The icing of an unheated non-rotating cylinder in liquid water droplet-ice crystal clouds

Lozowski, E. P.; Stallabrass, J. R.; Hearty, P. F.

Publisher's version / Version de l'éditeur:
https://doi.org/10.4224/40003080
Laboratory Technical Report (Low Temperature Laboratory (Canada)); no. LTR-LT-96, 1979-02

National Research Council Canada | Conseil national de recherches Canada

DIVISION OF MECHANICAL ENGINEERING

LABORATORY TECHNICAL REPORT

RAPPORT TECHNIQUE DE LABORATOIRE

DIVISION DE GÉNIE MÉCANIQUE

OTTAWA, CANADA

Dr. Whyte

National Research Council Canada | Conseil national de recherches Canada

DIVISION OF MECHANICAL ENGINEERING

DIVISION DE GÉNIE MÉCANIQUE

PAGES Text - 61
PAGES Appendices - 11

FIG. DIAG. 31

TABLES TABLES 5

REPORT
RAPPORT

LABORATORY / LABORATOIRE

Low Temperature

REPORT RAPPORT LTR-LT-96

DATE DATE February 1979

LAB. ORDER COMM. LAB. 16329A

FILE DOSSIER 3741-2

FOR POUR Internal

REFERENCE RÉFÉRENCE

LTR - LT - 96

THE ICING OF AN UNHEATED NON-ROTATING CYLINDER IN LIQUID WATER DROPLET - ICE CRYSTAL CLOUDS

SUBMITTED BY PRÉSENTÉ PAR T. R. Ringer
LABORATORY HEAD
CHEF DE LABORATOIRE

AUTHOR AUTEUR E. P. Lozowski*
J. R. Stallabrass
P. F. Hearty

APPROVED APPROUVÉ D. C. MacPhail
DIRECTOR
DIRECTEUR

* Visiting Research Officer on study leave from the University of Alberta, Department of Geography, Division of Meteorology.

COPY NO. COPIE NR. 61

TABLE OF CONTENTS

TABLE OF CONTENTS (cont'd)

LIST OF ILLUSTRATIONS

LIST OF ILLUSTRATIONS (cont'd)

SUMMARY

Concern over unusually high rates of torque rise, encountered recently by helicopters in natural icing flights, has led to the suggestion that perhaps ice crystals existing within a cloud of supercooled droplets may contribute to a rapid increase in the rotor blade icing rate. With a view to testing this hypothesis, and at the same time to developing a greater insight into the physics of rotor blade icing, it was decided to develop a model of mixed condition icing, and to test it by comparison with icing tunnel measurements. As a start, both the model and the experiments were based on cylinder icing. This report presents in some detail the development of the model for fixed cylinder icing with runback, and verifies it against a large set of experimental cylinder icing tests, performed over a wide range of suitable environmental conditions. The results of these efforts answer a few of the concerns about mixed condition icing. They suggest in fact that supercooled water-ice crystal clouds may not pose a serious hazard. On the other hand, many further questions are raised concerning the details of the accretion mechanism, and these questions will have to be answered before much further progress in modelling will be possible. The report therefore concludes with recommendations for future icing experiments and model development.

1.0 INTRODUCTION

1.1 Helicopter Rotor Blade Icing: The Problem

Early helicopter flight tests in icing conditions produced by the National Research Council's helicopter spray rig (Stallabrass, 1957 and 1958) demonstrated the susceptibility of the helicopter to icing of the rotor blades. There were three principal effects of rotor blade ice accretion:

1. An increase in the blade drag, necessitating an increased engine power if the same rotor speed and lift are to be maintained. Little direct change in the blade lift coefficient is observed, however.

2. The projectile shedding of ice from the rotor blades, once the ice mass exceeds the value at which the centrifugal force equals the adhesive force between the ice and the blade. Such shedding may cause damage to the helicopter.

3. The likelihood of asymmetric ice shedding, of different extent on each blade, causing the centre of mass to shift away from the centre of rotation. The resulting vibrations may at times be severe, and they place an unusually high load on the rotor system structural members and control mechanisms.

These tests also demonstrated the complexity of the rotor blade ice accretions. Because of the variation in velocity from near zero at the blade root to close to sonic at the tip, the thermodynamic conditions vary along the length of the blade. Consequently, both the rate of icing and the character of the ice accretion are functions of the blade radius. Further variations in the ice form might be expected between hovering and forward flight as a result of the cyclic variations in blade pitch, lag angle, and velocity experienced in forward flight conditions. Observation of such accretions at the conclusion of flights in natural conditions is all but impossible, however, owing to ice loss between leaving the icing conditions and the rotors coming to a stop after landing. It has therefore been impossible to date to determine observationally the nature or magnitude of the icing effects produced by these cyclic variations. Perhaps the in situ photographic techniques currently being developed for recording the ice accretions in flight (Ray, 1978) will help to resolve how significant these cyclic effects are.

In recent years, helicopters flying in natural icing conditions have occasionally experienced sudden extreme rates of torque rise (Lake and Bradley, 1976), which were not predicted on the basis of the icing rig hovering flights. In addition to the drag rise, some reduction in the lift coefficient was also observed. These events, which occurred at temperatures just a few degrees below 0°C led to much speculation as to their cause, particularly as photographic evidence showed ice on the blades at greater radii than had previously been observed or predicted by theoretical calculations of stagnation line ice accretion rates (Stallabrass, 1957). Unfortunately, insufficient instrumentation was mounted on board the aircraft to determine the complete microphysical properties of the clouds in which this phenomenon occurred. As a consequence, speculation as to the cause or explanation of these events was not constrained by a complete set of measurements.

The various hypotheses put forward included the following:

1. The validity of the rig tests in hovering flight was questionable because the limited cloud width resulted in relatively lower droplet impingement rates in the critical rotor blade tip region.

2. Because of the lack of cyclic blade variations, ice accretions in hovering flight do not present the same aerodynamic penalties as ice accreted in forward flight.

3. The theories on which the simple calculations of stagnation line ice accretions were based are in serious error because they do not predict ice in areas where the photographic evidence has shown it to occur.

4. The theories are essentially correct, but unusual or unexpected environmental conditions were encountered. These may have consisted of extremely high liquid water contents, or mixed conditions of supercooled droplets with either ice crystals or snow.

Speculations 1 and 2 may have some merit, but they do not explain the apparent discrepancy between theory and observation. The proponents of the third suggestion have failed to appreciate that the simple theoretical calculations were applicable to the stagnation line only. The radial extent of icing may be greater above and below the stagnation line than it is on the stagnation line itself, with the greatest extent occurring above the stagnation line in the region of maximum local velocity. An extension of the simple theory is therefore needed to provide predictions of the ice accretion rate away from the stagnation region. This is one of the aims of the work presented in this report.

Speculation 4 implies that because of the rather specialized "operational envelope" of the helicopter, environmental conditions are being encountered which have not been recognized previously as being a hazard for fixed wing aircraft. Because of the nature of fixed wing aircraft operation, such conditions either are flown in very infrequently, or are encountered as a transient only as the aircraft climbs through them. It is possible for example to encounter cumulus clouds embedded in a stratus layer, and so to experience an unexpectedly high water concentration. This could have a serious effect on the aerodynamics of the helicopter rotor blades, while, because of its brevity, having an almost insignificant effect on the larger scale wings of a fixed wing aircraft.

Mixed cloud icing conditions may be more extensive than such high liquid water concentration conditions, and should therefore possibly be of greater concern for designers of an all-weather rotor craft. It is generally assumed that in mixed conditions, impinging ice crystals will adhere to a wet icing surface, thereby enhancing the growth rate of the accretion. Further, the heat capacity of these adhering ice crystals will modify the icing thermodynamics, permitting more liquid water to freeze, and resulting in a more extensive and possibly a rougher ice accretion. Thus it was suggested that these mixed conditions might help to explain the rapid torque rises and the

photographic evidence of greater than expected ice extents. A second aim of the present work is in fact to test this hypothesis by incorporating ice crystals into a mathematical model of the icing process, and by undertaking icing tunnel experiments to verify the assumptions upon which the model is based.

Because of the complexities involved in modelling the ice accretion process on an airfoil, it was decided that the simpler, more tractable case of a cylinder should be modelled first. Once an acceptable model of this icing process is achieved, the next logical step will be to extend it to an airfoil. In fact this has already been attempted (Kloner, 1970, and Werner, 1973). Although an important initial attempt, this work lacks suitable airfoil heat transfer data, does not allow for adiabatic temperature changes in the airstream at high Mach numbers, and does not consider mixed conditions. It is also unfortunate that it has not been directly verified with icing experiments. In order that icing modellers not operate in a vacuum, it is essential that modelling be undertaken in conjunction with simultaneous icing experiments.

1.2 Review of Cylinder Icing under Rotor Blade Conditions

Ludlam (1951), was one of the first to publish work on the thermodynamics of cylinder icing. In fact, he was among the first to suggest that a thermodynamic limit might exist to the rate of ice accretion on a rotating cylinder, implying that as the liquid water content is raised at a fixed temperature and airspeed, the ice accretion rate does not continue to grow indefinitely. Below this critical liquid water content, usually called the Ludlam limit, the growth is "dry" in the sense that the equilibrium surface temperature is less than or equal to 0°C and all the impinging liquid water is thermodynamically capable of freezing. Above this value, Ludlam assumed that the excess liquid water which could not be frozen was shed into the airstream. It was first recognized by Fraser, Rush, and Baxter (1952) and subsequently documented by List (1959), that under some icing conditions, not all of this excess water, accreted above the Ludlam limit, is lost into the airstream. In fact none may be lost up to a certain point beyond which the excess liquid is shed. Instead the liquid water is contained in pockets within the ice matrix, forming a mixed accretion for which the term "spongy ice" was coined. Recently, List (1977) has reviewed this concept of spongy ice in the light of new experimental findings at high liquid water contents.

The physics of the icing of rotating cylinders is relatively easily amenable to a theoretical treatment because the deposit has rotational symmetry. On the other hand, airfoil icing is a much more difficult problem to treat because it may lack any symmetry at all, and it is especially complicated by the runback of excess water along the surface. In order to bridge the gap between the relatively simple rotating cylinder problem and the highly complex airfoil icing problem, a number of authors (Cansdale and McNaughtan, 1977, and Ackley and Templeton, 1978) have addressed the problem of the icing of a non-rotating cylinder. In this case the runback effects are still present, but the geometry is simplified and data is available on the collection efficiency (Langmuir and Blodgett, 1946), and on the heat transfer of cylinders (Zukauskas, 1972). Thus in the present work, we will also adopt this point of view and begin by examining cylinder icing before proceeding in logical stages to a theoretical

investigation of the airfoil icing problem. In preparation for this next step, we have in fact already undertaken wind tunnel icing experiments on airfoils (Stallabrass and Lozowski, 1978).

Our approach differs somewhat from that of both Ackley, and Cansdale and McNaughtan. Ackley has examined cylinder icing under liquid water conditions. In his model he calculates the overall rate of accretion and assumes that it is distributed over the cylinder surface in such a way that the surface is always a smooth ellipse with a minor axis equal to the cylinder diameter. A novelty of his approach is that it is time dependent, and he takes into account the effect of the changing accretion profile on the collection efficiency, and in an empirical manner, on the overall heat transfer coefficient. He also compares his model predictions with measurements of ice accreted on a whirling cylinder at very cold temperatures (Ackley et al, 1978).

Cansdale and McNaughtan's approach is a more detailed one. They consider the accretion as a function of the angle around the cylinder circumference and their model allows for runback water. They also go on to consider the possibility of mixed accretion icing, and they outline a model which will perform these calculations. However, their report does not include model predictions or comparisons with experiment. In the present work we have developed a model, initially independently but in the later stages in cooperation with Cansdale and McNaughtan, which is similar in principle to theirs, although it differs in a number of details. In this report, we will present results of the simulated icing predicted by our model and will compare them with experimental icing measurements in both liquid water and mixed conditions. The experiments were performed on a .0254 m diameter cylinder in the high speed icing tunnel at the Low Temperature Laboratory, National Research Council.

1.3 Outline of the Report

The report begins by describing in some detail a numerical ice accretion model for unheated, non-rotating cylinders. The model is developed for supercooled liquid water icing initially, and then is extended to include mixed accretion in clouds containing both liquid water and ice crystals. Following this, experiments on a .0254 m diameter cylinder are described, which were undertaken in the high speed icing tunnel of the Low Temperature Laboratory, N.R.C. The icing wind tunnel is described, the details of the experimental procedures follow, and the results obtained are presented. Results of the icing experiments are displayed chiefly in the form of photographs of the accretions and profiles of the ice shapes, from which average linear and volumetric growth rates can be deduced. Finally some model results are presented in the form of linear stagnation line growth rates and model predicted profiles. These results are compared with the experimental observations, and certain deductions regarding the success and failure of the model, as well as inferences concerning the mechanisms of the icing process, are made. A number of positive recommendations are made concerning some potentially fruitful directions for future experimental and modelling research in this field.

2.0 CYLINDER ICING MODEL: LIQUID ACCRETION

2.1 Steady State Heat Balance Equation

The traditional approach to the thermodynamics of icing (Messinger, 1953) is to start with the quasi-steady state heat balance equation. This equation is based on the assumption that the accretion is in thermal equilibrium, and therefore that the sum of all sources and sinks of heat is zero. The significant heat terms for rotor blade icing are:

SINKS: 1. Conduction and convection through the cylinder boundary layer. 2. Latent heat transfer due to evaporative and sublimative mass transfer through the boundary layer. 3. Warming of the accreted water to the equilibrium surface temperature. 4. Conduction into previously deposited ice and into or along the cylinder itself.

SOURCES: 5. Latent heat of freezing at the equilibrium surface temperature of a certain fraction of the accreted water. 6. Aerodynamic heating due to adiabatic compression of the air and viscous work in the boundary layer. 7. Kinetic energy of the impinging droplets. Under some circumstances, the heat transfer due to the shedding of water (either by splashing or melting) may be important, but we choose to ignore this effect as well as that due to term 4.

With these assumptions, the heat balance equation may be written:

$$\underset{1}{h(t_a - t_s)} + \underset{2}{h\left(\frac{Pr}{Sc}\right)^{.63} \frac{\epsilon \ell_v}{p c_p} (e_a(t_a) - e_s(t_s))} + \underset{3}{R_w \bar{c}_w (t_a - t_s)} + \underset{5}{n R_w \ell_f(t_s)}$$

$$+ \underset{6}{\frac{1}{2} \frac{h r_c U^2}{c_p}} + \underset{7}{\frac{1}{2} R_w U^2} = 0 \qquad (2.1.1)$$

In this equation, the terms are numbered according to their physical descriptions given above. The symbol meanings are not given here, because each term will be treated individually in succeeding sections. One of the early references to an equation of this type is the work of Tribus (1952), although since he uses engineering units, his equation is not identical in appearance to 2.1.1, which is formulated for SI units. More recently, Cansdale and McNaughtan (1977) and Ackley (1978) have employed an equation similar to 2.1.1 in the development of their cylinder icing models.

In order ultimately to make use of and solve this equation, we will now begin by examining the formulation of each of its terms.

2.2 Collection Efficiency

Due to their inertia, the water droplets in a supercooled icing cloud will not follow the air streamlines exactly, but instead will deviate away from them so that they impinge upon the cylinder. Langmuir and Blodgett (1946) have

computed the trajectories of water droplets around cylinders in a potential flow, and their work has been used in the present investigation as a basis for determining the liquid water collection efficiency. This is defined as the ratio of the mass of water actually caught on some surface element, to that which would be caught if the droplet trajectories were straight lines parallel to the undisturbed flow, and if the surface element were oriented perpendicular to the flow. Because the collection efficiency in this study is a function of angle around the cylinder, the upwind face is divided into angular sectors, each 5° in width and centred on the angles $\theta_i = 5i°$, $i = 0,1,2,....18$. Each sector has the same surface area per unit cylinder length, but the component of the surface area normal to the undisturbed flow diminishes as $\cos \theta_i$.

The droplet size spectrum is divided into nine diameter categories. These are each 5 μm wide, and centred on the diameters $D_j = (5j - 2.5)$ μm, $j = 1,2,....9$. For the purpose of estimating the collection efficiency, all the droplets in each size category are treated as if they had the centre value diameter, D_j. For each value of D_j, the stagnation line collection efficiency, β_{oj}, the overall collection efficiency E_j, and the maximum impingement angle θ_{mj} are calculated according to the formulae of Langmuir and Blodgett. In order to do this, three droplet parameters must first be evaluated. The droplet Reynolds number Re_j is defined by:

$$Re_j = \frac{\rho_a U D_j}{\mu_a} \qquad (2.2.1)$$

where ρ_a and μ_a are respectively the density and dynamic viscosity of the air, and U is the free stream speed. The non-dimensional inertia parameter K_j is defined by:

$$K_j = \frac{2\lambda_{sj}}{D_c} \quad \text{where} \quad \lambda_{sj} = \frac{\rho_w U D_j^2}{18\mu_a} \qquad (2.2.2)$$

where ρ_w is the droplet density, D_c the cylinder diameter, and λ_{sj} the droplet range when released as a projectile with initial velocity U into still air under the assumption that Stokes Law holds. Because Stokes Law is not valid at the velocities of interest, an adjustment to K_j must be made in order to permit the use of the Stokes Law results.

This is done by defining:

$$K_{oj} = .125 + (K_j - .125)\left(\frac{\lambda}{\lambda_s}\right)_j \qquad (2.2.3)$$

where λ is the actual droplet ballistic range. Langmuir and Blodgett's table of λ/λ_s as a function of Re, part of which is reproduced in Table 2.2.1, has been fitted empirically using the formula:

$$\left(\frac{\lambda}{\lambda_s}\right)_j = \frac{1}{1 + .0967\, Re_j^{0.6367}} \qquad (2.2.4)$$

The values given by Equation 2.2.4 generally lie within 10% of the Langmuir and Blodgett values over the entire range of Re_j of interest.

Using K_{oj}, values of β_{oj}, E_j, and ϑ_{mj} can be calculated according to:

$$\beta_{oj} = E_j = \vartheta_{mj} = 0 \qquad K_{oj} < .125 \qquad (2.2.5a)$$

$$\beta_{oj} = \frac{1.4\,(K_{oj} - .125)^{.84}}{1 + 1.4\,(K_{oj} - .125)^{.84}} \qquad .125 \leqslant K_{oj} < 7.5 \qquad (2.2.5b)$$

$$\beta_{oj} = \frac{K_{oj}}{1 + K_{oj}} \qquad 7.5 \leqslant K_{oj} \qquad (2.2.5c)$$

$$E_j = .489\,(\log_{10} 8K_{oj})^{1.978} \qquad .125 \leqslant K_{oj} < .9 \qquad (2.2.6a)$$

$$E_j = \frac{K_{oj}}{\frac{\pi}{2} + K_{oj}} \qquad .9 \leqslant K_{oj} \qquad (2.2.6b)$$

$$\vartheta_{mj} = \tan^{-1}(1.7(K_{oj} - .125)^{.76}) \qquad .125 \leqslant K_{oj} < 10 \qquad (2.2.7a)$$

$$\vartheta_{mj} = \tan^{-1} K_{oj} \qquad 10 \leqslant K_{oj} \qquad (2.2.7b)$$

Some of these equations, namely 2.2.5c, 2.2.6a, and 2.2.6b, have been modified from their Langmuir and Blodgett form in an attempt to improve their accuracy vis-à-vis the Langmuir and Blodgett graphical data. Recently, however, Stallabrass (1978) has shown that the original Langmuir and Blodgett equation corresponding to 2.2.6b, namely:

$$E_j = \frac{K_j}{H_{E_j} + K_j} \qquad (2.2.8)$$

will give better accuracy than Equation 2.2.6b, when properly applied. Overall, Equations 2.2.5a to 2.2.7b provide a good fit to Langmuir and Blodgett's graphical data, and this is illustrated in Table 2.2.2. Over the range of parameters of interest for this work, the maximum errors in β_o, E and ϑ_m are .053, .056 and 2.5° respectively. The parameter ϕ in Table 2.2.2 is Re^2/K.

In order to calculate the variation of the collection efficiency with angle around the cylinder for each drop size, the relation given below was employed:

$$\beta_j(\vartheta_i) = \beta_{ij} = \beta_{oj}\cos\left(\frac{\pi}{2}\,\frac{\vartheta_i}{\vartheta_{mj}}\right) + \frac{\pi^3}{\vartheta^3_{mj}(\pi^2-4)}\left(E_j - \frac{2\vartheta_{mj}\beta_{oj}}{\pi}\right)\vartheta_i^2 \sin\left(\pi\,\frac{\vartheta_i}{\vartheta_{mj}}\right)$$

$$\text{for } \vartheta_i < \vartheta_{mj} \text{ and } \beta_{ij} = 0 \text{ for } \vartheta_i > \vartheta_{mj} \qquad (2.2.9)$$

This equation satisfies the physical constraints $\beta_j(0°) = \beta_{oj}$, $\beta_j(\vartheta_{mj}) = 0$ and $\frac{1}{\vartheta_{mj}}\int_0^{\vartheta_{mj}} \beta_j(\vartheta)d\vartheta = E_j$. Its general form was chosen to fit the results of a detailed and lengthy calculation of $\beta(\vartheta)$ performed according to the procedure devised by Langmuir and Blodgett.

The overall collection efficiency for each sector is the mass-weighted mean over all the drop size categories:

$$\beta(\vartheta_i) = \beta_i = \sum_{j=1}^{9} f_j \beta_{ij} \qquad (2.2.10)$$

where f_j is the fraction of the total droplet mass flux in the undisturbed flow consisting of droplets in the jth size category. Finally, the liquid water mass flux ($kgm^{-2}s^{-1}$) impinging on each sector is $R_{wi} = \beta_i Uw$, where w is the volumetric concentration or liquid water content (LWC) in kgm^{-3} of liquid water in the airflow.

2.3 Heat Transfer with the Airstream

The rate of transfer of sensible heat from the cylinder in watts/m^2 is governed by the term $q_c = h(t_s - t_a)$, where t_s and t_a are respectively the equilibrium surface temperature and the local air temperature above the boundary layer, and h is the heat transfer coefficient. In terms of the dimensionless Nusselt number, Nu, h is given by $k_a D_c^{-1} Nu$, where k_a is the thermal conductivity of air, and D_c is the cylinder diameter. The Nusselt number is found experimentally to be a function of the angle around the cylinder, ϑ, the cylinder Reynolds number, $Re_c = \frac{UD_c \rho_a}{\mu_a}$, the cylinder roughness (characterized by the ratio of the roughness scale to the cylinder diameter), the Prandtl number of the fluid (essentially constant for air and equal to 0.711), and the turbulence level of the free stream. This functional dependence has been discussed by Zukauskas (1972) and by Achenbach (1974) among others. For a smooth cylinder in a non-turbulent airstream (<~ 1% turbulence intensity), the Nusselt number data of Achenbach (1974) can be approximated by the relation:

$$Nu = Re_c^{.5}\left(1 - \left(\frac{2\vartheta}{\pi}\right)^3\right) \qquad (2.3.1)$$

This equation is valid for ϑ between 0° and about 80°, where the boundary layer becomes turbulent, and the Nusselt number begins to increase rapidly with ϑ. Since we are primarily interested in icing on the upstream surface of the cylinder, the heat transfer characteristics beyond about 80° may be ignored for the present.

Data in the literature on the effects of free stream turbulence on the heat transfer are incomplete. Moreover, the turbulence in the high speed wind tunnel is unknown. Consequently, it was decided to ignore this effect in calculating the heat transfer coefficient. According to Zukauskas (1972), this could give rise to an underestimate of the heat transfer rate by as much as a factor of two.

Achenbach (1974) presents some experimental results on the effect of homogeneous surface roughness on the heat transfer. The data do not cover a sufficiently wide range of Reynolds number and roughness parameter to permit a general expression for the Nusselt number to be developed. However, at $Re_c = 2.6 \times 10^5$ and a roughness parameter $R_o = 9 \times 10^{-3}$, the following equation is found to provide a reasonable fit to his experimental points:

$$Nu = Re_c^{.5} \, (2.4 + 1.2 \sin (3.6 \, (\varphi - 25°))) \qquad (2.3.2)$$

The roughness of an icing cylinder depends on the local character of the ice accretion. If the surface is dry ($t_s < 0°C$), the deposit is generally smooth except near the edges where rime feathers develop. If the droplets are freezing individually rather than coalescing before freezing, then the roughness parameter for such a surface would likely be of the order of the ratio of the volume median droplet diameter to the cylinder diameter, or about 10^{-3}. When the accretion becomes wet ($t_s = 0°C$), and a film of runback water covers some of the surface, the roughness of the ice deposit increases. The roughness parameter will then be a function of φ, and experiments indicate values as high as 10^{-1} (depending on how the dimensions of the roughness elements are defined).

In view of the above discussion, it is clear that there remains a considerable uncertainty about the quantitative local heat transfer for icing cylinders. For want of more complete data, however, Equations 2.3.1 and 2.3.2 were used to represent the heat transfer effects in the model. In the computer program, a choice can be made between "rough" heat transfer ($R_o = 1$ and Equation 2.3.2) and "smooth" heat transfer ($R_o = 0$ and Equation 2.3.1). In this way, the heat transfer appropriate to a wet or dry surface can be chosen, the state of the surface being determined a posteriori either by the model or by experiment.

In addition to the sensible heat transfer, there is a transfer of latent heat due to the evaporation or sublimation of water vapour from the surface. According to Reynolds' analogy, this term can be written in a similar form to that for the sensible heat transfer, making use of the heat transfer coefficient:

$$q_e \ (W/m^2) = h \left(\frac{Pr}{Sc}\right)^{.63} \frac{\epsilon \ell_v}{p c_p} (e_a - e_s) \qquad (2.3.3)$$

where Pr and Sc are the Prandtl and Schmidt numbers respectively, ϵ is the ratio of the molecular weights of water vapour and dry air (0.622), p is the static pressure in the free stream, c_p is the specific heat capacity at constant pressure of dry air, and e_a and e_s are the saturation vapour pressure of moist air at the local temperature above the boundary layer and at the equilibrium surface temperature respectively. Finally, ℓ_v is the specific latent heat of vaporization. Since there may be both ice and liquid water on the surface at a given time, it is not clear whether the appropriate latent heat is that of sublimation or of vaporization or a combination of the two. Even at equilibrium surface temperatures somewhat below 0°C, a water film may exist on the surface because of the finite length of time required for total freezing of the impinging droplets. In view of this, and in order to avoid a discontinuous transition between the latent heats of vaporization and sublimation, we have chosen to use the latent heat of vaporization in this term under all conditions.

It should be pointed out that certain assumptions in the derivation of Equation 2.3.3 mean that it does not remain valid when the surface pressure around the cylinder deviates significantly from the free stream static value. Consequently, for free stream speeds approaching sonic values, this term should be re-derived. A similar caveat should be expressed regarding the possible effects of compressibility on the heat transfer coefficient and the collection efficiency.

2.4 Aerodynamic Heating

The aerodynamic heating consists of two components: adiabatic heating arising from the compression of air which is decelerated in passing around the cylinder outside the boundary layer, and frictional (viscous) heating within the boundary layer. The effect of this heating on a passive, non-conducting body is to raise its surface temperature to T_s^*(°K), thereby giving rise under steady state conditions to an outward heat flux of magnitude $h\ (T_s^* - T_a)$, T_a being the free stream air temperature in °K. Since this heat source is of mechanical origin, it must be independent of the thermodynamic properties of the surface. In particular, it remains valid for an icing surface. In order to calculate this term, it is necessary to determine $(T_s^* - T_a)$. This is done in two stages. First, the adiabatic temperature rise $(T_L - T_a)$ may be obtained from a consideration of the energy equation for compressible flow. Then the boundary layer temperature rise $(T_s^* - T_L)$ may be calculated using the flat plate analogy (Schlichting, 1968). The temperature T_L (°K) is the local temperature above the boundary layer.

A consideration of the Bernoulli equation of motion, the adiabatic thermodynamic equation, and the ideal gas law yields the steady state total energy equation:

$$\tfrac{1}{2}U^2 + c_pT = \text{a constant along a streamline} \qquad (2.4.1)$$

That is, the sum of the specific kinetic energy and the specific enthalpy is constant along a streamline. Considering a streamline from the free stream to a point L somewhere above the boundary layer, Equation 2.4.1 yields:

$$T_L - T_a = \frac{1}{2c_p}(U^2 - U_L^2) \qquad (2.4.2)$$

where U_L is the local airspeed outside the boundary layer at point L, and U is the free stream airspeed.

According to Schlichting, the equilibrium boundary layer temperature rise above a non-conducting flat plate is:

$$T_s^* - T_L = \frac{rU_L^2}{2c_p} \qquad (2.4.3)$$

where the flat plate recovery factor $r = \sqrt{Pr}$ or 0.85 for a laminar boundary layer, and $r = \sqrt[3]{Pr}$ or 0.90 for a turbulent boundary layer. Adding Equations 2.4.2 and 2.4.3 gives the desired result, namely:

$$T_s^* - T_a = \frac{1}{2c_p}\left(U^2 - (1-r)\,U_L^2\right) \qquad (2.4.4)$$

It is customary to define a recovery factor for the cylinder, $r_c(\theta)$, in terms of the stagnation point adiabatic temperature rise $\frac{U^2}{2c_p}$; that is,

$$T_s^* - T_a = \frac{r_c\,U^2}{2c_p} \qquad (2.4.5)$$

In terms of r_c, the local aerodynamic heating q_v is $\frac{hr_cU^2}{2c_p}$ W/m^2, and in view of 2.4.4 and 2.4.5, we have:

$$r_c = \left(1 - (1-r)\,\frac{U_L^2}{U^2}\right) \qquad (2.4.6)$$

In order to determine r_c, it may be more convenient to use p_L rather than U_L. This can be done by substituting into Equation 2.4.6 for U_L in terms of p_L as follows. For isentropic flow, $p^{\frac{1-\gamma}{\gamma}}T$ is constant along a streamline, implying that:

$$T_L - T_a = T_a\left(\left(\frac{p}{p_L}\right)^{\frac{1-\gamma}{\gamma}} - 1\right) \qquad (2.4.7)$$

where p is the free stream static pressure. Comparing Equation 2.4.7 with Equation 2.4.2, one readily obtains $U_L(p_L)$, which combined with Equation 2.4.6 yields:

$$r_c = \left(r + (1-r)\,\frac{2c_pT_a}{U^2}\left(\frac{p}{p_L}\right)^{\frac{1-\gamma}{\gamma}} - 1\right)) \qquad (2.4.8)$$

The cylinder recovery factor used in the present study is based on the work of Seban (1960). It is:

$$r_c = 0.75 + 0.25\cos 2\theta \qquad (2.4.9)$$

Cansdale and McNaughtan (1977) use a somewhat different formulation.

2.5 Droplet Kinetic Energy

The kinetic energy flux of the droplets q_{kw} is given by $\frac{R_wU^2}{2}$ where R_w is the droplet mass flux defined by:

$$R_w = \beta_{wU} \qquad (2.5.1)$$

and w is the volumetric water concentration (henceforth referred to as the liquid water content or LWC) in the airstream. It is assumed that all of this kinetic energy is converted into thermal energy upon impact. This is certainly an overestimate, but since this term is generally small compared with the other heat transfer terms, the error introduced by making such an assumption is probably small.

It should be borne in mind that droplets in a wind tunnel airstream may not have achieved the airspeed prior to impacting upon the cylinder. This possibility and its implications will receive further attention in Section 4.1, with specific reference to the high speed icing tunnel in the Low Temperature Laboratory. In addition to this effect, acceleration of a droplet in the curved flow adjacent to the cylinder will also cause its velocity to deviate from the free stream speed. However, the practical significance of both of these effects for this heat transfer term is probably minor.

2.6 Thermodynamics of the Accretion

Upon impact, individual supercooled droplets at the air temperature t_a (in °C) are nucleated by contact with pre-existing ice on the cylinder, or by ice nuclei within the droplets or on the cylinder surface. The supercooling permits the rapid growth of ice dendrites in a few milliseconds, with an accompanying release of latent heat that raises the temperature to 0°C (provided that $t_a \geqslant -80$°C). The fraction of the droplet mass which is rapidly converted into dendritic ice is $|t_a| / \ell_f$ (0°C) or about 1.25×10^{-2} for each degree Celsius of supercooling. This quantity will also influence the extent to which the droplet retains its spherical shape or is flattened upon impact (Brownscombe and Hallett, 1967). Further freezing proceeds at 0°C, at a rate determined by the transfer of the latent heat of freezing to the airstream (c.f. Section 2.3) or to the substrate (Section 2.7). This rate may not be sufficient to permit all the liquid water to freeze before another droplet is accreted in the same location. In this event, some of the unfrozen water may remain trapped within the ice matrix (forming "spongy ice"), or some may be driven back along the cylinder surface by the aerodynamic stresses ("runback water"). If the heat transfer rate to the airstream is large enough, all of the liquid water will freeze, and the ice will cool to a final temperature $t_f \leqslant 0$°C by the time another droplet is accreted in the same location.

Not all of the droplets in the same region on the surface at the same time will be undergoing identical thermal changes, since the accretion of cloud droplets is a stochastic process. At any time on a certain surface element, some drops will be in the warming phase ("initial freezing"), some at 0°C ("subsequent freezing") (Macklin and Payne, 1967) and still others, completely frozen, may be cooling. This complexity is obviated in most models by postulating a mean thermodynamic cycle for the entire ensemble of droplets which is accreted over a small time interval by a particular surface element. This consists of a warming phase from t_a to 0°C, partial or complete freezing, and finally if necessary a cooling phase to some final temperature t_f. However, even this degree of complexity makes the heat transfer with the airstream difficult to calculate. Consequently, for the purpose of calculating the heat transfer, a time independent "equilibrium" surface temperature, t_s, is usually assumed. This same temperature is also taken to be the final temperature after the cooling phase. Such a model is not consistent, since the heat transfer on the average will occur at a temperature which is somewhat higher than the final deposit temperature. This inconsistency can be avoided, however, by assuming the thermodynamic changes in the surface temperature to occur instantaneously so that the heat transfer is always from a surface at temperature t_s.

The heat flux in the warming phase is given by:

$$q_w = R_w \bar{c}_w (t_a - t_m) \qquad (2.6.1)$$

where t_m is the freezing/melting temperature (usually taken to be 0°C), and $\bar{c}_w$ is the average specific heat capacity of water between t_a and t_m. The latent heat of freezing at t_m gives rise to a flux:

$$q_f = R_w \ell_{fm} n \qquad (2.6.2)$$

where n is the fraction of the accreted mass which freezes, and ℓ_{fm} is the specific latent heat of freezing at t_m.

Finally, the heat flux in the cooling phase is:

$$q_i = R_w \bar{c}_i (t_m - t_s) n \qquad (2.6.3)$$

where $\bar{c}_i$ is the average specific heat of ice between t_m and t_s. The sign convention used in these and all other expressions for heat flux is that a positive value is exothermic. The quantities n and t_s are not independent since when $n < 1$, $t_s = 0°C$, while when $t_s < 0°C$, $n = 1$. This is the assumption made in the model, and it implies that there can be no runback unless the equilibrium surface temperature, t_s, is 0°C. The possibility of runback occurring before all or any of the water has an opportunity to freeze, even when the equilibrium surface temperature is calculated to be below 0°C, cannot be entirely ignored, however. Such a non-equilibrium effect may play a significant role in the first seconds of accretion (before the initial nucleation takes place), and also for accretion at high speeds and warm temperatures.

The sum of these three terms can be written as:

$$R_w \bar{c}_w (t_a - t_m) + R_w \ell_{fm} n + R_w \bar{c}_i (t_m - t_s) n \qquad (2.6.4)$$

where the third term is zero unless $n = 1$. The process of warming the liquid from t_a, freezing at 0°C, and cooling the ice to t_s, is thermodynamically equivalent to warming the accreted water from t_a to t_s and freezing it at t_s. Consequently, expression 2.6.4 may alternatively be written more compactly as:

$$R_w \bar{c}_w (t_a - t_s) + R_w \ell_{fs} n \qquad (2.6.5)$$

where we still have that $n = 1$ when $t_s < 0°C$, while $t_s = 0°C$ when $n < 1$. The quantity ℓ_{fs} is the latent heat of freezing at t_s.

2.7 Internal Heat Conduction

The possibility of heat conduction into or along the surface of the cylinder or deposit (between regions of differing equilibrium surface temperature) can considerably complicate a heat transfer model. D'Amours (1977) has investi-

gated radial internal heat transfer in connection with a spherical model for hailstone growth, while Kloner (1970) has devised a model which deals with transverse conductive heat fluxes along ice accretions on an airfoil. For now, this type of heat flux is ignored in the present model. This is probably a reasonable approximation to describe the initial icing on a non-conducting cylinder.

Ackley and Templeton (1978) and Pellet and Dennis (1974) have examined the transient thermal effects associated with a perfectly conducting substrate (one with an infinite conductivity). They show that some tens of seconds may be required for the deposit and the substrate to achieve a thermal quasi-equilibrium. During this time, the deposit temperature warms slowly until it reaches the "equilibrium" surface temperature. Of course an infinite conductivity model is an idealization, even for a relatively highly conducting substrate such as steel. For a poorly conducting one such as bakelite, it is not appropriate (c.f. Sections 4.5 and 6.3).

2.8 Constants, Parameters, and Variables

In order to calculate the heat transfer terms described in previous sections of this chapter, it is necessary to know the values of various constants, and to be able to compute a number of quantities which are functions of temperature and pressure. Most of these values have been taken from the Smithsonian Meteorological Tables (List, 1951). Where this is not the case, the particular source is referenced.

1. The Prandtl number for the air is Pr = 0.711.
2. The Schmidt number for the air is Sc = 0.595.
3. The specific heat capacity of dry air is $c_p = 1.005 \times 10^3$ J/kgK.
4. The specific heat capacity of water at -10^0C is $c_w = 4.27 \times 10^3$ J/kgK. The maximum error, introduced by neglecting its variation with temperature between 0° and -15°C, is about 1%.
5. The specific heat capacity of ice at -5°C is $c_I = 2.07 \times 10^3$ J/kgK. The maximum error introduced by neglecting its variation with temperature between 0° and -10°C is about 2%.
6. The density of liquid water is taken to be 1000 kg/m^3.
7. The density of the ice deposit is taken to be 890 kg/m^3 everywhere, for the purpose of calculating the deposit volume from its mass. The size of the error introduced by this assumption depends on the amount of air or liquid water incorporated into the ice structure.
8. The density of moist air is calculated from the ideal gas law

$$\rho_a = \frac{p}{R_d T_v} \qquad (2.8.1)$$

where T_v is the absolute virtual temperature of the air (in °K), p the pressure (in Pascals), and R_d the specific gas constant for dry air, viz. 287.04 J/kgK. The absolute air temperature T_a may be substituted for T_v with an error of at most about 0.3% in the temperature range below 0°C.

9. The specific latent heat of freezing as a function of temperature is expressed by:

$$\ell_f(t°C) = \ell_f(0°C) + (\bar{c}_w - \bar{c}_I)\, t \qquad (2.8.2)$$

where t is in °C and $\ell_f(0°C) = 3.34 \times 10^5$ J/kg. The quantities $\bar{c}_w$ and $\bar{c}_I$ are average specific heat capacities for water and ice respectively between 0°C and t°C. They are approximated in the model by the constant values given in 4. and 5. above.

10. The specific heat of vaporization at 0°C is 2.50×10^6 J/kg. Ignoring its variation with temperature leads to a maximum 2% error between 0° and -20°C.

11. The dynamic viscosity of air is given by:

$$\mu_a(t) = 1.718 \times 10^{-5} + 5.1 \times 10^{-7}\, t\ (°C)\ \text{kg/ms} \qquad (2.8.3)$$

to an accuracy of better than 0.1% between 0° and -20°C.

12. The thermal conductivity of air is given by:

$$k_a\ (t) = 2.43 \times 10^{-2} + 7.3 \times 10^{-4}\, t\ (°C)\ \text{J/msK} \qquad (2.8.4)$$

to an accuracy of better than 0.5% between 0°C and -20°C.

13. The air temperature, pressure, liquid water content, drop size distribution, and cylinder diameter are all independent variables of the model.

14. The saturation vapour pressure as a function of temperature is calculated with the following fourth order polynomial in nested form (similar to Lowe, 1977):

$$e_s(t) = 609.92 + t(44.26 + t(1.4472 + t(2.7487 \times 10^{-2} + 2.59 \times 10^{-4} t))) \qquad (2.8.5)$$

This equation is accurate to better than 1% in the temperature range between 0° and -20°C. The derivative $\frac{\partial e_s}{\partial t}$ is represented by:

$$\frac{\partial e_s}{\partial t} = 44.26 + t(2.8944 + t(8.2461 \times 10^{-2} + 1.036 \times 10^{-3} t)) \qquad (2.8.6)$$

2.9 The Model without Runback

Ignoring runback for the moment, the Langmuir and Blodgett collection efficiencies permit the calculation of the mass flux $R_w(\Theta_i)$ for each angular sector of the cylinder. The heat balance equation (2.2.1) can then be solved in each sector to determine the equilibrium surface temperature $t_s(\Theta_i)$ or the freezing fraction $n(\Theta_i)$ for the deposit in that sector.

This is done by writing Equation 2.1.1 in the form

$$h(t_a - t_s) + h\left(\frac{Pr}{Sc}\right)^{.63} \frac{\epsilon \ell_v}{p c_p} (e_a(t_a) - e_s(t_s)) + R_w \bar{c}_w (t_a - t_s) + R_w \ell_f(t_s)\, n + \frac{h r_c U^2}{2 c_p} + \frac{R_w U^2}{2} = f(t_s) \qquad (2.9.1)$$

where the condition for equilibrium is $f(t_s) = 0$. In order to solve this equation for n or t_s given R_w, it is first postulated that $t_s = 0°C$ and Equation 2.9.1 is solved for n. If n lies within the interval $[0,1]$, the solution has been found. If n does not lie within this interval, then either $t_s > 0°C$ (if n was determined to be <0) or $t_s < 0°C$ (if n was found to be >0). In either event, the value of t_s may be determined by setting $n = 0$ or 1 as appropriate, and solving for the zero of the function $f(t_s)$ using Newton's Method, for example. In order to do this one requires the derivative

$$g(t_s) = \frac{\partial f}{\partial t_s} = -h - h\left(\frac{Pr}{So}\right)^{.63} \frac{\epsilon \ell_v}{pc_p} \frac{\partial e_s}{\partial t_s} + n R_w \frac{\partial \ell_f}{\partial t_s} - R_w \bar{c}_w \qquad (2.9.2)$$

The derivative $\frac{\partial e_s}{\partial t_s}$ is evaluated using the polynomial approximation of Section 2.8, while $\frac{\partial \ell_f}{\partial t_s}$ is specified by Kirchoff's Theorem, namely

$$\frac{\partial \ell_f}{\partial t_s} = c_w - c_I \qquad (2.9.3)$$

The value of t_s can now be sought iteratively with the equation

$$t_s^{new} = t_s^{old} - \frac{f(t_s^{old})}{g(t_s^{old})} \qquad (2.9.4)$$

Trying $t_s = 0°C$ as a first guess, only a few iterations are normally required to obtain a value for t_s with a precision of $\pm .01°C$. An even faster procedure might be to use as a first guess the equilibrium temperature determined for the immediately upstream sector.

2.10 The Model with Runback

In order to model runback effects on a fixed cylinder, it is assumed that all of the unfrozen water in any sector flows into the next downstream sector, and participates in the heat exchange there by adjusting to the new equilibrium surface temperature of that sector, and freezing in the same proportion as the directly impinging water. Since a steady state is assumed, the runback velocity is not needed. If $R_w^*(\vartheta_i)$ represents the runback mass flux <u>into</u> sector i centred on angle ϑ_i, and R_w represents the directly impinging mass flux, the heat balance equation becomes:

$$h(t_a - t_s) + h\left(\frac{Pr}{So}\right)^{.63} \frac{\epsilon \ell_v}{pc_p}(e_a(t_a) - e_s(t_s)) + R_w \bar{c}_w (t_a - t_s) + R_w \ell_f(t_s) n$$
$$+ \frac{hrU^2}{2c_p} + \frac{R_w U^2}{2} + R_w^* \bar{c}_w (t_s^* - t_s) + n R_w^* \ell_f(t_s) = 0 \qquad (2.10.1)$$

where the two last terms represent respectively the heat of cooling and freezing of the runback water. The incoming temperature t_s^* of the runback water is assumed to be the equilibrium surface temperature of the immediately upstream sector, viz.:

$$t_s^*(\vartheta_i) = t_s(\vartheta_{i-1}) \qquad (2.10.2)$$

Also, since R_w^* is the unfrozen portion of the total mass flux of the upstream sector

$$R_w^*(\Phi_i) = (1 - n)\ (R_w(\Psi_{i-1}) + R_w^*(\Psi_{i-1})) \qquad (2.10.3)$$

Beginning with the first sector which is centred on the forward stagnation line, Equation 2.10.1 can be solved in a fashion analogous to that described in Section 2.9, for each sector proceeding downstream in sequence. Because there is no sector upstream to the first, $R_w^*(\Phi_1) = 0$. Moreover, since the runback from sector 1 is split, half proceeding to the upper and half to the lower cylinder surfaces, Equation 2.10.3 must be modified for the second sector only so that

$$R_w^*(\Phi_2) = \tfrac{1}{2}\ (1-n)\ R_w(\Phi_1) \qquad (2.10.4)$$

The runback from the final sector, if there is any, is assumed to be shed into the airstream.

It should be kept in mind that this runback model does not take into account the possibility of spongy ice formation, splashing or shedding of water directly into the airstream from a sector other than the final one (List, 1977), non steady-state thermodynamics of the runback water, or "spanwise" flow in the direction of the cylinder axis, as would occur if the cylinder were mounted as a rotating arm. A comparison of modelled and actual ice shapes in Section 7.3 will suggest that at least some of these effects may need to be taken into account in future developments of the model. The details of the model computer program are not shown here, but will be presented in a more general form in Chapter 3, where mixed icing conditions will be discussed. Some model predictions will be presented in Chapter 7.

3.0 CYLINDER ICING MODEL: MIXED ACCRETION

3.1 Collection Efficiency for Ice Crystals

If the ice crystals are sufficiently large, their inertia will cause them to move in essentially straight line trajectories prior to impact. Thus their collection efficiency will be given approximately by

$$\beta_I(\Phi) = \cos\Phi \qquad (3.1.1)$$

where the subscript "I" will distinguish the ice from the liquid water. Some evidence for roughly straight line trajectories for ice crystals of dimension about 1 mm is contained in high speed 16 mm cine films which were taken of ice crystal-cylinder collisions in the icing tunnel. More details of this work will be presented in Chapter 5.

3.2 Sticking Efficiency of Ice Crystals

Some initial postulates concerning the sticking efficiency of ice crystals will be described here. These have had to be reconsidered in view of the results of mixed accretion icing tests (c.f. Sections 6.2 and 7.4), but at present no new quantitative theory of ice crystal sticking has been devised to replace the one presented here. Although the reader is cautioned to view this

model circumspectly, it will be described in some detail because it is based on hypotheses which have been employed by others (Stallabrass, private communication; English, 1973; Cansdale and McNaughtan, 1977), and because it may be possible to use it as a basis on which to develop a more realistic model of the ice crystal sticking phenomenon.

In order to describe this problem quantitatively, some new quantities must be defined, and some old ones re-defined. The symbol k will be used for the sticking efficiency, that is, the fraction of the impinging ice crystal mass which remains where it hit in the deposit. The symbol m is the fraction of the sticking ice mass which melts, and the symbol f is the fraction of the liquid water (both directly impinging and runback) which freezes. The quantity n will in future be used to describe the fraction of the total water substance mass flux into a sector which remains in that sector as ice. Although this is a new definition for n, it is consistent with the old one inasmuch as n and f are identical when there is no ice crystal accretion.

Other workers have generally assumed that the sticking efficiency of ice crystals is related to the "wetness" of the surface. That is, when the deposit is entirely "wet" ($t_s \geqslant 0°C$, $n = 0$), all impinging ice crystals are assumed to stick, while when it is entirely "dry" ($t_s \leqslant 0°C$, $n = 1$), it is hypothesized that none will stick, there being no means to bond them to the surface. Both of these assumptions are questionable since there appears to be no reason why a surface liquid layer should necessarily act to glue the impinging crystals in place, or why mechanical adhesion (sintering) or interlocking may not bond the crystals to a "dry" surface. It should also be borne in mind that a so-called "dry" surface, for which $t_s < 0°C$, may contain liquid water because of the finite time required for it to freeze. Such objections notwithstanding, these sticking hypotheses will be adopted for "completely wet" and "dry" conditions in the present model. The physics of the sticking process may be even more complicated when the deposit is "partly wet", i.e. when $t_s = 0°C$ and $0 < n < 1$. Unfortunately little experimental data has so far been available on which to base a sticking model. Macklin (1961) describes mixed condition accretion experiments, but these were done at low speeds and he does not derive sticking efficiencies from his results. Consequently, we resort again to the assumption that the sticking efficiency will be related to the wetness of the surface.

Following Stallabrass (private communication), we may hypothesize that the sticking fraction equals the liquid fraction which would prevail in the deposit if no ice crystals were accreted, i.e.

$$k = 1 - f' \qquad (3.2.1)$$

where f' is the freezing fraction of the droplet accretion taken by itself, ignoring the presence of the ice crystals. A more precise assumption may be to define

$$k = 1 - n \qquad (3.2.2)$$

where n is the actual ice fraction of the deposit when the thermodynamic effects of the sticking ice crystals are included. Unfortunately, Equation 3.2.2 is much more difficult to solve for k than is Equation 3.2.1 because n is also a function of k through the heat balance equation (c.f. Section 3.3). These sticking hypotheses, though tried, were not used.

The sticking hypothesis which was finally adopted for the present model is a hybrid based on the hypotheses of English (1973) and Cansdale and McNaughtan (1977). It is conveniently summarized in Table 3.2.1. If R_w and R_I are respectively the liquid water and ice crystal impingement fluxes, then n is related to f, k and m by the equation:

$$n = \frac{kR_I(1 - m) + fR_w}{kR_I + R_w} \qquad (3.2.3)$$

In thermodynamic zone 1, the deposit would grow dry even if there were no ice crystal impingement, so that $k = 0$ and $f = n = 1$, while $t_s < 0°C$. In zone 2, the liquid water only deposit would be wet, but a sufficient fraction of the ice crystal flux is assumed to stick, that the mixed deposit becomes "just dry". Consequently $f = 1$, $0 < k < 1$, and $m = 0$ making $n = 1$ while $t_s = 0°C$. In zone 3, even though all of the impinging ice crystals are accreted, not all of the liquid water can freeze, so that $k = 1$, $0 < f < 1$, $m = 0$ and $\frac{R_I}{R_I+R_w} < n < 1$. In zone 4, none of the liquid water freezes and some of the impinging ice melts, so that $f = 0$, $k = 1$, $0 < m < 1$ and $0 < n < \frac{R_I}{R_I+R_w}$. Finally in zone 5, all of the impinging ice sticks and melts, but the surface temperature rises above 0°C. In this breakdown into thermodynamic zones, there is some arbitrariness with respect to f and m. Clearly, if some additional ice crystals melt, increasing m, this will provide a heat sink sufficient to freeze an equal mass of the liquid accretion, thereby also increasing f. However, since such a process would leave n unchanged, this arbitrariness in f and m is of no particular consequence.

3.3 Heat Balance Equation in Mixed Conditions: No Runback

In order to account for the thermodynamic effects of the impinging ice crystals, it is necessary to add three terms to the heat balance equation (2.9.1). Assuming that the kinetic energy of all the impacting crystals is converted into heat (including those which do not stick), a source term $\frac{R_I U^2}{2}$ must be included, where $R_I = \beta_I w_I U$ and w_I is the ice crystal content (ICC) of the airstream in kg/m^3. In addition, the ice crystals provide two heat sink terms due to melting, $kmR_I \ell_f(t_s)$, and due to warming from the airstream temperature, $kR_I \bar{c}_I(t_a - t_s)$. Taking these terms into account, Equation 2.9.1 must be rewritten in the form:

$$h(t_a - t_s) + h\left(\frac{Pr}{Sc}\right)^{.63} \frac{\epsilon \ell_v}{pc_p} (e_a(t_a) - e_s(t_s)) + R_w \bar{c}_w (t_a - t_s) + kR_I \bar{c}_I (t_a - t_s)$$

$$+ R_w \ell_f(t_s) f - kmR_I \ell_f(t_s) + \frac{hr_c U^2}{2c_p} + \frac{R_w U^2}{2} + \frac{R_I U^2}{2} = f(t_s) \qquad (3.3.1)$$

The method of solution of this equation is similar to that described in Section 2.9. One begins by attempting to see whether the conditions of thermodynamic zone 3 (see Table 3.2.1) are consistent with Equation 3.3.1. If so, the solution is readily found. If not, one proceeds to examine zones 2 or 4 and if necessary zones 1 or 5 using Newton's Method until the solution is found. The details of this process are given in Section 3.5.

3.4 Heat Balance Equation in Mixed Conditions: With Runback

The essential concept upon which the model of mixed condition runback is based is that the liquid water and ice crystals which arrive in a particular sector, either directly by impingement from the airstream or as runback from the upstream sector, constitute a well mixed slurry. The quantities f, m and n are now defined in terms of this total ice and liquid complement of the sector (including both the directly impinging and runback fluxes). For example f is the fraction of the total liquid flux into the sector which freezes, while m is the fraction of the total ice crystal flux which melts. The quantity n is the ratio of the ice mass flux remaining in the sector to the total water substance mass flux entering the sector. It should be borne in mind that such a definition for n, which includes the runback flux, makes the numerical value of n dependent upon the angular size of the sector. Since the ice crystals are assumed to be well mixed with the liquid water, it is assumed that when a fraction f of the liquid water freezes, it traps a fraction f of the unmelted ice crystals. The unfrozen water, together with the unbonded ice crystals, continues to run back into the next downstream sector.

Figure 3.1 illustrates the input and output for a sector in each of the five thermodynamic zones outlined in Table 3.2.1. The quantities R_w^* and R_I^* are respectively the liquid water and ice crystal runback fluxes. The runback input to sector i is the output from the immediately upstream sector (i-1), while the runback output of sector i becomes the input to the downstream sector (i+1). The relationship between the input and output runback fluxes is given by the following equations:

$$R_w^{*out} = (1 - f)\,(R_w + R_w^{*in}) + m(kR_I + R_I^{*in}) \qquad (3.4.1)$$

$$R_I^{*out} = (1 - f)\,(1 - m)\,(kR_I + R_I^{*in}) \qquad (3.4.2)$$

The ice mass flux which remains in a sector is:

$$R = f\,(R_w + R_w^{*in}) + f\,(1 - m)\,(kR_I + R_I^{*in}) \qquad (3.4.3)$$

and in order to satisfy conservation of mass:

$$R_w^{*out} + R_I^{*out} + R = R_w + R_w^{*in} + kR_I + R_I^{*in} \qquad (3.4.4)$$

Consequently the re-defined ice fraction n is given by:

$$n = \frac{f(R_w + R_w^{*in}) + f(1 - m)\,(kR_I + R_I^{*in})}{R_w + R_w^{*in} + kR_I + R_I^{*in}} \qquad (3.4.5)$$

If no ice crystals melt (m = 0), then n and f are identical.

In order to calculate the thermodynamics of mixed accretion runback, it is assumed that both R_w^{*in} and R_I^{*in} enter at the equilibrium surface temperature of the immediately upstream sector i-1, namely t_s^* (c.f. Equation 2.10.2). Thus it is necessary to cool the runback mixture to the new equilibrium surface

temperature of sector i, viz. t_s, and if possible to freeze a portion of it at this temperature. The outgoing runback then leaves at the equilibrium surface temperature of sector i, namely t_s.

The heat balance equation including the effects of mixed runback can therefore be written in the form:

$$h(t_a - t_s) + h\left(\frac{Pr}{Sc}\right)^{.63} \frac{\epsilon \ell_v}{pc_p} (e_a(t_a) - e_s(t_s)) + \frac{hr_c U^2}{2c_p} + (R_w + R_I) \frac{U^2}{2}$$

$$+ (R_w \bar{c}_w + kR_I \bar{c}_I) (t_a - t_s) + ((R_w + R_w^{*in}) f - m (kR_I + R_I^{*in})) \ell_f(t_s)$$

$$+ (R_w^{*in} \bar{c}_w + R_I^{*in} \bar{c}_I) (t_s^* - t_s) = f(t_s) \qquad (3.4.6)$$

A description of the meaning of the terms follows. The first is the sensible heat transfer with the airstream, while the second is the latent heat transfer. The third is the aerodynamic heating and the fourth the kinetic energy of the impinging particles. The fifth is the heat required to warm the impinging water droplets and the sticking ice. It is assumed that the bouncing ice does not participate in the heat exchange, except to impart its kinetic energy, and that there is no splashing or shedding water, except at $\vartheta = 90°$. The sixth term is the differential latent heat term resulting from the freezing of a fraction f of the total liquid water flux and the melting of a fraction m of the total ice crystal flux. Finally, term seven is the heat required to adjust the temperature of the runback mixture to the new equilibrium value. The steady state condition is $f(t_s) = 0$. Equation 3.4.6 is solved using Newton's Method in a similar fashion to Equation 3.3.1. The details are given in Section 3.5.

The icing flux is calculated by means of Equation 3.4.5, namely:

$$R = n (R_w + R_w^{*in} + kR_I + R_I^{*in}) \qquad (3.4.7)$$

3.5 Details of the Computer Program

In order to simulate the model physical processes discussed so far for mixed icing with runback, a BASIC language computer program was written. The program logic and formulae are outlined in the flow charts contained in Figures 3.2 through 3.5(b). An annotated listing of the program itself is contained in Appendix A. A table of correspondence between program symbols and text symbols is contained in Appendix B.

4.0 CYLINDER ICING EXPERIMENTS: THE ICING WIND TUNNEL

The cylinder icing experiments were conducted in the high speed wind tunnel of the Low Temperature Laboratory, NRC, during the period August 1977 to March 1978. A summary of some of the characteristics of this tunnel, which are pertinent to these icing experiments, is presented below. Figure 4.1, adapted from Ringer (1977), shows the tunnel as it was configured for the present work.

4.1 Velocity

The wind tunnel was operated over a range of working section airspeeds from about 30 m/s to 120 m/s, the latter being close to the maximum speed which can be achieved with the present tunnel configuration. As the measuring cross-section is .30 m by .30 m, these speeds correspond to air mass fluxes of about 3.3 to 9.8 kg/s (allowing for density changes with speed). The air velocity profile in the tunnel working section is essentially flat except for wall boundary layers about .01 m thick. Although the tunnel pressure can be controlled to simulate conditions at altitude, this facility was not used. All of the experiments were undertaken with a plenum static pressure which was close to the ambient atmospheric pressure. Tunnel blockage effects (<10% of the cross-sectional area) will cause the streamline pattern about the cylinder to deviate from the ideal pattern in an infinite free stream. This difference was ignored in the model calculations.

No data on turbulence levels in the tunnel, either with or without the sprays on, are presently available. Since the heat transfer coefficient is affected by free stream turbulence (Zuskauskas, 1972), this deficiency adds a measure of uncertainty to the comparison between experimental and model icing, the heat transfer coefficient in the model assuming no turbulence in the free stream.

The plenum has a square cross-section with an area of 1.881 m^2. A rapidly converging bell mouth contraction reduces this cross-section to 0.209 m^2 over a distance of .152 m. This is followed by a more gentle linear contraction of length 1.981 m, which adjoins the measuring section (.093 m^2). The cylinder axis lies horizontally across the centre of the tunnel at a distance of 0.24 m into the working section. Because the plenum air pressure is essentially atmospheric, the pressure in the working section (and hence the simulated altitude) varies with the tunnel speed. Since rotor blade icing experiments conducted at NGTE (Swift, 1978) suggest no significant effect of altitude on the results, this pressure variation with tunnel speed was not considered to be a cause for concern.

The spray nozzle apertures are located 0.20 m downstream from the bell mouth, where the tunnel cross-section is 0.206 m^2. The injection velocity and precise location of formation of the spray droplets is unknown. Whatever these are, the droplets initially are most likely rapidly accelerated (or decelerated) until they achieve a velocity very close to that of the airstream locally. Subsequently, they will be accelerated along with the air through the remaining portion of the contraction. In order to continue to be accelerated, their velocity must lag behind that of the airstream. The magnitude of this velocity lag can be determined by solving the compressible flow equations and numerically integrating the equation of motion of the droplets (ignoring mass changes due to evaporation or condensation). Figure 4.2 shows the results of three such calculations. A 20 μm droplet is injected into the flow either with zero velocity or with the velocity of the airstream at the spray nozzles. After the first 0.3 m, the velocity history is independent of the initial conditions for this droplet size, and the droplet arrives at the measuring section lagging the airspeed by about 6 m/s. Most of this lag is recovered, however, by the time the droplet reaches the cylinder. A 50 μm droplet arrives at the working section with a

velocity lag of about 15 m/s, and at the cylinder lagging by 6 m/s (about 5%). Since this case corresponds to about the worst which can be expected in the present set of experiments (the mean air acceleration in the contraction following the sprays is about 230 g), it is reasonable to infer that little error is likely to be incurred by assuming that the droplets are travelling at the airspeed when they arrive in the proximity of the cylinder.

4.2 Temperature

The automatic tunnel air temperature controller can be set with a precision of about ±0.2°C. Its absolute accuracy varies with temperature, with a minimum error at 0°C, and a maximum of ±0.5°C at -30°C. Once a stable tunnel temperature has been achieved, the control system can generally maintain the set temperature to within ±0.5°C for the duration of an icing experiment (typically one to five minutes). The nominal operating range of the controller is +20°C to -30°C, although its use in these experiments was restricted to the interval +3°C to -15°C. The controller measures the temperature in the plenum (the total temperature). The static temperature in the measuring section, t_a, is generally cooler than this owing to the adiabatic expansion of the air accelerating within the contraction.

In a natural developing cloud, the droplet temperature is generally very close to that of the air. However, this may not always be the case in the tunnel. The water supply to the spray nozzles is usually maintained at room temperature, while the nozzle compressed air supply is typically heated to 30 or 40°C. Upon injection, the water is initially cooled through heat transfer with the nozzle air, which has undergone an adiabatic expansion through the nozzle aperture. It is found empirically that unless the nozzle air is kept sufficiently warm, some of the droplets freeze, possibly through homogeneous nucleation. Thus the actual droplet temperature upon initial contact with the tunnel air is unknown, but it must lie between the supply air temperature and -40°C. Whatever this initial spray temperature, it will in most instances probably equilibrate with that of the airstream before the spray reaches the cylinder. However, at the highest tunnel speeds, there may be insufficient time for this to occur, especially when the tunnel airstream is itself cooling by adiabatic expansion within the contraction.

In order to investigate this possibility, a droplet heat exchange model (including sensible and latent heat) was combined with the droplet dynamics model mentioned in Section 4.1. Using this model, the thermal history of a single droplet injected into the tunnel with various initial conditions was computed numerically. The results of these calculations are presented in Figures 4.3 and 4.4. The assumed plenum air conditions are a temperature of 2.5°C, a static pressure of 1013.25 mb, a relative humidity of 90%, and an airspeed of 5.55 m/s (giving a working section temperature of -5°C, and an airspeed of 120 m/s). For a 20 μm diameter droplet (Fig. 4.3), the initial transient thermal adjustment occurs sufficiently rapidly that beyond 1.5 m the temperature history is essentially independent of both the injection velocity and the injection temperature.

Subsequently, the droplet cools more slowly, and it is unable to keep pace with the more rapidly cooling air. The result is that the droplet temperature lags the air temperature by 2.4°C when it reaches the cylinder. In the case

of a 50 μm diameter droplet (Fig. 4.4), the accommodation rate is slower, and the final temperature lag at the cylinder varies between 3.1°C and 3.9°C depending on the assumed initial temperatures. It should be noted that this model considers a single droplet only, and that it does not take into account the feedback between an ensemble of droplets and the airstream. Consequently, the temperature deviations predicted by this model should be taken as an indication only that there may exist a discrepancy between the air temperature and the spray temperature at the highest tunnel speeds. This possibility needs further investigation with a more complete model. Generally, such a temperature difference would not be expected to affect the overall heat balance significantly. However, at high speeds where the total temperature is close to 0°C, such a small deviation may play a critical role in determining whether or not any ice will accrete at all.

4.3 Sprays

The droplet spray is produced with a set of four pneumatic atomizing nozzles mounted in the contraction section of the tunnel. The nozzle apertures lie in a plane 0.20 m downstream of the bell mouth, and they are symmetrically located at the corners of a square of side 0.23 m. The spray bars are covered by an airfoil housing, with spoiler bars to promote turbulence for the uniform mixing of the spray across the tunnel. The distilled water flow rate and the atomizing air pressure (generally about 100 to 400 kPa) are independently controllable, and they have been calibrated to give quite reproducible liquid water contents and median volume diameters.

The spray calibration graphs were used to determine the water flow and air pressure settings nominally required to obtain a desired liquid water content. Then with these settings, a rotating cylinder measurement was made in order to determine the actual liquid water content on the axis of the measuring section. For each spray setting used, the rotating cylinder measurement was generally taken only for the initial experiment of the day. Subsequent tests made on the same day with the same settings were assumed to have the same liquid water content as the initial run. When checked, this assumption usually turned out to be correct within better than 5%.

The rotating cylinder measurement for determining the liquid water content (Rush and Wardlaw, 1957) employs a .05 m long cylinder of diameter 2.5×10^{-3} m rotating at 1 Hz. When this cylinder is inserted into the spray at a temperature sufficiently low that no impinging water is shed from the deposit, the mass of ice accreted in a specified time interval (generally 30 or 60 s depending upon the airspeed and liquid water content) is directly relatable to the liquid water content, provided that the airspeed, ice density and mean collection efficiency of the cylinder are known. Reasonable values for the latter two quantities are generally assumed. Recently, Stallabrass (1978) has undertaken a careful study of the assumptions and sources of error inherent in the rotating cylinder measurements. He concludes that these measurements are generally accurate to better than 10%.

Using the rotating cylinder, the liquid water content distribution across the tunnel measuring section was determined for the case illustrated in Figure 4.5. The tunnel conditions were: measuring section airspeed 30.5 m/s,

air temperature -15°C, and "centreline" liquid water content 1.23 g/m^3. Actually, this centreline value is an average over the length of the rotating cylinder. In the present case, the liquid water content lies within 5% of the centreline value over the central third of the horizontal cross-section. In view of this result, comparisons between model predictions and experiments were usually based on measurements of the accretion made either at the centreline or within .05 m of it.

The spray droplet size spectrum in the measuring section was determined by means of an oiled slide sampler, at least once for each spray setting. Because of the tedious nature of the droplet counting procedure, this was not done for individual experiments. It was desired to produce a droplet spray with a median volume diameter of 20 μm. In practice the measured values were found to lie within the range 17 μm to 25 μm, depending upon the spray settings used. Some of this variation represents a real difference in the median volume diameter among various spray settings. On the other hand, some of the variability also arises from stochastic sampling errors, which Lozowski (1978) estimates to be about $6\sqrt{1000/N}$ %, where N is the total number of droplets counted in the sample. Other error sources such as droplet evaporation and coalescence, and human counting errors, may also have caused apparent variations from sample to sample. Because of all of these factors, although an attempt was made to determine how the droplet size spectrum varied across the tunnel working section, no consistent pattern was found. Since the oiled slide samples were always taken at the cylinder position, it was not necessary to adjust the measured size spectrum to take into account size changes caused by evaporation or condensation during passage along the tunnel.

The relative humidity of the tunnel air was not measured or otherwise estimated. It was assumed that in the measuring section, the air was saturated at the local static temperature. Finally, any electrical effects which may be associated with the spray production or icing (see for example Lenard, 1892) are ignored both experimentally and in the model development.

4.4 Ice Crystals

Some workers have produced ice particles for mixed condition icing experiments by grinding ice blocks with wobble circular saw blades (W. Grabe, private communication). Others have used a "snow nozzle" which produces a fine spray of frozen rather than supercooled droplets (McNaughtan, 1977). Both of these approaches produce ice particles whose shape and possibly size may not be appropriate for the simulation of many types of natural atmospheric ice crystals. Unfortunately natural ice crystals are difficult to produce in the quantities and sizes required for these experiments (up to 10 g/s with sizes of 10^{-4} to 10^{-3} m), although Iribarne (private communication) has produced small ice crystals for wind tunnel experiments by nucleating droplets with liquid nitrogen and growing them in a supersaturated cold chamber. The principal limitation to this approach is the large residence time required to grow freely falling ice crystals several hundred microns in diameter by vapour diffusion from the air.

In order to produce realistic simulations of natural ice crystals in the necessary sizes and quantities, it was decided to inject finely divided, recently fallen snow into the tunnel. This was accomplished by means of a hydraulically driven conveyor belt mechanism (c.f. Figure 4.1) contained in an insulated box. Snow with a density of about 60 to 270 kg/m^3 was collected out of doors within a few days of its fall, and placed in the dry-ice-cooled conveyor belt channel. It was carefully levelled to a depth of .02 m and then fed through an oscillating rake at a rate of 10^{-3} to 10^{-2} m/s, before falling through a vertical tube into the plenum. A flat plate was mounted below the end of this tube in order to arrest the fall of any large aggregates, and to break them up.

Figure 4.6 is a photograph of some of the ice crystals which were collected on the axis of the working section using a hollow sampling tube feeding into a cold bath of silicone oil. The individual particle sizes are in the range of about 10^{-4} to 10^{-3}m, and although they seem to have undergone some metamorphosis, they are still characterized by the large surface area to volume ratio, typical of many natural ice crystals.

The ice crystal content (ICC) of the air in the working section was varied by changing the belt speed. An initial calculation was performed, using the measured snow density, to determine what belt speed was necessary to provide a desired ICC value. Unfortunately the hydraulic drive speed varied with the temperature in the box and the condition of the belt, and it was not always possible to achieve a desired value. Consequently the ice crystal content in the working section was measured directly. This was done with a set of five aluminum sampling tubes, screw mounted at .05 m intervals on a bar fitted across the measuring section. These tubes were .05 m in length with a 5.4×10^{-3} m inside diameter and a sharp 45° outside bevelled edge in order to define a precise sampling cross-section. At speeds below 100 m/s, the tubes were initially oriented perpendicular to the flow and were then turned into the airstream to begin the sampling. At the end of the sampling period (typically a few minutes), the tubes were restored to their perpendicular position, and were subsequently removed and weighed to determine the mass of ice crystals caught. Using this mass, the known airspeed and sampling cross-section and an assumed collection efficiency of 100%, the mean ice crystal content during the sampling period was readily calculated.

The ice crystal content during a mixed icing experiment was determined by multiplying the ice crystal content, measured during the sampling run, by the ratio of the measured belt speed during the test to that during the sampling. This procedure is a valid way of compensating for the temporal variability in the belt speed provided that the snow density and thickness are homogeneous along the belt, and that the snow is conveyed without slipping. Difficulties were occasionally encountered in satisfying one or both of these requirements leading to an uncertainty in the deduced ice crystal content. If this knowingly occurred, however, it was noted in the results. Generally a full belt of snow (2 m x .3 m x .02 m) was sufficient for one or two sampling runs as well as several mixed icing experiments.

At speeds exceeding about 100 m/s, the ice crystal content in the working section consisted of both snow which had been directly injected into the plenum and recirculating particles which had already travelled around the tunnel circuit one or more times. This recirculation does not occur to any significant extent at lower speeds because the ice crystals are able to settle out in the lower section of the tunnel. For these high speed cases, the total ice crystal content was measured as before using the sampling tube array, but the array could not be restored to the perpendicular position without risking the possibility of snow loss from the tubes. Consequently the tubes were left in their sampling position while the snow drive was stopped and the tunnel air decelerated. Because of the recirculating particles, this procedure may have given rise to a small (<5%) sampling error. Based on the measured snow density and feed rate, it was possible to estimate what portion of the ice crystal content consisted of directly injected particles and what portion of recirculating snow. At the highest tunnel speed (about 120 m/s), the recirculating snow accounted for as much as 80% of the total ice crystal content. In view of this result, the procedure described above for calculating the ice crystal content during an experiment may give erroneously large estimates, because the ICC of the recirculating snow is not necessarily related in a linear fashion to the belt speed. Unfortunately no procedure is available for the direct measurement of the ice crystal content alone during a mixed icing experiment, but since the belt speed is not sufficiently reproducible, some allowance for changes in the drive speed must be made. The resolution of this difficulty, which is fortunately restricted to high airspeeds, requires further study.

An example of the ice crystal distribution across the working section both in the horizontal and in the vertical is presented in Figure 4.7 (at an airspeed of 30.5 m/s). The vertical distribution displays a maximum in the lower half of the working section, reflecting the influence of the vertical location of the injection tube mouth, and the fallspeed of the ice crystals (probably around 1 m/s). In the horizontal, the distribution is more symmetrical, but it is narrower than that for the water sprays (c.f. Figure 4.5). This may occur because the ice crystal source is more compact, but it also suggests that the turbulence is less effective in distributing these large particles for which the drag to mass ratio is likely smaller than that for the water droplets. At other tunnel speeds, the ice crystal distribution exhibits similar general characteristics, although the details change.

The velocity and temperature of the ice crystals in the measuring section have not been investigated. It is assumed that they are in equilibrium with the tunnel airstream. The crystals are injected into the tunnel with essentially no horizontal component of velocity. Their temperature as they reach the rake is monitored with a thermocouple. It was usually in the range -30 °C to -10 °C. How quickly these variables adjust to the air temperature and speed could probably be explored with a model similar to that described in Section 4.3 for the water droplets. In several instances where an icing experiment was repeated with snow of differing temperature, no apparent change in the accretion was observed. It is felt therefore that either the ice crystals equilibrate with the airstream, or that deviations in the ice crystal temperature from that of the airstream have little effect on the icing in those cases which we considered.

Finally, no attempt has been made to take into account possible electrification effects which may arise from the production, injection or collision of the ice crystals.

4.5 The Cylinder

The icing cylinder was a bakelite rod, .305 m long and .0254 m in diameter, which was mounted horizontally across the middle of the measuring section. It could be readily inserted into and removed from the measuring section, and observed through the transparent plexiglass walls. The cylinder was painted black to provide the contrast necessary for photography of the ice deposit. This had the disadvantage of giving the cylinder a rather high infrared absorptivity, which may have given rise to non-negligible radiative heat transfer effects when a floodlamp was used for illumination. Because of this possibility, floodlamp illumination was generally used for only a few seconds at a time, except during the taking of time lapse movies (see Section 5.3) when it had to be employed continuously.

The thermal conductivity of bakelite is typically 0.3 W/mK ($\pm$25%), its specific heat capacity is 1.5 x 10^3 J/kgK ($\pm$15%), and its specific gravity is 1.40 ($\pm$5%). The conductivity being about an order of magnitude lower than that of ice, it was felt that heat conduction into the interior and along the surface of the cylinder could safely be ignored.

5.0 CYLINDER ICING EXPERIMENTS: PROCEDURES

5.1 Experimental Conditions

The cylinder diameter, air temperature, airspeed, tunnel pressure (simulated altitude), liquid water and ice crystal contents, median volume droplet diameter, and ice crystal shapes and sizes were all selected with a view to simulating conditions appropriate to helicopter rotor blade icing in natural clouds. Proposed requirements for rotorcraft ice protection in periodic mixed icing conditions are summarized in Table 5.1.1 (McNaughtan, 1978). In general accordance with these criteria, the following conditions were examined.

A. Altitude

Ambient atmospheric pressure in the plenum of the icing tunnel gave rise to a working section pressure, and hence altitude, which varied with the airspeed. The maximum simulated altitude was about 1 km. It is not expected that altitude changes of this order will have any significant effects upon the icing.

B. Temperature

Measuring section static temperatures of -5°C and -15°C were selected as being representative of "warm" and "cold" icing conditions respectively. Some experiments were also run at -8°C.

C. Liquid Water Content

Three nominal liquid water contents were selected for the experiments, namely, 0.4, 0.8, and 1.2 g/m^3. The actual values measured using the rotating cylinder method were generally within ±15% of these nominal values.

D. Ice Crystal Content

Because it would have been too time-consuming to test a range of ice crystal contents for each liquid water content, and because of the difficulty in establishing precise ice crystal contents a priori, it was decided to try to match the ice crystal content with the liquid water content. Unfortunately, even this objective was not always achieved, the ice crystal and liquid water contents occasionally differing by as much as a factor of 2 or 3.

E. Median Volume Diameter

A target median volume diameter (MVD) of 20 μm was selected. Actual values lay within the range 17 μm to 25 μm.

F. Airspeed

The velocity of the airstream relative to a helicopter rotor blade varies from about zero near the hub to close to sonic speeds at the tip. Since the maximum achievable tunnel speed was approximately 122 m/s, velocities of 30.5, 61, 91.5 and 122 m/s were employed in the experiments.

The conditions in the icing tunnel were maintained as steady as possible during an icing experiment, although secular variations of a few percent were inevitable. It was not possible to simulate the cyclic variations in pitch, yaw, and airspeed which are characteristic of helicopter rotor blades when the aircraft is in forward flight, nor did we attempt to simulate centrifugal effects which would give rise to spanwise flow along the cylinder axis.

5.2 Measurements

Once an accretion had grown on the cylinder, the tunnel was stopped (and cooled when necessary to prevent melting of the accretion), and the dimensions of a section of the accretion on the tunnel axis were recorded. The forward growth at the stagnation line, or to the "horns" if a stagnation line hollow had developed, was measured with vernier calipers from the rear stagnation line of the cylinder. The circumferential extent of the icing was measured with a protractor. For smooth accretions, the precision of the forward growth measurement was about $\pm 10^{-4}$ m, while for rough accretions, it was typically ± one-half the roughness height. Because of random spanwise variations in the extent of the icing (caused by rime feather growth or runback fingers), the icing extent measurements are subject to an uncertainty of ±5°. In addition to these measurements, the sizes of peaks, hollows, and any other noteworthy features were recorded, along with the extent of any runback. Finally, a plasticene mold was made of the accretion provided that its lateral extent did not greatly exceed the cylinder diameter.

5.3 Film Records

The accretions were first photographed obliquely in order to convey an overall picture of the nature of the icing; its shape, the type of ice, surface roughness, occurrence of runback, etc. The accretions were then sectioned near the tunnel axis using a soldering iron, and half of the accretion was removed from the cylinder permitting the photography of the accretion profile. These photographs along with photographs of the plasticene mould made it possible to sketch a composite deposit outline (see Sections 6.1 and 6.2).

In order to obtain a better appreciation of the way in which the accretion builds and of the direction of growth of the ice, time lapse photographs were taken during several of the experiments. These movies were made on Ektachrome EF7242 film, using an Arriflex 16 mm cine camera driven by a two frame per second animation motor. A 500W lamp situated outside the tunnel about 0.3 m away from the cylinder was used for illumination in these experiments. Although no dramatic radiant heating effects were observed to have been caused by this photoflood illumination, the possibility that the illumination provided a small though non-negligible contribution to the overall heat exchange must be borne in mind when interpreting the data for these experiments. Most of the experiments during which the time lapse movies were made were in fact repeated at a later stage without any illumination.

During some of the mixed condition experiments, high speed movies were taken of the ice crystal collisions using a Red Lake Hycam 16 mm camera. Framing rates of up to 3000 frames per second permitted the recording of ice crystal collisions during a one to two second time interval on 100 feet of film. This speed was high enough to reveal the details of the collisions and the subsequent motion of the collision fragments, but the framing rate was too slow to "stop" the motion of the impinging ice crystals which consequently appear as streaks on the film. The camera is actually capable of operating at speeds up to 10,000 frames per second. However, such high speeds were not used because the necessary illumination quickly melted the accretion! Because of these radiant heating effects, the experiments in which time lapse or high speed movies were made have been identified in the summary of the experimental records contained in Appendix C. It was not feasible to include excerpts from these films in this treatise, since in order to appreciate fully the phenomena they record, it is necessary to see them projected.

6.0 CYLINDER ICING EXPERIMENTS: RESULTS

6.1 Liquid Water Accretion Only

A summary of the records for the cylinder icing experiments is contained in Appendix C. Not every experiment is included in this table, since some experimental conditions were repeated, while only one example of each case appears in the summary. Figures 6.1, 6.3 and 6.5 depict the ice accretions grown in liquid water conditions. The oblique photograph shows the overall character and surface features of the deposit, while the accompanying line drawing shows the shape of the accretion cross-section, as deduced from the cross-sectional photograph, and the photograph of the plasticene mould.

As is implied by the heat balance equation (2.1.1), the effect of increasing the air temperature, airspeed, or liquid water content, is to make the deposit warmer and wetter. At the lowest values of each of these parameters (t_a = -15°C, U = 30.5 m/s, and w = 0.4 g/m^3), the shape of the deposit is lenticular (see Fig. 6.1(b)), and the surface is relatively smooth, except for the low density feathers which grow forward from the region of the initial maximum impingement angle. These feathers are typical low density rime deposits produced by the impingement of drops which freeze rapidly in situ without significant spreading or flattening, thereby incorporating large air gaps into the ice structure. The appearance of the overall deposit is opaque and white.

The change in the deposit shape as the air temperature, airspeed, or liquid water content increases is not easy to explain on the basis of the heat transfer equation, since each parameter appears in several terms. The air temperature for example and the liquid water content each affect three terms, while the airspeed either directly or indirectly affects all of the terms.

Nevertheless, we will attempt to understand the effects produced by changing one of these parameters at a time, while holding the other two fixed. Let us begin by examining the effect of an increase in the liquid water content while U and t_a are held constant at 30.5 m/s and -15°C respectively (Fig. 6.1 (a) & (b)). As a result of an increase in the water mass flux R_w, the heat source terms 5 and 7 of Equation 2.1.1 will increase, and this will be only partly offset by a compensating increase in the heat sink term 3. As a result, the deposit surface temperature must rise in order to enhance the sensible and latent heat transfer terms. Less air is incorporated into the accretion, and the result is that the central portion of the deposit takes on a milky appearance in contrast to the brilliant whiteness of the lower liquid water content case (contrast Fig. 6.1(a) at w = 0.8 g/m^3 and 0.4 g/m^3). Because of the higher liquid water content, the growth of the rime feathers is also enhanced, so that while the deposit shape is still generally lenticular, its thickness does not taper smoothly to zero near the edges.

At a still higher liquid water content, the surface temperature at the forward stagnation line reaches zero, the ice is clear (glaze), and runback begins (see Fig. 6.1(a) for w = 1.2 g/m^3). At this stage, the runback does not interfere significantly with the growth of the rime feathers (except perhaps to fill in some of the interstices), and these features remain quite pronounced. The effect of the runback on the shape is to give rise to a rough depression at the forward stagnation line, and as the runback water freezes further along the cylinder circumference, a pair of ridges is formed. In profile, these ridges give the impression of horns, and they are sometimes referred to as horned icing. An interesting aspect of this accretion is that a transition from smooth to horned growth occurs about half way between the centre line of the tunnel and the wall. This is presumably a consequence of the variation in the liquid water content across the tunnel. With the aid of Figure 4.5, it is found that the transition point corresponds to a liquid water content of 1.1(3) g/m^3 (when U = 30 m/s, and t_a = -15°C).

At a fixed air temperature, the transition from smooth to horned growth occurs at a lower liquid water content as the airspeed is increased. For example, at -15°C and 61 m/s, the growth at 0.8 g/m^3 already exhibits a horned growth

quite similar to that which occurs at 30.5 m/s and 1.2 g/m^3, while at 122 m/s runback effects are already in evidence at 0.4 g/m^3. In each of these cases, the runback flux is insufficient to obscure the growth of the rime feathers which may be seen quite prominently above and below the "wet" central portion of the accretion. Initially, the rime feathers begin to grow outwards, but after a few minutes they start to grow inwards relative to the free stream direction. This change in their growth direction may be seen particularly explicitly in the time lapse movies. The growth direction of the rime feathers is a consequence of the interaction between the mean droplet impingement direction and the shape of the surface. Initially the surface is convex and the rime feathers grow outwards because they are shielded from growth along the droplet impingement direction by the upstream growth. Later, however, as the accretion surface flattens, they begin to grow inwards along the mean direction of the droplet trajectories.

Under still wetter conditions (e.g. 61 m/s and 1.2 g/m^3) the runback region is quite broad and flat, and the horns develop further from the stagnation line so that they begin to interfere with the rime feather growth. At 122 m/s and 0.8 g/m^3 the feathers become quite glazed by the runback. Finally at 122 m/s and 1.2 g/m^3 the runback and horn growth completely inhibit any significant development of the rime feathers. The deposit profile is quite flat where it faces the airstream, a slight hollow occurs at the stagnation line, and the horns now extend laterally beyond the diameter of the cylinder. The appearance of the ice is milky and large air bubbles can be identified. It is interesting that in those cases where runback was occurring, the deposit had a tendency to develop a flat forward surface after a few minutes. Such a profile will probably enhance the drag considerably, while shedding of runback water from the horns probably helps to account for their rapid icicle-like growth. Not only will the horns experience an enhanced heat transfer with the airstream because of their small radius of curvature, but List (1977) has also suggested that the shedding of water from surface protuberances may act as an additional sink in the heat balance equation. Possibly because of this water shedding, there were no cases at -15°C where the runback travelled around to the rear surface of the cylinder.

The ice accretions grown at -5°C (Fig. 6.3(a)&(b)) are quite different from those grown at -15°C. Runback occurs under all experimental conditions, so that the rime feathers which characterized much of the growth at -15°C are almost entirely absent. Glazed icicle-like fingers growing in the same location as the rime feathers may, however, be seen in the accretions grown at 30.5 m/s and 0.8 g/m3, and at 61 m/s and 0.4 g/m^3.

At the lowest speed and liquid water content (30.5 m/s and 0.4 g/m^3), the deposit retains a smooth lenticular shape. The ice is transparent and so appears dark in the photographs, although because of cooling of the accretion or deformation of the cylinder subsequent to the growth, the ice has separated in places from the cylinder surface leaving air gaps which have a whitish hue. As the liquid water content is increased while the velocity is held constant at 30.5 m/s, the surface texture of the ice becomes rough or pebbly. The contour of the surface remains convex although the radius of curvature increases with time.

The -5°C results are similar to those at -15°C, inasmuch as an increase in speed (with constant LWC) gives rise to analogous changes in the accretion to an increase in LWC (with constant airspeed). As an example of this, one may observe the similarity between the deposits grown at 30.5 m/s and 0.8 g/m^3 and at 61 m/s and 0.4 g/m^3, or between those grown at 61 m/s and 0.8 g/m^3 and at 91.5 m/s and 0.4 g/m^3. At 61 m/s, an increase in the liquid water content makes the surface rougher, and icicle-like horns begin to develop, enhancing the cross-sectional area of the accretion perpendicular to the free stream. At the same time, a depression starts to appear at the forward stagnation line. At 91.5 m/s and 0.4 g/m^3 the deposit continues to be glazy and pebbly, much like those grown at lower airspeeds. However, as the liquid water content increases at this airspeed, the ice begins to take on quite a different character. Rather little ice growth occurs near the forward stagnation line, while a substantial open ice structure with a jagged appearance develops around the 45° position on the circumference. The resulting ice accretion might be termed a very rough horned type of growth. An interesting feature of the ice grown at 91.5 m/s and 0.8 g/m^3 was long pointed isolated protuberances (some as long as .01 m) which grew almost perpendicular to the flow. The precise growth mechanism of these protuberances is not understood, although it is suspected that their rapid growth results from a high heat transfer rate (because of their small size) coupled with a high flux of runback water to their tip followed by water shedding. Because of the fragility of these features, they were occasionally seen to break off and be shed into the airstream. Such ice shedding was even more in evidence at a liquid water content of 1.2 g/m^3. The photograph of this deposit shows a large section missing from the lower horn, which had broken off during the course of the icing experiment. Finally, at 122 m/s, ice grows only near the 90° position and only in small amounts. The aerodynamic heating is too great to permit ice build-up anywhere in the upstream facing sector of the cylinder. The extent and amount of this icing is rather insensitive to the liquid water content, the growths at .4 g/m^3 and 1.2 g/m^3 being quite similar. Again in these cases self-shedding of ice was observed during the course of the experiments.

A special set of experiments was performed at 110 m/s and -8°C with liquid water contents of 0.13, 0.28 and 0.65 g/m^3 (Fig. 6.5). These were undertaken in order to simulate icing trials performed at NGTE, Pyestock, on rotor blade sections (B. Perks, private communication). In these British experiments, a substantial difference was observed between an ice accretion grown at 110 m/s, -8°C and an LWC of 0.65 g/m^3, and one grown at 110 m/s, -8°C, an LWC of 0.2 g/m^3 and an ICC of 0.8 g/m^3. Our experiments were performed to investigate whether this difference might have resulted from the mechanical and thermodynamic effects of the ice crystals, or whether it could be ascribed mainly to the difference in the liquid water content alone. These conditions were also of interest because they represent an intermediate temperature between the -5°C and -15°C cases already considered, and because the accretions grown under these conditions are close to the point at which significant stagnation region icing ceases to occur because of aerodynamic heating, while a substantial ice build-up can still occur away from the stagnation region.

At the low liquid water content (0.13 g/m^3) the deposit outline resembles that grown at -15°C, 122 m/s and 0.4 g/m^3. The central portion is glaze ice with a small indentation along the stagnation line, while the outer portion

consists of rather delicate rime feathers. The principal differences between the two are that in the present case the rime feathers are more fragile in appearance, while the central portion of the deposit is both very smooth and extremely transparent. It is so clear in fact that individual ice crystals can be seen embedded in it. These ice crystals are blown off the turning vanes and cooling coils at these high speeds and they continue to circulate around the tunnel. Their concentration, however, is sufficiently low that they probably have a negligible influence on the icing process.

At a liquid water content of 0.28 g/m^3, the surface becomes pebbly, with a flat front and a wide cross-section normal to the free stream. The rime feathers are almost completely obscured by the runback. The deposit shape is similar to that grown at 122 m/s, -15°C and 1.2 g/m^3. Finally, at 0.65 g/m^3, the deposit is very rough with a large central depression and horns which extend outward into the flow. In response to the original question about these latter two cases, it is evident that a substantial difference between them occurs because of the LWC difference alone.

6.2 Mixed Accretions

Not all of the icing experiments performed with liquid water conditions were repeated under mixed conditions. However, an effort was made to include the same range of conditions. Ideally a variety of ice crystal contents should have been examined for each liquid water content value, but this was not feasible owing to a lack of time and the difficulty of obtaining a desired ice crystal content. As a result, only one ICC value was employed for each LWC case, an attempt having been made to equalize the two values. Both the ice crystal and liquid water contents are specified in the mixed condition deposit photographs which are assembled in Figures 6.3, 6.4 and 6.5. These figures show an oblique view of the deposit as well as a cross-sectional sketch, which is based on the photographs of the sectioned accretion and of the plasticene mould.

Generally, the deposits grown under mixed conditions show some evidence of having grown cooler and drier than their liquid water counterparts. The ice is more milky or opaque and the surface roughness appears to be diminished. In many instances, however, the overall shape and growth rate of the accretions do not differ substantially from the corresponding liquid water only cases. For this reason, it seemed most appropriate to compare the liquid and mixed accretions on the basis of the same liquid water content, rather than by comparing those grown under the same total water content (both liquid and solid).

On this basis, notable differences among the liquid and mixed deposits were seen to occur in three cases: (a) 61 m/s, -5°C and an LWC of 1.2 g/m^3, (b) 122 m/s, -15°C and an LWC of 0.4 g/m^3, and (c) 110 m/s, -8°C and an LWC of 0.28 g/m^3. In case (a) the mixed condition accretion is superficially less rough than the corresponding liquid water growth, but it incorporates many large air bubbles and cavities giving it a slushy, milky appearance. In cases (b) and (c), the mixed condition deposits are quite similar in appearance - even though the corresponding liquid water deposits look to be very different. The outlines of these accretions suggest that the ice particles have had a considerable shaping influence, though the precise mechanism by which this comes

about requires further investigation. It is tempting, however, to speculate that this effect may be attributable to the interaction of a mechanical and thermodynamic process associated with the ice crystals.

The smooth "aerodynamic" streamlining of the lateral surfaces of the accretion suggests a possible erosion process which wears down the feathery rime that might otherwise grow outwards in this region. Possibly the hollow along the stagnation line is the result of the splashing of runback liquid water caused by the impaction of the ice crystals. There must be a critical liquid water or ice crystal content (or both) for this to occur because the hollow does not extend along the entire length of the cylinder. This splashing, if it occurs, will be complicated by the secondary flow established within the cavity. Finally, the enhanced growth of the horns near to the stagnation line is no doubt the result of all these influences. However, it may be initiated by the enhanced heat sink associated with the impinging ice crystals.

Since the deposits were not weighed, a direct comparison between the average mass growth rates in liquid and mixed conditions cannot be made. However, this can be estimated (assuming similar ice densities) by measuring the cross-sectional area of the photographs of the accretion in the two cases. In both cases (b) and (c), the ratio of the liquid accretion cross-sectional area to the mixed accretion area was 1.3 $\pm$0.05. Thus the effect of the ice crystals in these two cases has been to reduce the overall mass growth rate by about 25%, and to redistribute the remaining deposit mass in a more streamlined fashion. Drag measurements probably should be made on shapes such as these in order to verify whether there is indeed a drag reduction accompanying these apparently more streamlined shapes.

6.3 Thin Sections

Thin sections of some of the accretions cut perpendicular to the cylinder axis were made in the fashion described by Timco (1978). A similar procedure used for making thin sections of hailstones has been outlined by List (1961). The thin sections were photographed in transmitted light to show the bubble patterns, and between crossed polaroids to reveal their crystal fabric. It was hoped that such structural information would cast light upon the nature of the ice growth processes occurring during accretion. The results for three cases, 59C, 72C and 70CM are presented in Figures 6.6 through 6.8.

Figure 6.6, corresponding to case 59C (-8 °C, 110 m/s, LWC 0.13 g/m^3), does not contain a transmitted light view of the thin section. Instead, two crossed polaroid views are shown to illustrate the change in apparent crystal structure which occurs when the section is microtomed from a thickness of about 1 mm (lower picture) to about 300 μm (upper picture). In the thicker section, the bubble patterns are more apparent. However, in the thinner section the grain boundaries are sharper and the crystal shapes and sizes are consequently better defined. This result illustrates that it is important when investigating the crystal fabric to employ a thickness which is commensurate with the minimum crystal dimensions, and consistent from case to case. Unfortunately, in the three cases treated here, the precise section thicknesses are unknown, and this will tend to confound the interpretation of the crystal structures.

Case 59C is an example of slow ($\sim 9\ \mu ms^{-1}$) accretion growth at a probable surface temperature in the stagnation region of 0°C, but without a significant surface water accumulation or runback flux. The crystals formed in the central region of the deposit under these circumstances are relatively large (according to the classification scheme of Levi and Aufdermaur (1970)), and elongated more or less along the growth direction of the deposit. In this respect, they bear some resemblance to the grains formed in bulk ice during slow, one-dimensional growth at the ice-water interface. Typically the crystals are 1 to 10 mm long and .5 to 2 mm wide. The crystals in the vicinity of the rime feathers are smaller, although these too appear to have a preferred orientation along the growth direction. A higher bubble density is evident in this outer region, while in the central region, bubbles are almost totally absent. This observation is consistent with the overall clarity of the deposit's central region as shown in Figure 6.5.

Another feature of this accretion, which is also typical of the other two accretions considered in this section, is a layer of thickness about 0.5 mm to 1 mm adjacent to the cylinder, in which the crystal and bubble structures are different from those of the overlying ice. In order that this layer not be confused with the layer of re-frozen melt water which arises when the accretion is melted onto the glass slide, the thin section photographs have been cut out so as to include only the accretion itself. In the case of accretion 59C, crystals in this "surface" layer appear to be smaller, and more bubbles are included in the overlying deposit. In addition the crystal boundaries tend to be oriented perpendicular to the surface giving this layer a "regular" appearance compared with the more "random" appearance of the overlying ice. Ackley et al (1978) has also noted a distinct "surface" layer of comparable thickness in ice deposits grown on a whirling steel cylinder. He ascribes its occurrence to the influence of the initial heat conduction into the cylinder (thermal conductivity about 15 W/mK), whereas the comparatively poor thermal conductivity of ice (about 2 W/mK) subsequently reduces the internal heat conduction. Since the thermal conductivity of the bakelite cylinder is about 0.3 W/mK, such an explanation is unsatisfactory for the present results. A more likely explanation is that initially the impinging water droplets are unable to nucleate to form ice. As a result, a thin layer of liquid water develops on the surface, and its comparatively slow rate of freezing gives rise to the unique crystal and bubble structure of the surface layer. Of course it may also be that the tunnel spray conditions settle down after an initial transient, but this explanation is considered to be unlikely. Since the growth of this layer for the three cases considered takes place during the first 15 to 30 seconds following the initiation of icing (based on the layer thickness and the overall average growth rate), it may be an important consideration for the thermodynamics of de-icing or anti-icing. Some effort should therefore be expended to further elucidate the physics of this initial layer.

Figure 6.7 illustrates the thin sections of accretion 72C. This case is similar to 14C, but it was grown for twice as long (5 min.) in order to produce an accretion of manageable dimensions for thin sectioning. Here again, the deposit in the stagnation region was probably growing at 0°C, but the growth rate was about four times that of case 59C. The "surface" layer is about 1 mm thick in this instance, and it is characterized by an absence of

air bubbles. The 3 mm thick layer above this in the central region consists of long, narrow crystals (typically about 1.5 to 3 mm long and about .5 mm wide) and relatively small concentrations of air bubbles which tend to form lines directed inwards at about 8° to the free stream direction. Since the direction of growth of the deposit is an important consideration for modelling, it would be valuable to know whether the orientation of the bubble lines characterizes the growth direction as it does in bulk ice. More work needs to be done to answer this question. A third layer of thickness about 7 mm overlies the previous two. It is characterized by large numbers of small crystals typically 200 to 500 μm in maximum dimension, and it has a greater bubble density than the layer below it. The bubbles in this layer are small and again tend to be oriented in lines or bands, this time at about 22° to the free stream direction. The bands appear to focus on the stagnation line as the growth proceeds so that the bubbly ice segment becomes successively narrower. It is suspected that the transition between the second and third layers is associated with the transition from a convex to a concave icing surface, although this hypothesis requires further testing. If this should be the case, and if the differing structures of the two layers imply different thermodynamic regimes, this will have important consequences for modelling. It means in fact that in order to model accurately the thermodynamics and consequently the growth over periods of several minutes, the effects of the change in shape of the growing accretion cannot be ignored. A fourth, less bubbly layer, about 1 mm thick, occurs right at the surface of the deposit. This may have been formed during final freezing of the surface liquid layer after the sprays were turned off.

The ice structure in the outer regions of this accretion is different from that in the interior. This is the growth region of the rime feathers, and the loose, open structure of the rime is reflected in the long lines of bubbles parallel to the surface, and the occasional large bubble. The very large bubble near the right hand side of this accretion is probably air trapped between the ice and the glass slide, and should be ignored. The crystals in this region, as might be expected, are small, although it must be kept in mind that these structures do not necessarily accurately reproduce the original structures of the rime region. Melting of the rime feathers and re-crystallization of the melt water while the accretion is being attached to the slide will significantly change the structure of outer portions of the thin section.

Figure 6.8 depicts the thin section of accretion 70CM, which was grown under conditions similar to those of case 47CM, but with a somewhat lower ice crystal content (0.7 g/m^3 compared with 1.0 g/m^3). It was hoped that by comparing this thin section with that of case 72C (Figure 6.7), some evidence of the effects of ice crystal impingement would be seen. Unfortunately, as far as the crystal fabric is concerned, this does not seem to be the case. The crystals in this thin section appear to be uniformly small (about 250 to 500 μm in maximum dimension), and no larger (1 to 2 mm) crystals typical of those in the airstream are evident. One interpretation of this result, which is consistent with the high speed movie observations, is that the airborne ice crystals break up on impact, and that only a small fraction remains embedded in the surface, the rest splashing away.

In this thin section also, there is a suggestion of an initial bubble free layer, about 0.5 mm thick, which forms adjacent to the cylinder surface. The overlying layer has a bubbly central portion, but unlike the second layer in Figure 6.7, the bubbles here are not clearly oriented in bands. In the outer region of the deposit, the long lines of bubbles almost certainly indicate the growth direction of the rime feathers, which is about 15° to the free stream direction and about 18° to the slope of the surface. Whereas in case 72C, the rime feathers were growing parallel to the surface, in this case the growth direction is inclined to the surface, suggesting a possible erosion effect by the ice crystals. Since this shape is apparently more streamlined than that of accretion 72C, further effort should go into determining whether or not the shape is indeed dictated by erosion. Because accretion 70CM was grown for only 2.5 minutes, its forward growth is smaller than that for case 72C. Nevertheless, it has already undergone a transition from a convex to a concave surface, but this transition does not appear to be reflected in the crystallography or the bubble structure.

Although much of the discussion in this section has perforce been tentative, it does suggest that a careful, systematic study of the internal structure of ice accretions grown under helicopter icing conditions could pay off in an improved understanding of the mechanisms of accretional growth. In this connection, the body of knowledge which has been built up concerning hailstone structural interpretation (e.g. Macklin, 1977) should certainly not be ignored.

6.4 Movie Data

Tables 6.4.1 and 6.4.2 summarize the experimental conditions for which time lapse and high speed movies were made. Neither of these sets of films has been quantitatively analyzed at present. However, certain qualitative observations based on these films will be recorded here.

First, the time lapse movies indicate that the direction of growth of the accretions is predominantly forward. In those cases where rime feathers develop along the edges of the deposit, their initial growth direction is canted outwards, but after a few minutes they usually begin to grow inwards. Likewise, depressions in the stagnation area bounded by "horns" also appear to grow inwards, so that the width of the depression diminishes with time. This observation is consistent with the inward orientation of the bubble lines in the thin section of accretion 72C for example (c.f. Figure 6.7). Another significant impression gained from the time lapse films is that the general character of the deposit seems to be established in the first 30 to 60 seconds or so of growth, and that the growth during the next several minutes continues to maintain the same overall character. This result suggests that despite the effect which shape changes may have on the detailed growth mechanics and thermodynamics of the accretion, it may not be unreasonable to extrapolate the initial growth rate, as predicted by the model, to estimate the growth after several minutes.

Many of the high speed movies were underexposed because of difficulties with the framing rate control of the camera. Nevertheless in most of the films it is possible to observe the impact of many individual crystals, and thereby

gain an initial insight into the ice crystal accretion process. One of the first impressions gained from these movies is that the ice crystal trajectories are very close to being straight lines. If this result is verified by careful quantitative analysis, it will mean that the assumption that the ice crystal collision efficiency is given by $\beta_{Ii} = \cos \theta_i$ is correct for particles of this size. The second qualitative observation that can be made is that many of the impacting ice crystals bounce off the surface whether it is wet or dry, leaving no apparent residue in the accretion. A small fraction of the particles, chiefly the larger crystals and possibly conglomerates, hit the surface and are observed to splash leaving an identifiable ice residue in the surface. The splashed material which is probably predominantly ice, though it may contain liquid water, is generally carried away in the airstream. Occasionally a splashed particle is seen to re-impinge upon the surface, frequently only to bounce again. This observation helps to explain why the mass and dimensional growth rates of the mixed accretions are not substantially different from the corresponding rates in pure liquid water clouds. Because the high speed movies were focussed on the central portion of the accretion, they contain no apparent evidence which might help to resolve the question of whether the streamlining, which occurs in cases such as 70CM, is the result of rime feather erosion by the ice crystals.

7.0 COMPARISON OF EXPERIMENTAL AND MODEL RESULTS: MODEL VERIFICATION

7.1 Basis of the Comparison

The model and the observations will be compared in two ways. First, a comparison will be made for all the experimental cases undertaken at -5°C and -15°C, between the stagnation icing rate predicted by the model and that measured in the experiments. Then, for certain illustrative cases, a comparison will be made between the experimental accretion profile and the model-predicted profile obtained by extrapolating in time the initial growth rate as a function of angle around the cylinder. By simply extrapolating the initial icing rates predicted by the model, important time-dependent effects such as the continuous influence of the shape change on the heat transfer coefficient, the collection efficiency and the angular location at which runback shedding occurs, cannot be taken into account. In the model, the collection efficiency is fixed in time, and the liquid water shedding occurs only at 90°. In addition, the heat transfer coefficient was based on a simplified rough heat transfer formulation, unless it was clear from the experiments that the surface was very smooth (roughness $\ll$ about $.01D_c$).

Both of these comparisons are unrealistic because the model predictions are strictly valid only at the beginning of the icing, whereas the observations are based on icing effects integrated over several minutes. In order to make a comparison, therefore, either the model icing rates must be extrapolated over the period of the particular experiment, or the total experimental growth must be averaged to obtain a mean icing rate which can be compared with the model initial prediction.

Another difficulty encountered in converting the model predictions into growth profiles is the assumption it is necessary to make regarding the ice density and the growth direction. The model yields icing fluxes R in kg/m^2s for each 5° sector of the cylinder. The surface area of these sectors per unit

length is $(5\pi r_c/180)m^2$ where r_c is the cylinder radius. Thus the ice mass growth rate per unit sector length is $(R5\pi r_c/180)kg/s$. In order to convert this quantity into a volume growth rate, an ice density must be assumed. For convenience, a constant value of $\rho_I = 890\ kg/m^3$ is chosen, although this is clearly not appropriate in the vicinity of the rime feathers. Thus the volume growth rate will be $R5\pi r_c/180\rho_I$. The profile is now determined by the direction of the growth, which in turn will depend on whether the deposit is wet or dry. For dry deposits, the rime feathers indicate that the growth direction near the maximum impingement angle is approximately forward (i.e. parallel to the free stream). Near the stagnation line it must also be forward. Consequently, if forward growth is assumed in the intervening portion of the deposit as well, the accretion thickness in the forward direction at an angle θ on the surface of the cylinder is given by $h = R\Delta t/\rho_I \cos\theta$.

When the surface is wet, and runback occurs, a more realistic approximation might be to assume radial growth. In this case, h, defined now as the radial accretion thickness, is given by:

$$h = \frac{2\frac{R\Delta t}{\rho_I}}{1+\sqrt{1+\frac{4R}{\rho_I D_c}}} \qquad (7.1.1)$$

If h is small compared with the cylinder diameter, the expression above reduces to $h \doteq R\Delta t/\rho_I$. This is the expression which has been used to establish the model predicted profiles, even though the assumption that $h \ll D_c$ is not always valid. Naturally, any such errors in the assumed density and growth directions can be expected to affect the correspondence between the model and the experimental profiles.

In comparing the profiles of the model and experimental accretions, the measured experimental values of the liquid water content, air temperature, and airspeed have been inserted into the model. However, in order to standardize the model results and because the droplet size spectrum was not measured for each experiment, a standard droplet size spectrum with a median volume diameter of about 20 μm has been incorporated into the model. This spectrum, based on Cansdale and McNaughtan (1977), has f_j values of .06, .10, .19, .29, .18, .08, .05, .035 and .015 for j = 1 to 9 respectively (see Section 2.2).

Another method of verifying the model predictions, which is free of time-dependent effects, might be to compare the model-predicted surface temperatures with measured initial surface temperatures. Although we have not made such measurements, they have been made by Cansdale (private communication), and a comparison with these results is planned in a subsequent publication.

7.2 Liquid Accretion: Stagnation Growth Rate

Figures 7.1 through 7.4 compare the stagnation icing growth rates predicted by the model with the experimentally determined values for a number of conditions. For consistency, the model predictions were made for liquid water contents of exactly 0.4, 0.8 and 1.2 g/m^3. Since the experimental liquid water contents were not integral multiples of 0.4 g/m^3, it was necessary, in order to

make a fair comparison, to adjust the experimentally observed growth rates by multiplying them by the ratio of the appropriate idealized liquid water content to the observed liquid water content.

At -15°C and an LWC of 0.4 g/m^3, the growth profiles are essentially smooth and lenticular for airspeeds of 30.5 and 61 m/s. Under these conditions, good agreement is found between the model predicted growth and that observed (Fig. 7.1). The model predicts that a transition from dry to wet growth will occur between 60 and 120 m/s, and the accretion photographs (Figure 6.1) appear to confirm this. In all three cases, however, the model prediction is about 5% low. For the two dry growth cases, this can only occur if the measurements are consistently in error (an unlikely possibility for these smooth accretions), the Langmuir and Blodgett collection efficiencies are erroneous (see a comment on this possibility by List (1977)), or the liquid water content measured by the rotating cylinder is too high. Stallabrass (1978) has recently shown that an error of this magnitude and sign could possibly arise in the rotating cylinder measurements. Whatever the error source, however, it is encouraging that the total discrepancy is no larger than about 5%. Thus unless larger errors fortuitously cancel out, this suggests that both the rotating cylinder measurements and the Langmuir and Blodgett collection efficiencies at the stagnation point are probably accurate to 5% or better.

At a liquid water content of 0.8 g/m^3 (Figure 7.2), the model predicts the transition from dry to wet growth to occur between 30.5 and 61 m/s, and this is consistent with the observations. Once again, the stagnation icing rate is slightly underpredicted for the dry case, but a more significant underforecast occurs at 60.5 and 122 m/s. There are several potential explanations for this discrepancy. First, the measurements may be overestimates of the true average growth because of the surface bumps. This is unlikely to account for such a large deviation, especially as care was always taken to measure to the bottom of the hollow if the profile near the stagnation line was concave. The effect of the changing profile on the collection efficiency is not a promising explanation either. In these cases the profile becomes flatter without much change in its lateral extent. A comparison of Langmuir and Blodgett's data for cylinders and flat plates suggests that such a trend would in fact decrease the collection efficiency by a few percent. A third possibility is the effect of roughness on the heat transfer coefficient. The model assumes that roughness will enhance the stagnation line heat transfer by about 25%. This enhancement may not be large enough in view of the hypothesis of Schuepp (1968) that large roughness elements may enhance the heat transfer in proportion to the additional surface area they create. If the bumps for example were spherical caps compacted together in a square lattice, the surface area would increase by about 80% over that of a flat surface. In view of this possibility, the model may be underpredicting the heat transfer coefficient and hence the icing rate. Still another explanation might be that the ice has a lower density than that assumed because of the incorporation of large quantities of air bubbles. The appearance of the ice accretions, however, makes this an unlikely possibility. Finally, it may be that the ice accretion is growing "spongy" and incorporating unfrozen liquid water into the ice matrix. This would have the effect of increasing the measured ice volume without changing its thermodynamics. The occurrence of spongy ice seems to have been mentioned first by Fraser, Rush and Baxter (1952), while

its significance for hail growth was first appreciated by List (1959). The dashed line in Figure 7.2 and subsequent figures in this series illustrates the growth which would be predicted by the model if the ice were spongy, incorporating the specified percentages of liquid water. Alternatively, the dashed line may be interpreted as the growth which would occur if an enhanced rough heat transfer permitted a fixed percentage increase in the icing rate (subject of course to the availability of impinging water and neglecting the density difference between ice and liquid water). Since the dashed curves fit the two higher points rather better than the solid ones, it is suggested that either spongy ice or an enhanced heat transfer are the most likely explanations for at least some of the discrepancy between the model and experimental values. In future experiments, it may be possible to look for evidence of spongy ice growth in thin sections using the approach of Knight and Knight (1973). Unfortunately, no potentially spongy cases were included in the thin sections discussed in Section 6.3.

At a liquid water content of 1.2 g/m^3 (Figure 7.3), a qualitatively similar but even larger discrepancy to that described above occurs between the model and the experimental values. The list of possible explanations need not be repeated. However, in this case it is not so obvious which explanations are the most likely ones. If the spongy ice explanation is invoked for example, the dashed curve continues to represent wet growth, but no runback occurs until the break in the curve. On the other hand, if the enhanced heat transfer explanation is invoked, the steeply rising part of the dashed curve represents dry growth. In either event, it would be difficult on this basis to explain the runback effects which are quite apparent in the accretion photographs of case 19C (Fig. 6.1(a)). In this case, the transition from dry to wet growth is predicted by the uncorrected model (solid line) to occur at about 30.5 m/s and a liquid water content of 1.20 g/m^3, when the air temperature is -15°C. This is quite consistent with the result of Section 6.1, in which the experimental transition was determined to have occurred at a liquid water content of 1.13 g/m^3 for an identical air temperature and speed. In summary then, although the model appears to be able to make certain reasonable predictions of the stagnation line growth rate at -15°C, and although it can be empirically modified to agree well with other observations in the 30.5 to 122 m/s airspeed range, it still needs to be placed on a more secure physical foundation before one can confidently make use of its present predictions or extrapolate them to other conditions.

At -5°C (Figure 7.4), the unadjusted model prediction of stagnation line growth rate is in very poor agreement with the observations, except for the single "just wet" case at 30.5 m/s and 0.4 g/m^3, and at 91.5 m/s, where the apparent agreement may be fortuitous since the model and experimental results appear to be crossing at this velocity. At intermediate speeds the model significantly underpredicts the growth rates while above about 90 m/s, it tends to overpredict them. The underprediction at intermediate speeds may have a similar origin to that occurring in wet growth at -15°C. For this reason dashed curves for specified sponginess values or additional ice accretion percentages are included. These dashed curves do appear to give a better prediction than the basic model in this velocity range, but their prediction is even poorer than that of the unadjusted model at high speeds. Above 90 m/s the model overpredicts

the stagnation line icing rate. Such a discrepancy has also been noted by Stallabrass (1958) in comparisons between his stagnation line icing model and rotor blade icing measurements, although in these cases additional factors may have been involved. The explanation of this anomaly is elusive. In the wind tunnel, it may be that the droplets are not completely in thermal equilibrium with the air, being somewhat warmer (c.f. Section 4.2). However, this explanation is less likely to be able to account for the Stallabrass observations. A more likely explanation may lie with the model assumption of equilibrium or quasi steady state thermodynamics of the accretion. Such a hypothesis ignores the fact that the nucleation of ice, being a stochastic process, may take some time to occur after the supercooled droplets have impinged. The high runback fluxes under these conditions may not allow the liquid sufficient residence time at the stagnation line to nucleate and grow sufficiently to adhere to the surface. In addition, the freezing fractions in these cases are small so that any nucleated ice crystals may simply be swept away with the runback flow rather than adhering to the cylinder. If this should be the case, the model must be modified to take such non-equilibrium effects into account. A final possibility for the model overprediction at high airspeeds may be splashing loss of liquid water as the droplets impact at high velocities into the thin layer of surface water (Joe et al, 1976; Macklin, 1977). This could lead to a loss of water and a lower growth rate than that of the model. Possibly some of the splashed water may re-impinge upon the icicle lobes enhancing their growth rate.

7.3 Liquid Accretion: Ice Profiles

The model predicted ice profiles for a number of cases, which typify the range of profile types encountered in the experiments, are compared with the experimental profiles in Figures 7.5 through 7.7. Figure 7.5 illustrates the profiles of three liquid water accretions which were grown at -15°C. The model profiles are the smooth ones, in contrast to the experimental profiles which are typically rough. The model prediction for case 17C (30.5 m/s and 0.4 g/m^3) compares well with the experimentally observed profile. An even better agreement might be expected if the model growth had been assumed to be forward (as seems likely in this case) rather than radial. The absolute maximum impingement angle predicted by the model is 80°, while at 75° the growth rate is only 1% of that at the stagnation line. This result compares well with the measured maximum impingement angle of 75°. Thus in dry growth the model predicted profile is quite reasonable.

In wet growth, a reasonable agreement between model and experiment is achieved in case 14C (122 m/s and 0.4 g/m^3). Here the occurrence of a hollow at the stagnation line and horned growth further out is qualitatively well predicted, although the model horns develop too far away from the stagnation line. The feathery rime near the maximum impingement angle will tend to be underpredicted because an ice density of 890 kg/m^3 is assumed, and overpredicted because the growth is plotted radially. In this case, these two effects fortuitously appear to cancel each other so that the model profile, even in this region, is in fair agreement with the observations.

Case 16C (122 m/s and 1.2 g/m^3) is another one where the model profile (when suitably adjusted) is not in bad agreement with the observed profile. The model runback leads to a large ice accumulation back to 80°

(dashed line), where the growth becomes dry in the model. A similar growth is observed experimentally, although the horns are sharper than the smooth growth of the model, possibly because they begin to experience icicle-like growth through the shedding of runback water into the airstream. In the model, runback water is not allowed to blow off until it reaches an angle of 90°. Truncating the model at 65° in order to simulate this effect gives a profile (solid line) more in keeping with the observed one. An even better model representation could perhaps be obtained by connecting the point of maximum growth (50°), where one might expect the greatest shedding to occur, to the maximum impingement angle by a straight line.

Figure 7.6 illustrates two accretions at -8°C. Case 59C (0.13 g/m^3 and 110 m/s) was modelled using the smooth heat transfer coefficient, and the growth was plotted forward. The stagnation line hollow is simulated (although too wide) but the lateral growth is not well represented. This is probably because the low density of the rime fingers is not properly accounted for. Case 58C (0.65 g/m^3 and 110 m/s) is generally well simulated if the runback is cut off at 65° in order to allow for water shedding from the horns. The stagnation line depression is well represented, but the model horns are larger than those observed, again probably because of an inadequate accounting for blow-off water.

As was the case for the stagnation line growth rate, the model profile predictions are poorest at -5°C (Figure 7.7). The profile for case 60C (30.5 m/s and 1.2 g/m^3) is underpredicted at the stagnation line and overpredicted in the lobes. In addition the model fails to simulate the observed runback in streams beyond 90°. In fact, it predicts that the growth becomes dry at 65°, whereas the accretion photograph (Figure 6.3) clearly shows runback streams to 110° or even further. The resolution of this particular discrepancy between the model and experiment will not be simple. Increasing the overall heat transfer to enhance the stagnation line growth rate would simply make the accretion drier than it is at present. On the other hand, lowering the heat transfer coefficient to permit enhanced runback would have the undesirable effect of diminishing the stagnation line growth even further. It would therefore seem necessary to increase the rough heat transfer coefficient at the stagnation line and to decrease its value at higher angles in order to simulate adequately the experimental results. It is not clear however what the physical justification for doing this might be. Perhaps there is a non-equilibrium nucleation effect because of the high runback fluxes to the horns. The problem requires further investigation.

Case 61C (91.5 m/s and 0.4 g/m^3) is better represented by the model in the sense that the stagnation line depression with lateral bulges is simulated approximately. The bulges are located at too high an angle, but this is probably the result of plotting the growth radially for an interval over which it is not valid to extrapolate. Finally, Case 63C (91.5 m/s and 1.2 g/m^3) is not well predicted by the model, although the suggestion of a stagnation line hollow with a great deal of runback beyond 90° is qualitatively correct. The profile is truncated at 90° because the model assumes incorrectly in this case that runback beyond this angle is blown off. In view of the actual appearance of the accretion with large icicle-like horns, it is perhaps not surprising that the model fails to predict this type of growth well.

Seen as a whole, these results indicate that although the model is not always quantitatively accurate in predicting the liquid water accretion profiles, it does generally give a good qualitative prediction of the type of profile to expect, i.e. whether or not horns will occur, if there will be a stagnation line depression and so on. Certainly in most instances, such as case 58C for example, it gives better indication of the total amount of icing than could be gained simply by trying to extrapolate on the basis of the stagnation line icing only, with runback neglected.

There are several reasons for the discrepancies between the model and the observed profiles. In ascending order of importance these are:

1. Deviations in tunnel parameters from their measured or nominal values, e.g. velocity, liquid water content and droplet size spectrum.
2. Measurement errors due to surface roughness.
3. Profile errors due to melting during sectioning, non-centering of the section, pulling of the plasticene during removal, and so on.
4. Errors in assumptions about the heat transfer coefficient and recovery factor for cylinders due to unknown tunnel turbulence, and inadequate observations of rough heat transfer for roughness appropriate to cylinder icing.
5. Time dependent, and hence shape dependent, effects upon all the mechanical, aerodynamic and thermodynamic parameters of icing, including possible non-equilibrium nucleation effects.
6. Inadequate simulation of splashing and shedding of runback water.

7.4 Mixed Accretion

Only two mixed accretion cases are considered in Figures 7.5 and 7.7. These are case 47CM (122 m/s, -15°C, LWC of 0.4 g/m^3, and ICC of 1.0 g/m^3) and case 45CM (30.5 m/s, -5°C, LWC of 1.2 g/m^3, and ICC of 1.2 g/m^3). A comparison of the predicted and observed profiles for these two cases quickly demonstrates that something is seriously wrong with the model assumptions for mixed condition icing. The problem is with the assumption that when the growth is wet, all the impinging ice crystals stick, or at least enough of them to make the deposit "just dry". Consequently very large model icing rates can be achieved, because of the mass of these sticking crystals, and because of their thermal capacity which allows more of the impinging liquid water to freeze. Thus in case 45CM (Fig. 7.7), huge lobes develop in the model which are not evident in the experiment. In fact the experimental profile in this case is not very different from the liquid water only profile, with which the model gives reasonable agreement. Similarly in case 47CM (Fig. 7.5), a large nose develops in the model around the stagnation line where ice crystals adhere to the accretion. At higher angles however the growth is dry, no ice crystals stick, and the growth rate is substantially lower.

The possibility of this type of rapid growth in mixed conditions, which is exemplified by the model predictions, is the reason why a concern was originally expressed about helicopter icing in clouds containing both liquid water droplets and ice crystals. In fact, as the high speed movies and the experimental profiles indicate, not nearly all of the ice crystals adhere to the surface even when it is wet. For these conditions which we have examined

therefore, it seems that mixed condition cylinder icing need not pose as serious a concern as had been suspected. Because it is clear that the model must be modified in order to take into account the bouncing and splashing of the ice crystals (and perhaps their erosion effects too), no further comparisons will be made here between the model and experimental profiles in mixed condition icing.

7.5 Implications for Model Development and for Further Experiments

In view of the comparisons between the model and experimental results, the following recommendations are made with a view to improving the model predictions and making them more relevant to helicopter rotor blade icing, and to performing critical experiments which will elucidate the growth mechanisms of the ice accretion and provide the necessary parametrical input to the model. We have not attempted to establish an order of priority for these recommendations since the priority will depend upon one's objectives. Some are short-term projects, while others may require development over several years.

A. Further Experiments

1. Experiments need to be undertaken to determine the local heat transfer coefficient of realistically rough cylinders over a Reynolds and Mach number range appropriate to helicopter icing. How rough the cylinders need to be depends upon the growth interval of concern. For anti-icing calculations, a smooth surface is appropriate, for de-icing considerations, growth roughness developed over 30 seconds to a minute is of concern, while for an unprotected condition, one may need to simulate the growth roughness achieved after several minutes of icing.

2. It would be informative to undertake experiments to determine whether spongy ice occurs under the icing conditions discussed in Section 7.3. An examination of the isotopic, crystallographic and bubble structures of the ice (Macklin et al, 1977) may be an appropriate means for doing this.

3. An examination should be made of the secondary flow and particle trajectories in the stagnation line depression, especially the deep valleys which develop under certain mixed conditions.

4. Turbulence levels in the high speed tunnel need to be measured as they may have an influence on the heat transfer.

5. The physical behaviour of the accretion during what seems to be an initial nucleation delay period is poorly understood. This effect may be particularly important in wet growth conditions at high speeds where no ice grows at the stagnation line. High speed and time lapse cinematography would help to elucidate the mechanisms acting here.

6. A more detailed study should be made of the ice crystal impingement process, including sticking, splashing, re-impingement, and surface flow of ice crystals. The effect on these processes of crystal size, shape and state of

aggregation also requires to be investigated, in its relation to the thickness of the surface water film. Again high speed photography may be helpful in elucidating these questions on the microscale. Mass growth measurements would be beneficial on the macroscale. It may also be informative to make a comparison between mixed condition growth with snow crystals as described in the present work, and with frozen droplets produced by a "snow" nozzle.

7. A greater range of mixed conditions needs to be examined in future experiments. It is of particular importance to examine the effect on the growth of varying the ice crystal concentration, in those cases where significant shape changes are seen. In this connection, better measurement and reproducibility of both the ice crystal content and its distribution is required. This is especially necessary for those conditions where the concentration of recirculating snow is high.

8. It would be interesting to make a comparison between cylinder and airfoil icing under similar environmental conditions. It is expected that the differing pressure distribution about the two bodies, especially at high Mach numbers, may give rise to significant airfoil icing under conditions where little or no ice grows on the cylinder.

9. In order to assess the aerodynamic significance of various ice accretion shapes, it is necessary to make wind tunnel or in situ measurements on airfoils or rotor blades with simulated ice accretions attached.

10. An examination of the growth of ice as a function of time should demonstrate to what extent time-dependent effects need to be taken into account in the model. It may be possible to illustrate the time dependent shape in thin sections by inserting cold thin marker layers in the accretion at fixed intervals (see for example Thwaites, Carras and Macklin, 1977).

11. It would be useful to look for evidence of water droplet splashing at the high speeds and temperatures where the model overpredicts the stagnation line growth.

B. Model Development

1. Sensitivity experiments could be undertaken with the model to determine what are the most critical conditions for further icing experiments. Such experiments would also help to determine the measurement accuracy required in the liquid water content, etc. in order to make meaningful comparisons between the model predictions and experimental observations.

2. New experimental parameters and results should be incorporated into the model wherever this is feasible. Of particular importance is an improved formulation for the rough heat transfer coefficient.

3. It should not be too difficult to amend the model so that shedding of runback water occurs near the maximum growth point of the horns rather than entirely at 90°.

4. Further effort should be devoted towards incorporation into the model of such effects as (a) the initial nucleation delay, (b) non steady-state effects, and (c) internal heat conduction for metallic substrates.

5. A comparison should be made between the model predicted surface temperatures and the temperature measurements of Cansdale, for example, under both dry and icing conditions.

6. The model predicted and experimental profiles need to be compared for a greater number of conditions than have been considered in Sections 7.3 and 7.4.

7. A graphical display of the model profiles (on a CRT terminal for example) would save time in making comparisons with the experimental profiles, as well as permitting a quicker evaluation of the effects of varying the model parameters.

8. The incorporation of time dependence into the model, or the determination of empirical relations between model predicted initial icing parameters and the final experimentally observed parameters, would help to avoid the present naive extrapolation of model initial values over periods of time for which this is not valid.

9. The latent heat exchange term should be re-derived, examining the assumptions made along the way. Total and vapour pressure changes during adiabatic compression or expansion at high Mach numbers should be allowed for.

10. The final development of the model would be to apply it to the case of a helicopter rotor blade. In addition to an airfoil shape with its own peculiar collection efficiency and heat exchange, it would be necessary to consider angle of attack, centrifugal and Coriolis forces, oscillatory pitch, yaw and velocity, and possibly also interaction among the rotor blade elements.

8.0 CONCLUSIONS

8.1 Principal Conclusions

Quite a number of significant results have arisen during the course of this work and these have been pointed out in the body of the report. They will not all be summarized here. However, in order to pull together the main points, and to assess the significance of what has been accomplished, the following principal conclusions are drawn.

1. Non-rotating cylinder icing under dry conditions over a short period (long enough to accrete about .1 to .2 inches at stagnation on a 1" cylinder) leads to basically lenticular growth with a few rime feathers near the edge. This type of growth is well predicted by the model. Under these conditions, the stagnation line growth is also a good indicator of the overall growth.

2. Non-rotating cylinder icing under wet conditions is dominated by liquid water runback effects. These include stagnation line hollows, horned growth varying from small surface ridges to large icicle type lobes, and

liquid water shedding. Under these conditions, the stagnation line growth is not generally a good indicator of the overall growth. The model, however, gives reasonable qualitative predictions provided the growth is not too wet, a significant deterioration in the predictability occurring at high velocities and temperatures.

3. Contrary to prior expectations, mixed condition icing, under the limited range of conditions investigated here, does not lead to greatly enhanced icing rates. The net effect of the addition of ice crystals to the air stream in some cases may even be a small reduction in the mass growth rate coupled with an apparent streamlining of the profile, perhaps due to erosion.

4. Further icing experiments need to be undertaken, and there is considerable scope for improving the model predictions. These efforts should be undertaken in accordance with the recommendations attached in Section 7.5.

5. The present work demonstrates that a combined modelling and experimental approach, supplemented by experience from helicopter icing trials, is more effective in developing an understanding of and a prediction capability for helicopter icing than is any approach undertaken in isolation.

8.2 Implications for Helicopter Rotor Blade Icing

As there are many aspects of helicopter rotor blade icing that are not simulated in either the model or the experiments, it is not possible to extrapolate the results of this work in an entirely unambiguous fashion to the helicopter rotor blade icing problem. Nevertheless, the present results do suggest at least two important implications for rotor blade icing which deserve to be more fully investigated.

First, mixed condition icing appears to be not so serious a problem as had been suspected, at least over the range of conditions considered in the present work.

Second, the type of icing which occurs at warm temperatures (around -5°C) and high speeds (90 to 120 m/s in the present experiments), with little or no stagnation line icing, but large icicle lobes extending laterally, may pose a potential hazard for helicopter rotor blades. These lobes may be even more exaggerated and occur under even warmer conditions (higher total temperature) for an airfoil than they do in the cylinder, due to adiabatic cooling of the airflow in the low pressure zone on the upper portion of the airfoil. Unfortunately, it is precisely in this location where even a small amount of ice may have the most serious consequences for the aerodynamic performance of the airfoil.

9.0 REFERENCES

1. Achenbach, E., 1974: Heat transfer from smooth and rough surfaced circular cylinders in a cross flow. Proceedings of the 5th International Heat Transfer Conference, Tokyo, 229-233.

2. Ackley, S. F. and M. K. Templeton, 1978: Numerical simulation of atmospheric ice accretion. Paper presented at the 2nd International Symposium on Snow Removal and Ice Control Research, Hanover, N. H., May 1978, 27 pp.

3. Ackley, S. F., G. E. Lemieux, K. Itagaki and J. O'Keefe, 1978: Laboratory experiments: the icing of rotating blades. Paper presented at the 2nd International Symposium on Snow Removal and Ice Control Research, Hanover, N. H., May 1978.

4. Brownscombe, J. L. and J. H. Hallett, 1967: Experimental and field studies of precipitation particles formed by the freezing of supercooled water. Quarterly Journal of the Royal Meteorological Society, 93, 455-473.

5. Cansdale, J. T., and I. I. McNaughtan, 1977: Calculation of surface temperature and accretion rate in a mixed water droplet/ice crystal cloud. Royal Aircraft Establishment Technical Report 77090, 24 pp.

6. D'Amours, R., 1977: A numerical model for heat transfers during hailstone icing. Unpublished M.Sc. thesis, University of Alberta, 112 pp.

7. English, M., 1973: The growth of large hail. McGill Stormy Weather Group Scientific Report MW-78.

8. Fraser, D., C. K. Rush and D. Baxter, 1952: Thermodynamic limitations of ice accretion instruments. NRC NAE Laboratory Report LR-32.

9. Joe, P. I., R. List, P. R. Kry, M. R. de Quervain, P.Y.K. Lui, P. W. Stagg, J. D. McTaggart-Cowan, E. P. Lozowski, M. C. Steiner, J. von Niederhavsern, R. E. Stewart, E. Freire, G. Lesins, 1976: Loss of accreted water from growing hailstones. Proceedings of the International Conference on Cloud Physics, Boulder, 264-269.

10. Kloner, M. O., 1970: Prediction of ice formations on an airfoil, Lockheed California Co. Report No. LR 23993, December 24, 1970, 22 pp.

11. Knight, C. A., and N. C. Knight, 1973: Quenched, spongy hail. Journal of the Atmospheric Sciences, 30, 1665-1671.

12. Lake, Sqn. Ldr. H. B., and J. Bradley, 1976: The problem of certifying helicopters for flight in icing conditions. Aeronautical Journal, October 1976, 419-433.

13. Langmuir, I., and K. B. Blodgett, 1946: A mathematical investigation of water drop trajectories, AAF Technical Report No. 5418, 47 pp.

14. Lenard, P., 1892: Über die Elektrizität der Wasserfälle. Annalen der Physik, 46, 584.

15. Levi, L., and A. N. Aufdermaur, 1970: Crystallographic orientation and crystal size in cylindrical accretions of ice. Journal of the Atmospheric Sciences, 27, 443.

16. List, R. J., 1951: Smithsonian Meteorological Tables, Sixth Revised Edition. Smithsonian Institution, 527 pp.

17. List, R., 1959: Wachstum von Eis-Wassergemischen in Hagelversuchskanal. Helvetica Physica Acta, 32, 293.

18. List, R., 1961: Physical methods and instruments for characterizing hailstones. Bulletin of the American Meteorological Society, 42, 452.

19. List, R., 1977: Ice accretions on structures. Journal of Glaciology, 18, 375-388.

20. Lowe, P. R., 1977: An approximating polynomial for the computation of saturation vapour pressure. Journal of Applied Meteorology, 16, 100-103.

21. Lozowski, E. P., 1978: Stochastic effects in spray droplet sampling with oiled slides. NRC Low Temperature Laboratory Memorandum LT-172, 17 pp.

22. Ludlam, F. H., 1951: The heat economy of a rimed cylinder. Quarterly Journal of the Royal Meteorological Society, 77, 663-666.

23. Macklin, W. C., 1961: Accretion in mixed clouds. Quarterly Journal of the Royal Meteorological Society, 87, 413-424.

24. Macklin, W. C., 1977: The characteristics of natural hailstones and their interpretation. In: Hail: a review of hail science and hail suppression. Edited by G. B. Foote and C. A. Knight. Meteorological Monographs, 16, 65-88.

25. Macklin, W. C., C. A. Knight, H. E. Moore and N. C. Knight, 1977: Isotopic, crystal, and air bubble structures of hailstones. Journal of the Atmospheric Sciences, 34, 961-967.

26. Macklin, W. C., and G. J. Metaxas, 1976: Splashing of drops on liquid layers. Journal of Applied Physics, 47, 3963-3970.

27. Macklin, W. C., and G. S. Payne, 1967: A theoretical study of the ice accretion process. Quarterly Journal of the Royal Meteorological Society, 93, 195-213.

28. McNaughtan, I. I., 1977: Ice and snow in the atmosphere. Royal Aircraft Establishment, Technical Memorandum EP 594, 10 pp, 6 figs.

29. McNaughtan, I. I., 1978: Atmospheric conditions for helicopter icing protection design. Paper presented at NATO Panel X Symposium on Helicopter Icing, London, November 1978.

30. Messinger, B. L., 1953: Equilibrium temperature of an unheated icing surface as a function of airspeed. Journal of the Aeronautical Sciences, 20, 29-41.

31. Pellet, J. L., and A. S. Dennis, 1974: Effects of heat storage in hailstones. Preprints of the Conference on Cloud Physics, Tucson, 63-66.

32. Ray, G. V., 1978: Techniques for icing test flying. Paper presented at NATO Panel X Symposium on Helicopter Icing, London, November 1978.

33. Ringer, T. R., 1977: Icing test facilities in Canada. Unpublished paper presented at Round Table Discussion on Icing - AGARD Fluid Dynamics Panel meeting, Ottawa, September 1977.

34. Rush, C. K., and R. L. Wardlaw, 1957: Icing measurements with a single rotating cylinder. NRC NAE Laboratory Report LR-206, 8 pp. 13 figs.

35. Schlichting, H., 1968: Boundary-layer theory. Sixth Edition. McGraw-Hill, New York, 747 pp.

36. Schuepp, P. H., 1968: Studies of the local heat and mass transfer of spherical hailstone models. Proceedings of the International Conference on Cloud Physics, Toronto, August 1968, 416-421.

37. Seban, R. A., 1960: The influence of free stream turbulence on the local heat transfer from cylinders. Journal of Heat Transfer, 82, 101-107.

38. Stallabrass, J. R., 1957: Icing flight trials of a Bell HTL-4 helicopter. NRC NAE Laboratory Report LR-197.

39. Stallabrass, J. R., 1958: Icing flight trials of a Sikorsky H04S-2 helicopter. NRC NAE Laboratory Report LR-219.

40. Stallabrass, J. R., 1978: An Appraisal of the single rotating cylinder method of liquid water content measurement. NRC Report LTR-LT-92.

41. Stallabrass, J. R., and E. P. Lozowski, 1978: Ice shapes on cylinders and rotor blades. Paper presented at NATO Panel X Symposium on Helicopter Icing, London, November 1978.

42. Swift, R. D., 1978: See discussion on paper "Icing test facilities at the National Gas Turbine Establishment. NATO, AGARD Conference Proceedings No. 236, Icing Testing for Aircraft Engines, Paper No. 4.

43. Thwaites, S., J. N. Carras, and W. C. Macklin, 1977: The aerodynamics of oblate hailstones. Quarterly Journal of the Royal Meteorological Society, 103, 803-808.

44. Timco, G. W., 1978: Morphological characteristics of ice grown from an impure melt. NRC Division of Mechanical Engineering Report LTR-LT-91.

45. Tribus, M., 1952: Modern icing technology. Lecture notes. Engineering Research Institute. University of Michigan.

46. Werner, J. B., 1973: Ice protection investigation for advanced rotary-wing aircraft. U. S. Army Air Mobility Research and Development Laboratory Technical Report 73-38.

47. Zukauskas, A., 1972: Heat Transfer from tubes in crossflow. In: Advances in Heat Transfer, 8, 93-160.

10.0 ACKNOWLEDGEMENTS

One of the authors, E. P. Lozowski, wishes to acknowledge the roles played by the University of Alberta and the National Research Council in making it possible to undertake the work described here during a study leave year. Many individuals have contributed to the success of this endeavour. In particular we wish to thank Mr. G. W. Wood of the Low Temperature Laboratory, whose assistance with the design of the snow feed system was invaluable, and Mr. J. T. Cansdale of the Royal Aircraft Establishment, with whom we have had many stimulating discussions concerning helicopter icing.

TABLE 2.2.1

The Langmuir-Blodgett parameter λ/λ_s as a function of droplet Reynolds number Re.

Re	λ/λ_s (Langmuir & Blodgett)	λ/λ_s (Equation 2.2.4)
0	1.0000	1.0000
1	.9200	.9118
3	.8273	.8371
10	.6905	.7048
30	.5281	.5425
100	.3524	.3553
300	.2234	.2149
1000	.1215	.1128
3000	.0624	.0594
10000	.0262	.0285

TABLE 2.2.2

Droplet impingement parameters β_o, E, and ϑ_m as a function of the non-dimensional variables K and ϕ. The values to the left of the oblique are estimated from Eqs. 2.2.5, while those to the right are taken from the graphs of Langmuir and Blodgett (1946).

	K \ ϕ	0	10	10^2	10^3	10^4
β_o	.2	.137/.136	.126/.127	.116/.114	.100/.096	.079/.077
	.5	.381/.379	.351/.349	.325/.320	.282/.277	.224/.221
	1	.556/.557	.518/.517	.483/.480	.425/.421	.344/.342
	5	.841/.840	.806/.809	.772/.785	.713/.739	.622/.662
	10	.909/.910	.877/.891	.850/.873	.801/.837	.720/.773
	50	.980/.981	.967/.973	.953/.951	.926/.951	.875/.921
	100	.990/.991	.982/.986	.973/.981	.955/.971	.919/.951
E	.2	.021/.021	.018/.017	.015/.014	.011/.010	.006/.004
	.5	.179/.189	.152/.156	.130/.128	.097/.091	.060/.052
	1	.389/.385	.342/.343	.294/.292	.225/.227	.146/.149
	5	.761/.759	.706/.720	.656/.678	.573/.613	.459/.493
	10	.864/.863	.819/.832	.775/.796	.698/.736	.582/.638
	50	.970/.969	.949/.954	.929/.940	.888/.911	.816/.850
	100	.985/.984	.971/.974	.958/.966	.930/.945	.879/.904
ϑ_m°	.2	13.4/13.5	12.3/12.3	11.3/11.2	9.8/9.5	7.7/7.8
	.5	38.9/38.9	35.8/35.5	32.9/32.4	28.3/27.7	22.2/22.0
	1	56.9/56.9	53.2/53.1	49.7/49.1	43.6/41.2	35.0/34.0
	5	80.0/80.0	77.6/77.4	75.2/74.9	70.7/68.6	63.0/60.5
	10	84.1/84.3	82.3/82.1	80.6/80.3	77.2/76.1	71.3/69.0
	50	88.9/88.8	88.1/87.9	87.2/86.8	85.4/85.1	82.2/81.2
	100	89.4/89.4	88.9/88.9	88.4/88.1	87.3/87.3	85.0/84.1

TABLE 3.2.1

Zone	t_s °C	f	k	m	Remaining Ice	Runback Water R_w*out	Runback Ice R_I*out	n
1	<0	1	0	0	$R_w+R_w{}^*in+R_I{}^*in$	0	0	1
2	0	1	0 to 1	0	$R_w+R_w{}^*in+kR_I+R_I{}^*in$	0	0	1
3	0	1 to 0	1	0	$f(R_w+R_w{}^*in) + f(R_I+R_I{}^*in)$	$(1-f(R_w+R_w{}^*in)$	$(1-f)(R_I+R_I{}^*in)$	f
4	0	0	1	0 to 1	0	$R_w+R_w{}^*in + m(R_I+R_I{}^*in)$	$(1-m)(R_I+R_I{}^*in)$	0
5	>0	0	1	1	0	$R_w+R_w{}^*in + R_I+R_I{}^*in$	0	0

Icing parameters for a sector in the five thermodynamic zones defined in Fig. 3.2.1

TABLE 5.1.1

Definition of design atmospheric icing conditions
for periodic mixed condition encounters

air temperature °C	water/ice content g/m^3	median volume drop diameter μm	altitude range km
0	0.3/0.9	20	0 to 3
-10	0.2/0.7	20	0 to 3
-20	0.15/0.3	20	0 to 3

TABLE 6.4.1

Experimental conditions under which high speed movies were taken of the ice crystal accretion process

Case	Airspeed m/s	Temperature °C	LWC g/m^3	ICC g/m^3	Corresponding case in Appendix C
54 CM	30.5	-15	.4(0)	.9	46 CM
50 CM	30.5	-15	.4(6)	.6	36 CM
67 CM	30.5	-13.5	.4(0)	.5	46 CM
70 CM	122	-15	.4(4)	.7	47 CM
69 CM	30.5	-5	1.2(0)	1.2	45 CM
68 CM	91.5	-5	.3(8)	.3	68 CM

TABLE 6.4.2

Experimental conditions under which time lapse movies were taken of the accretion growth

Case	Airspeed m/s	Temperature °C	LWC g/m^3	Corresponding case in Appendix C
19C	30.5	-15	1.2(3)	4C
10C	61	-15	.7(8)	20C
24C	61	-15	.7(8)	20C
12C	61	-15	1.2(5)	12C
14C	122	-15	.4(4)	14C
16C	122	-15	1.2(7)	16C
9C	61	-5	.4(6)	9C
11C	61	-5	.7(8)	11C
13C	61	-5	1.2(5)	13C
15C	122	-5	.4(4)	15C

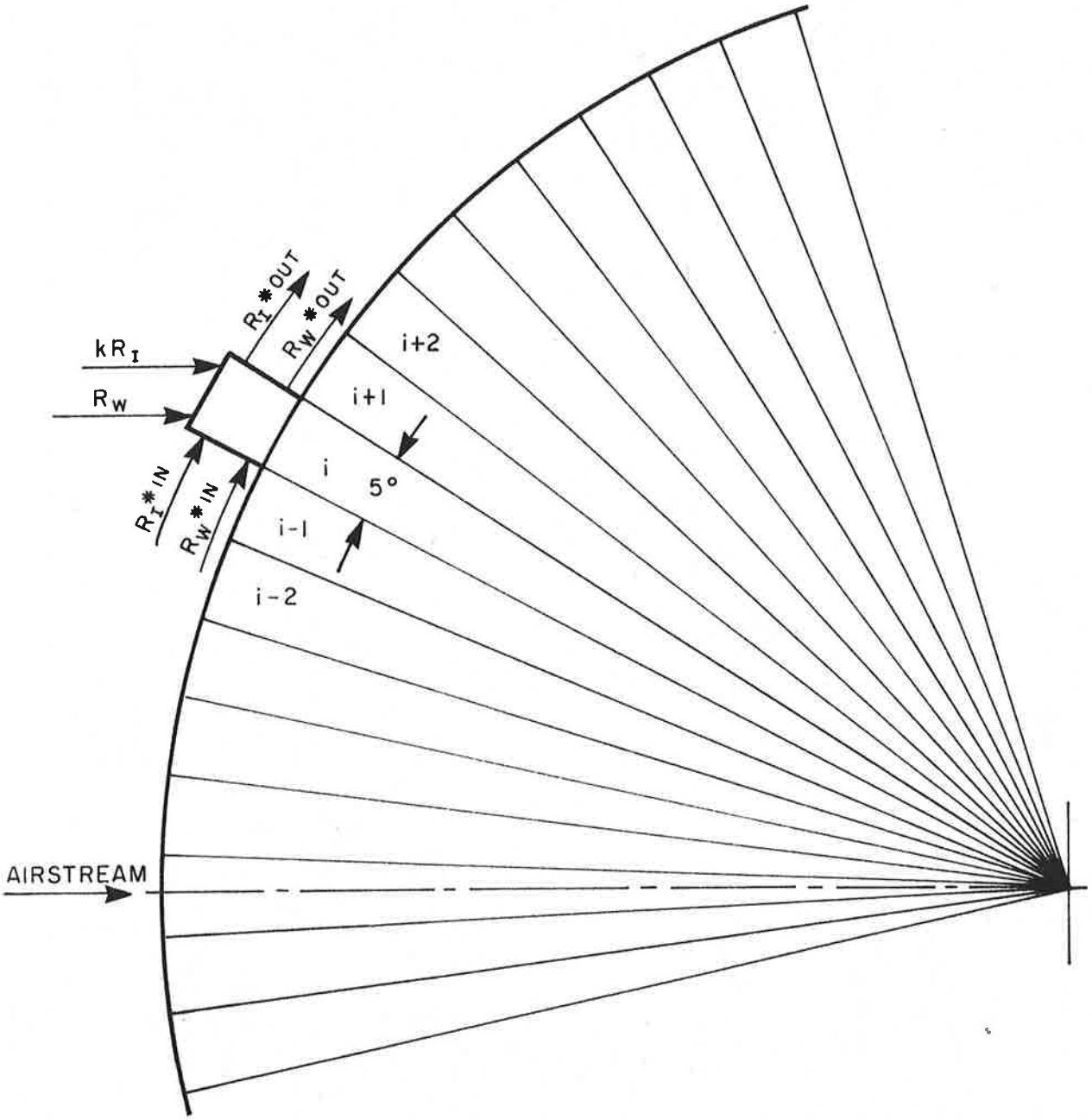

FIG. 3.1: NET DIRECTLY IMPINGING FLUXES, AND RUNBACK FLUXES INTO AND OUT OF THE ith 5° SECTOR ON THE CYLINDER SURFACE

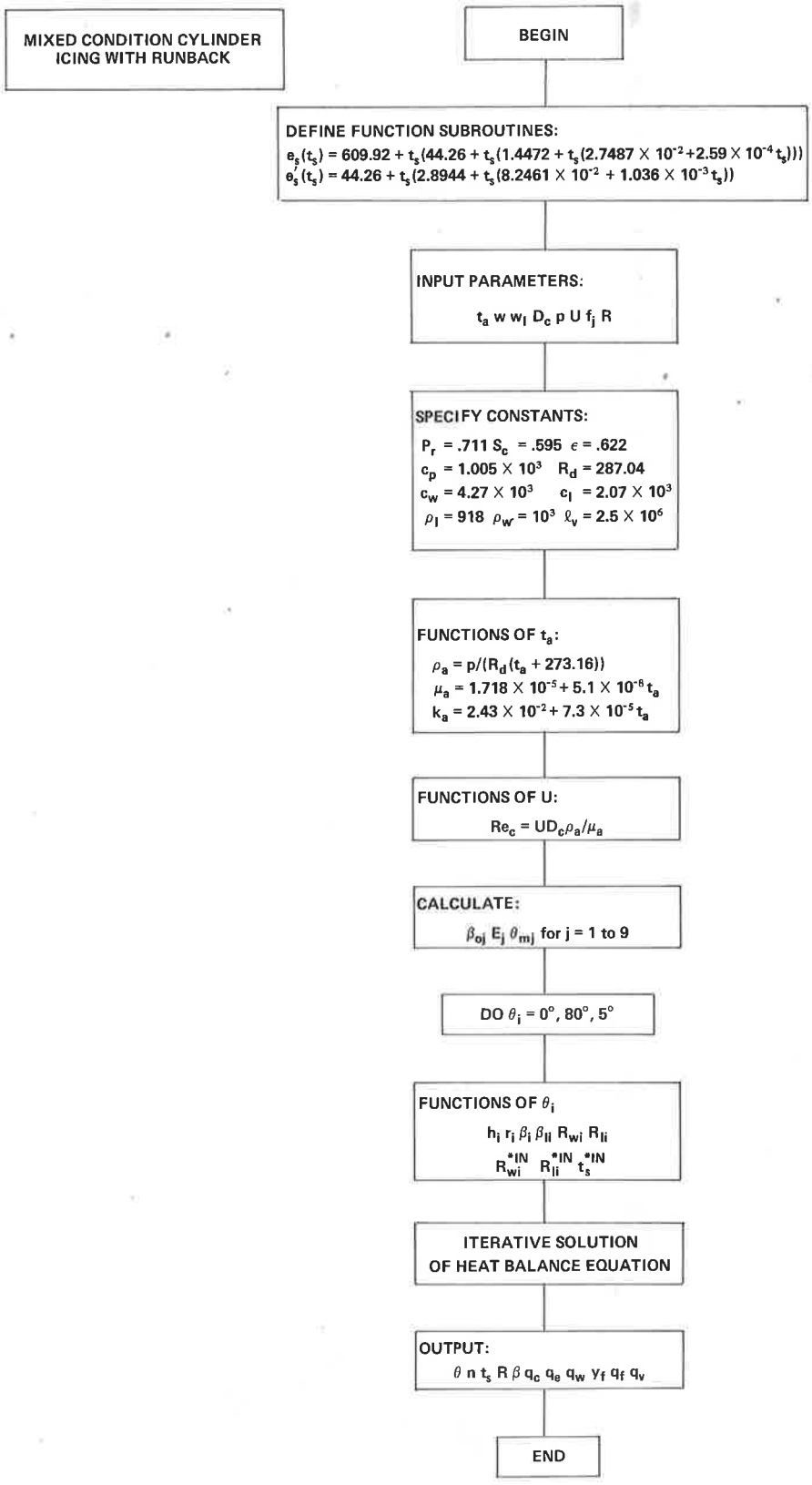

FIG. 3.2: BLOCK FLOWCHART FOR PROGRAM WHICH SIMULATES INITIAL CYLINDER ICING UNDER MIXED CONDITIONS WITH RUNBACK

INDIVIDUAL BLOCKS ARE EXPANDED, WHERE NECESSARY, IN FIGS. 3.3 TO 3.5(b)

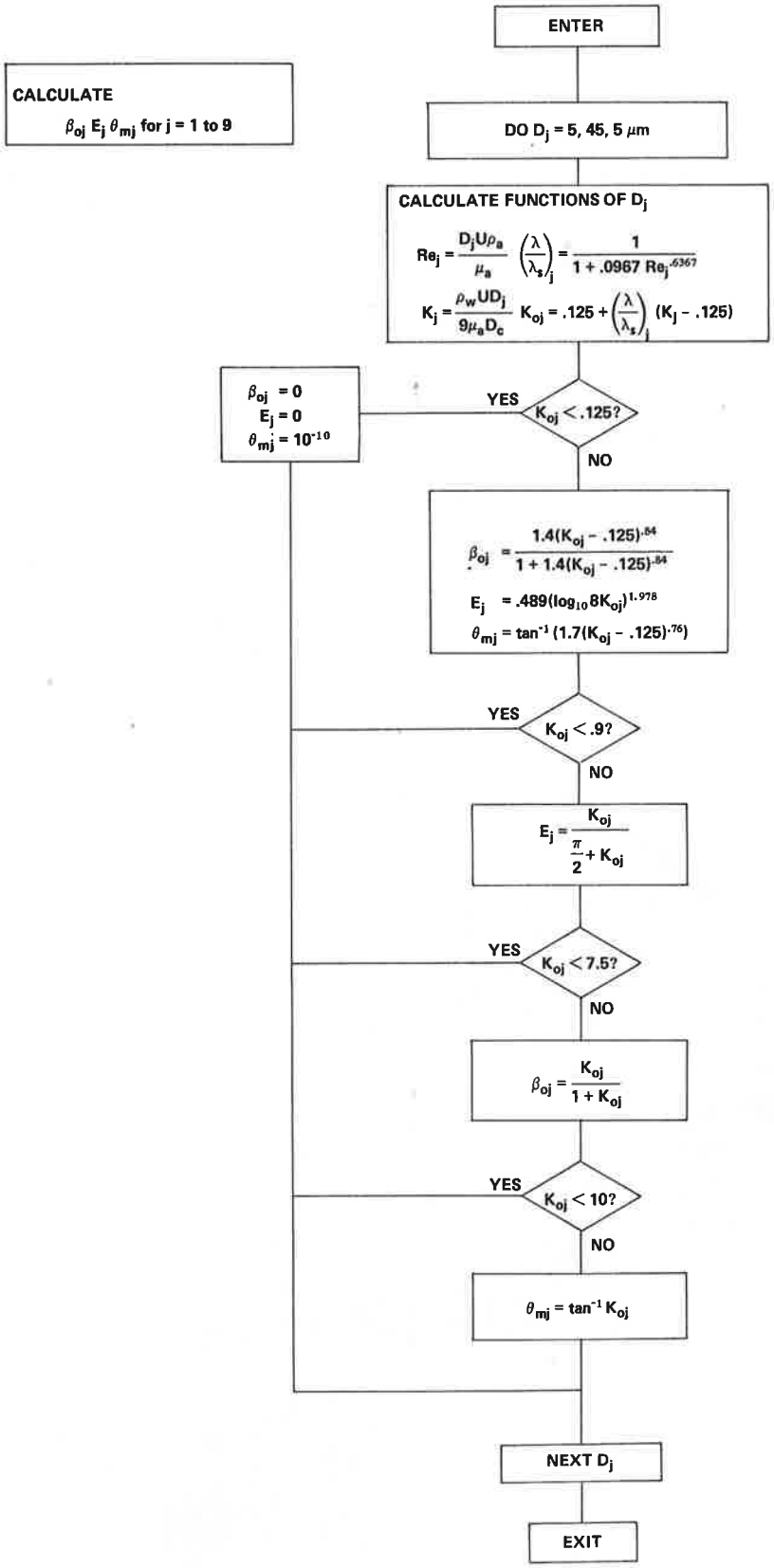

FIG. 3.3: THIS PROGRAM BLOCK CALCULATES THE STAGNATION POINT COLLECTION EFFICIENCY β_{oj}, THE TOTAL COLLECTION EFFICIENCY E_j, AND THE MAXIMUM IMPINGEMENT ANGLE θ_{mj}, FOR EACH DROP SIZE ACCORDING TO THE FORMULAE OF LANGMUIR AND BLODGETT

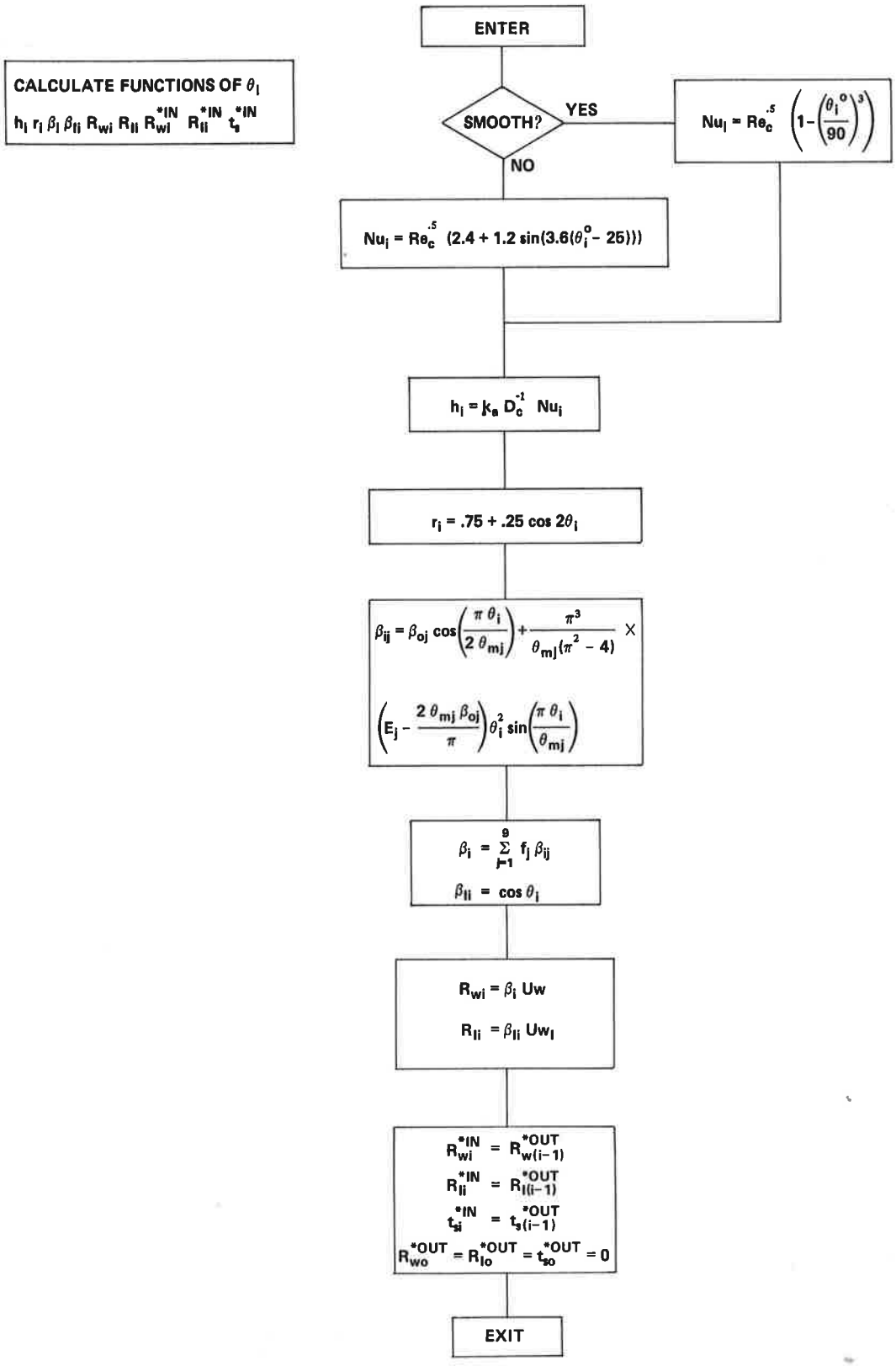

FIG. 3.4: THIS PROGRAM BLOCK CALCULATES INPUT VARIABLES FOR THE HEAT BALANCE EQUATION, WHICH VARY WITH ANGLE AROUND THE CYLINDER

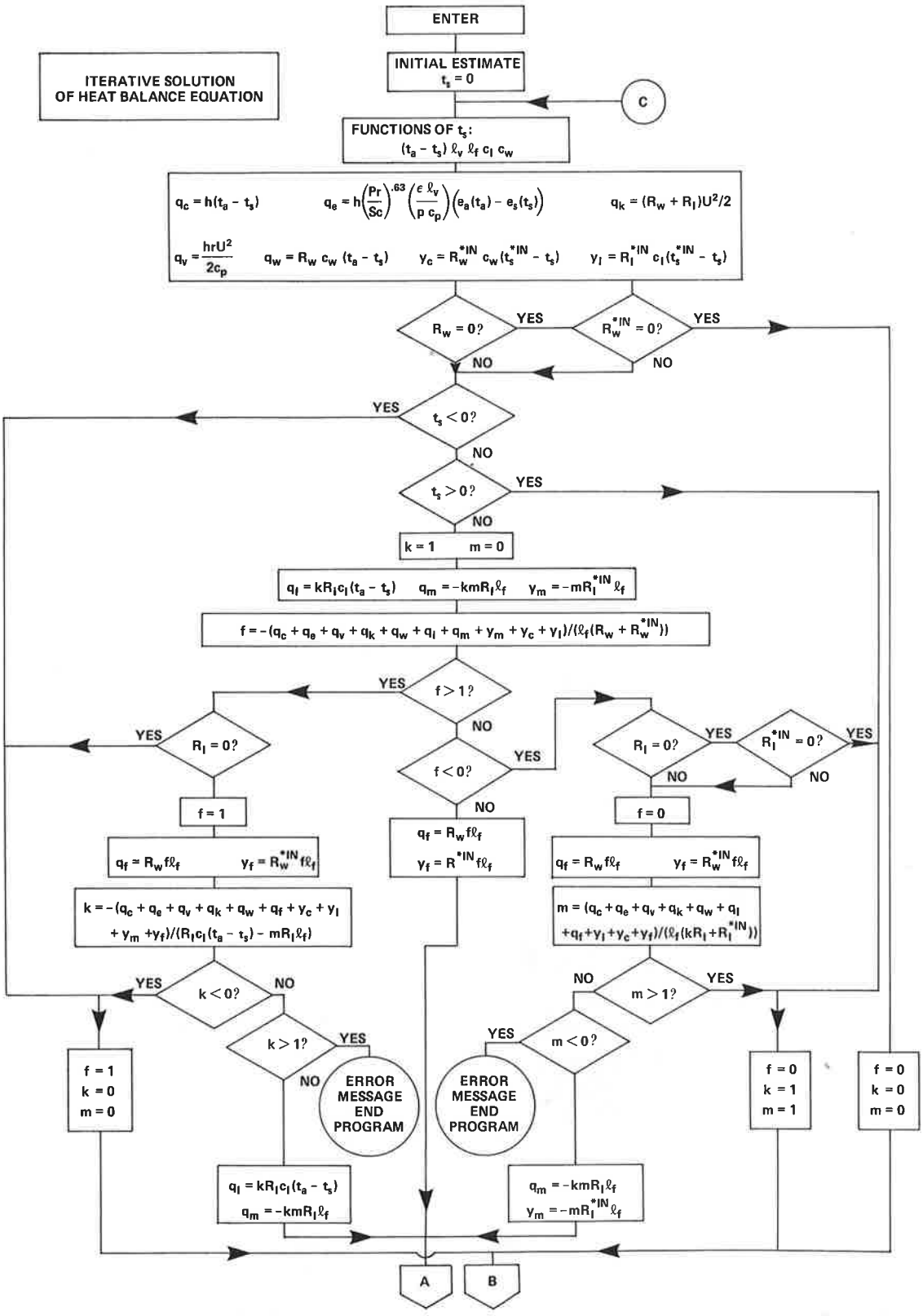

FIG. 3.5(a): THIS PROGRAM BLOCK DETERMINES THE DEPOSIT SURFACE CONDITIONS WHICH SATISFY THE STEADY STATE HEAT BALANCE EQUATION

ITERATIVE SOLUTION OF HEAT BALANCE EQUATION CONTINUED

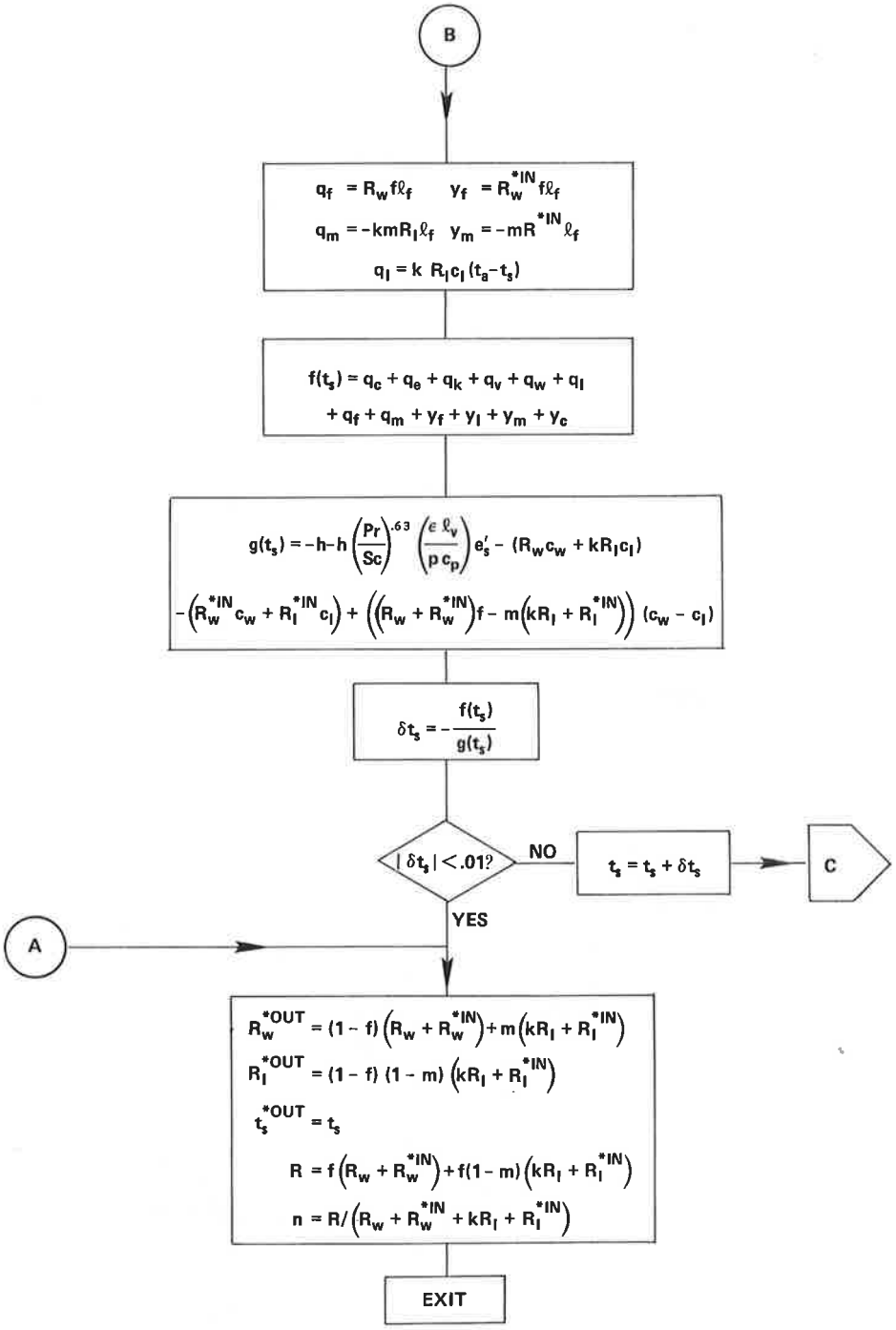

FIG. 3.5(b): CONTINUATION OF FIG. 3.5(a)

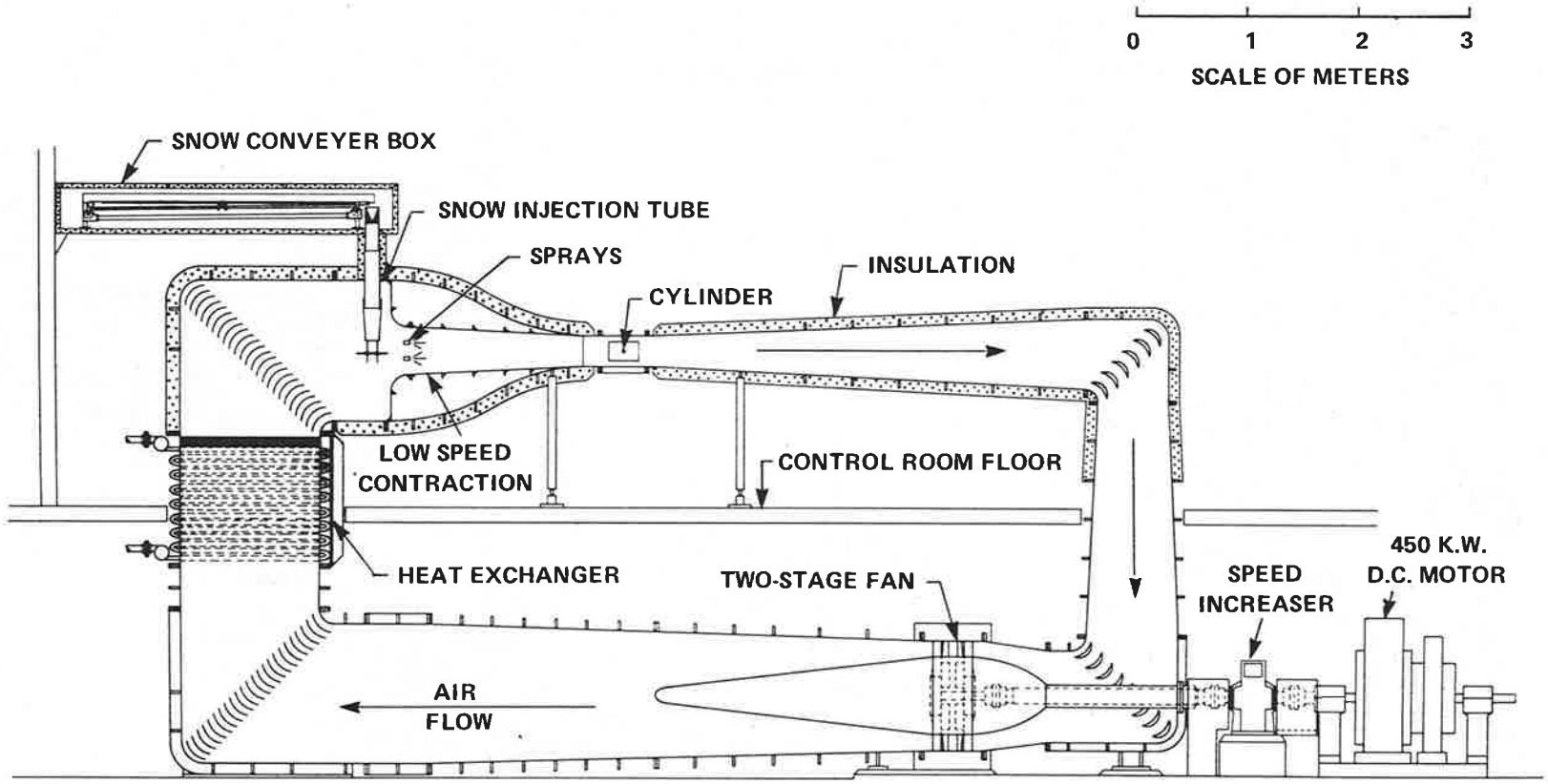

FIG. 4.1: HIGH SPEED ICING WIND TUNNEL

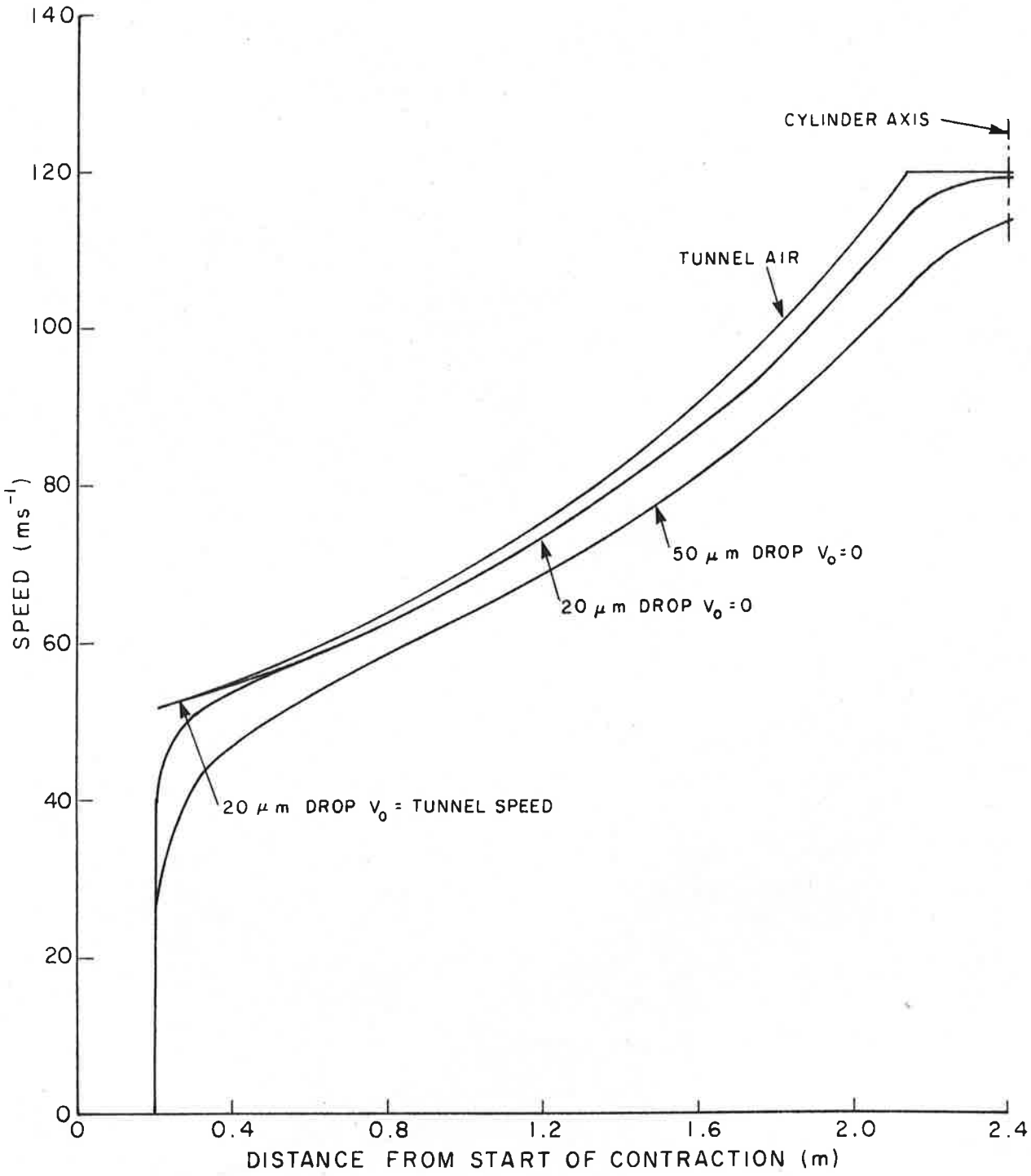

FIG. 4.2: ACCELERATION OF SPRAY DROPLETS THROUGH THE CONTRACTION SECTION OF THE TUNNEL

V_0 IS THE INITIAL INJECTION SPEED OF THE DROPLET

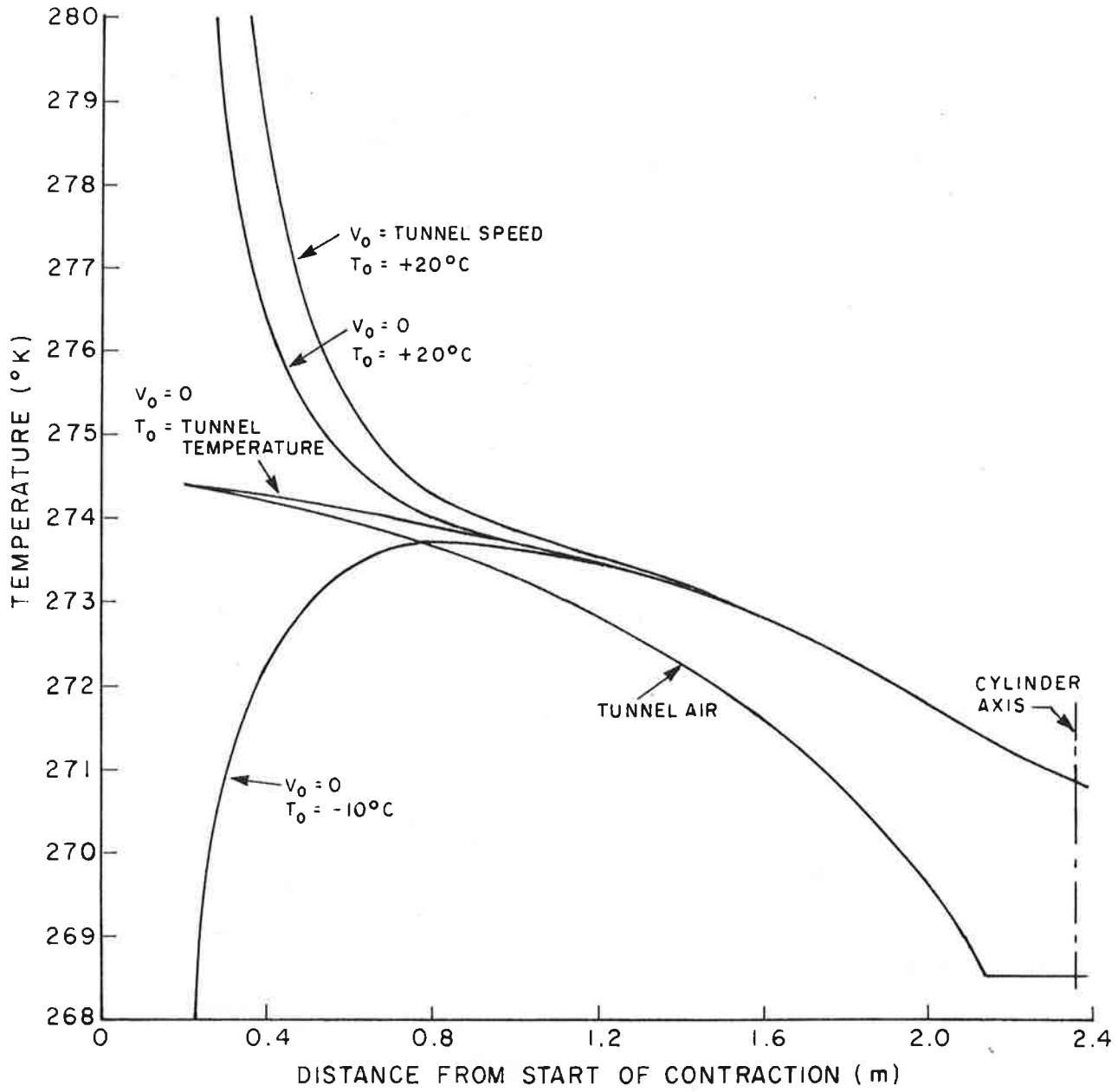

FIG. 4.3: THERMAL ADJUSTMENT OF INDIVIDUAL 20μm DIAMETER SPRAY DROPLETS ACCELERATING THROUGH THE CONTRACTION SECTION OF THE TUNNEL
V_0 AND T_0 ARE THE INITIAL INJECTION VELOCITY AND TEMPERATURE OF THE DROPLET

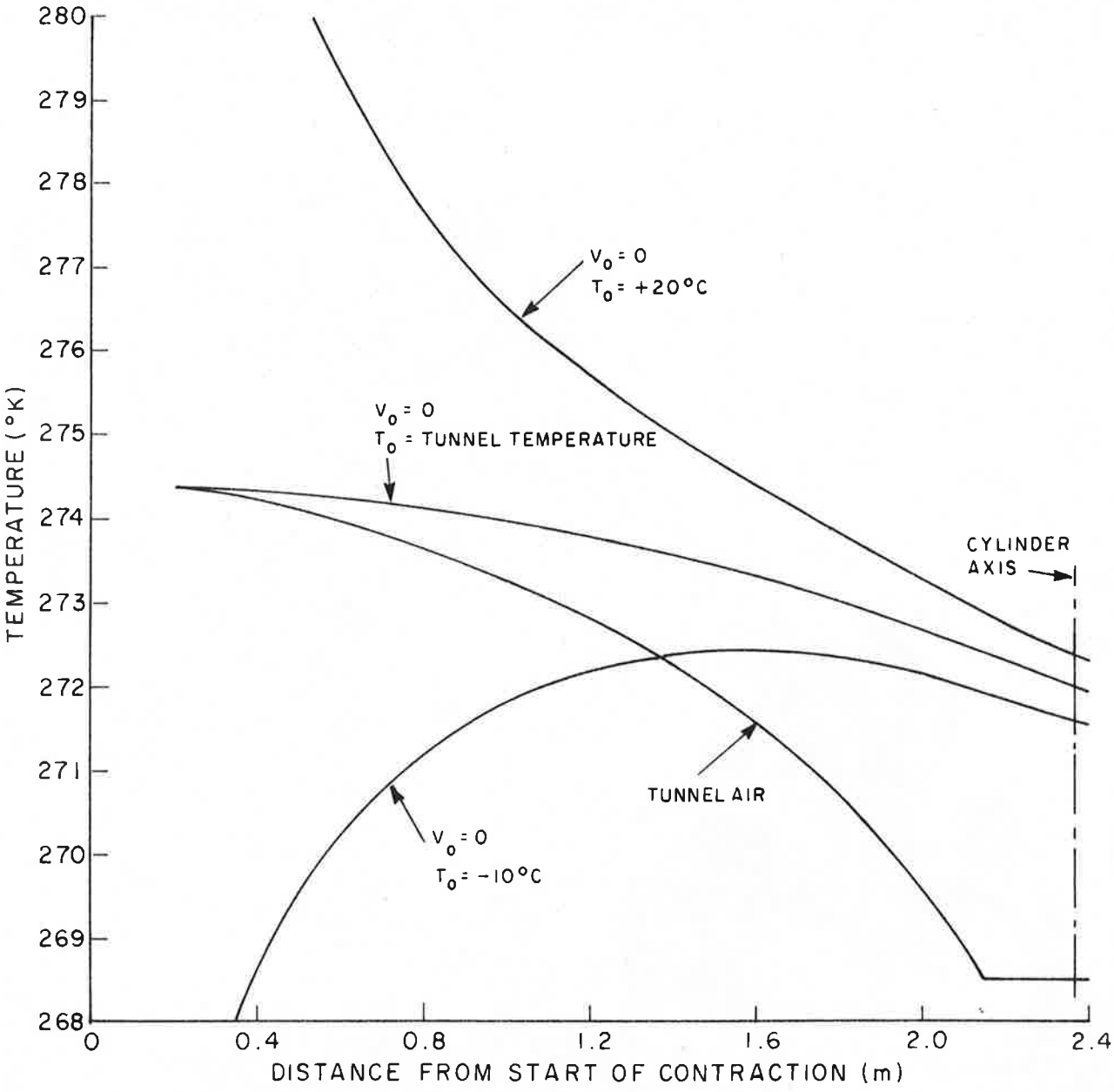

FIG. 4.4: THERMAL ADJUSTMENT OF INDIVIDUAL 50μm DIAMETER SPRAY DROPLETS ACCELERATING THROUGH THE CONTRACTION SECTION OF THE TUNNEL

V_0 AND T_0 ARE THE INITIAL INJECTION VELOCITY AND TEMPERATURE OF THE DROPLET

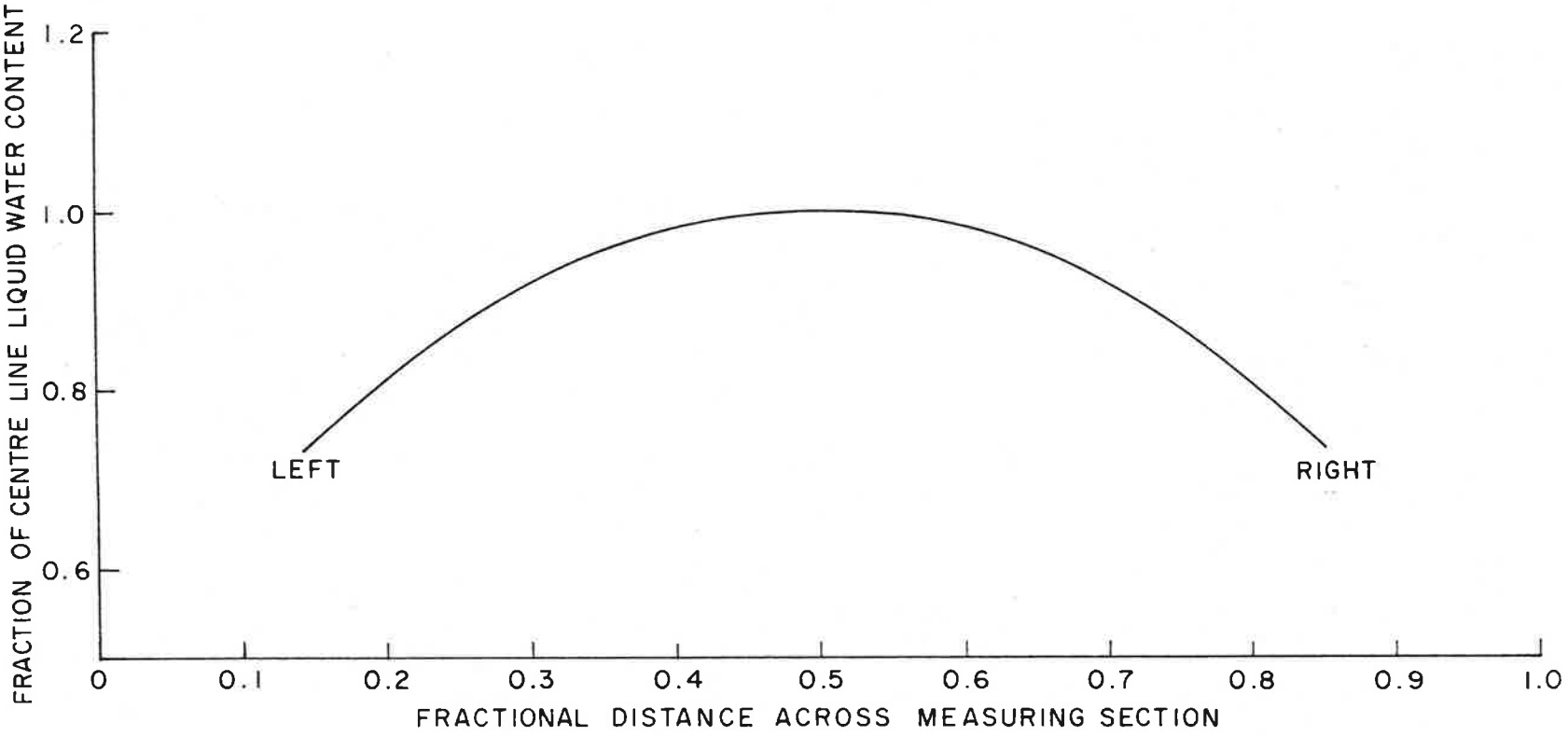

FIG. 4.5: LIQUID WATER CONTENT PROFILE ACROSS THE MEASURING SECTION UNDER THE FOLLOWING CONDITIONS:
AIRSPEED 30.5 ms^{-1}, AIR TEMPERATURE $-15^{\circ}C$, CENTERLINE LIQUID WATER CONTENT 1.23 gm^{-3}

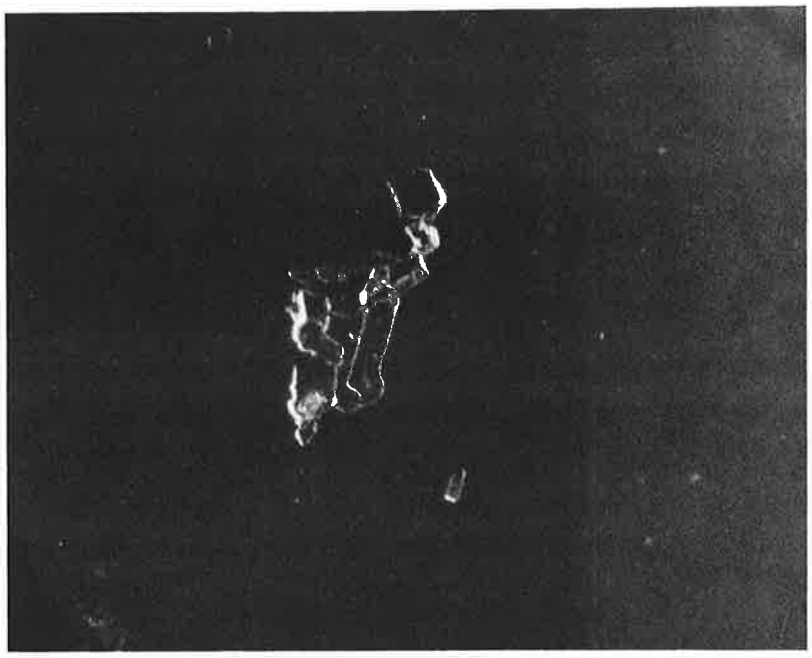

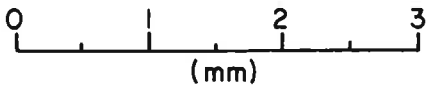

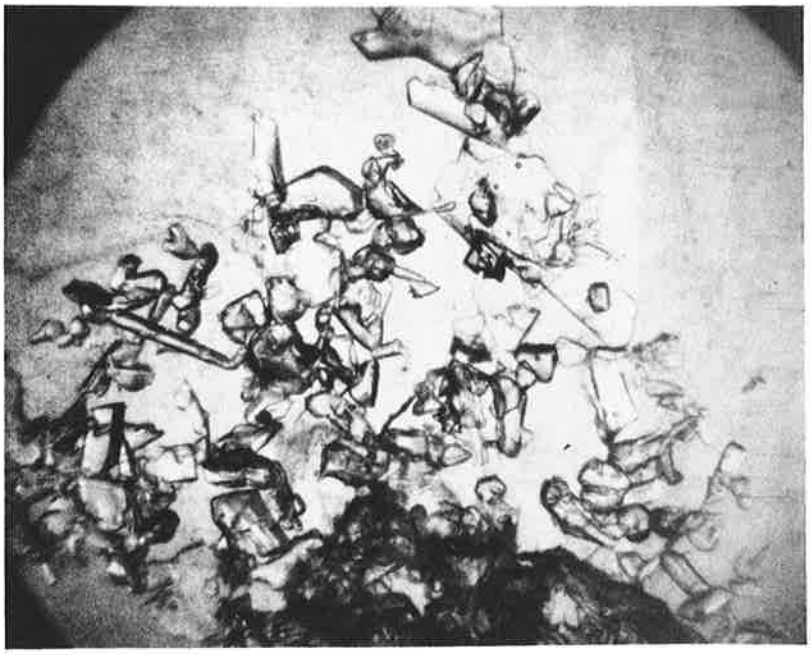

FIG. 4.6: TUNNEL ICE CRYSTAL SAMPLES TAKEN IN THE MEASURING SECTION

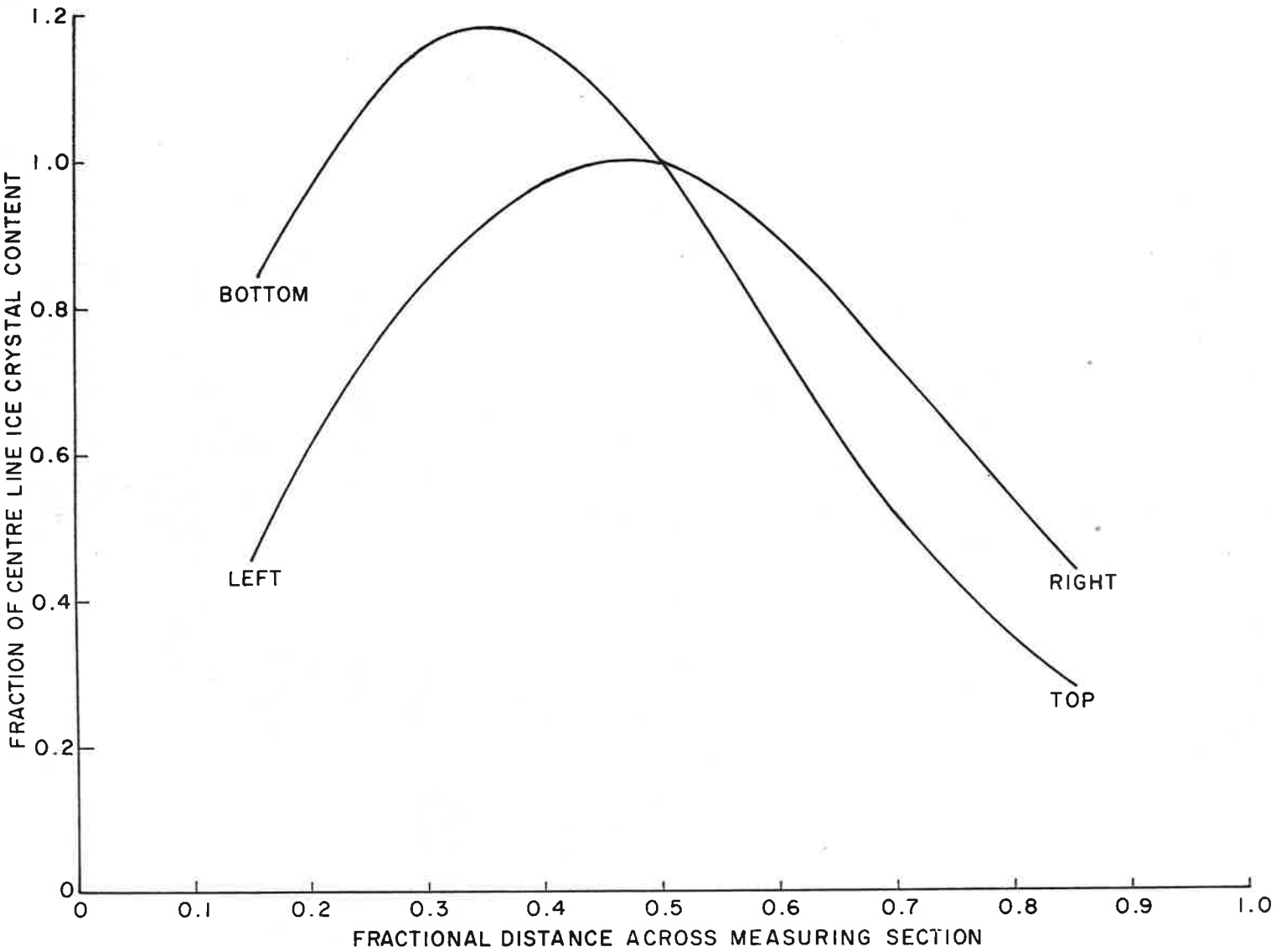

FIG. 4.7: ICE CRYSTAL CONTENT PROFILE HORIZONTALLY AND VERTICALLY ACROSS THE MEASURING SECTION UNDER THE FOLLOWING CONDITIONS:
AIRSPEED 30.5 ms^{-1}; AIR TEMPERATURE −15°C; CENTERLINE ICE PARTICLE CONTENT 0.4 gm^{-3}

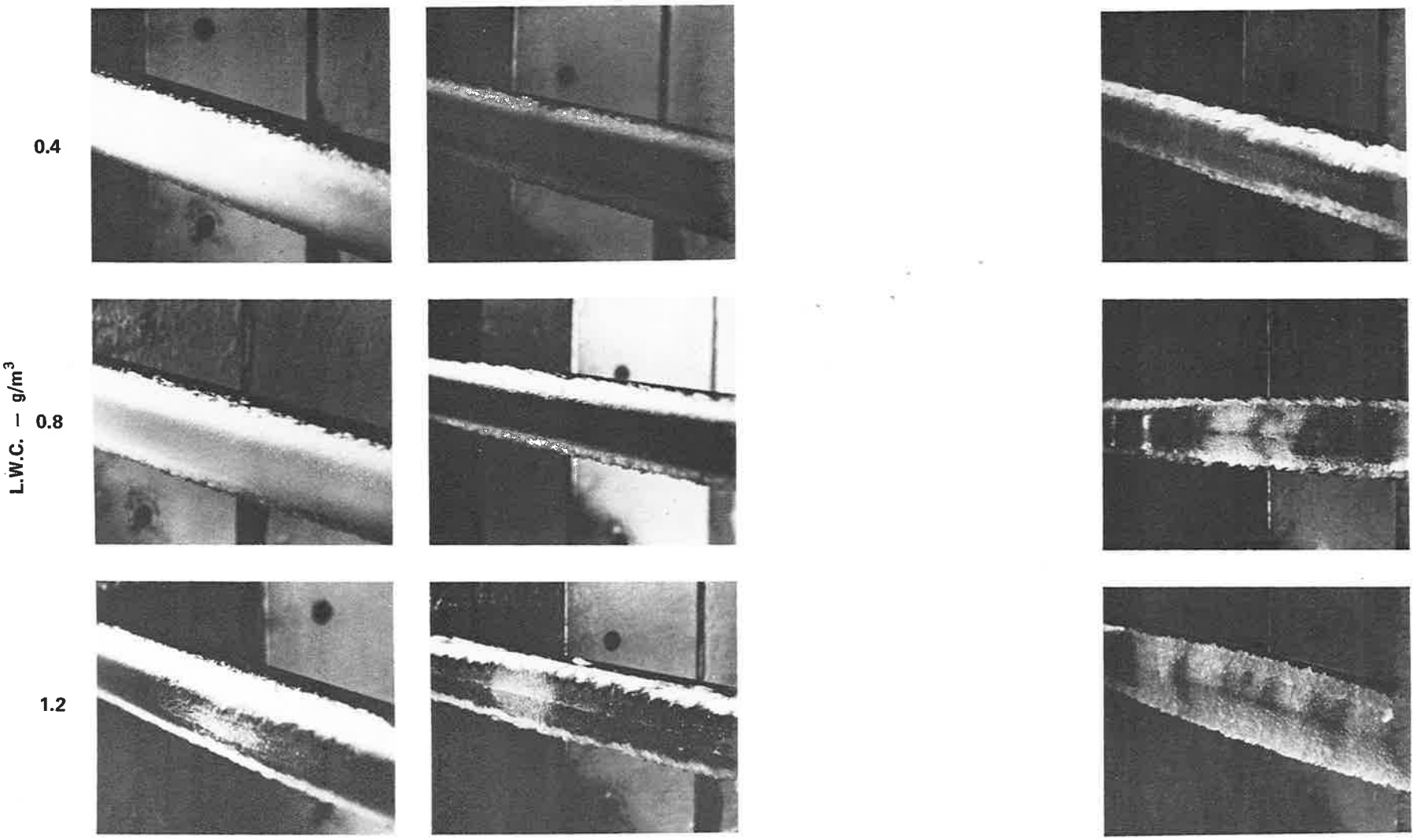

FIG. 6.1(a): CYLINDER ICING AT –15°C WITH LIQUID WATER ONLY

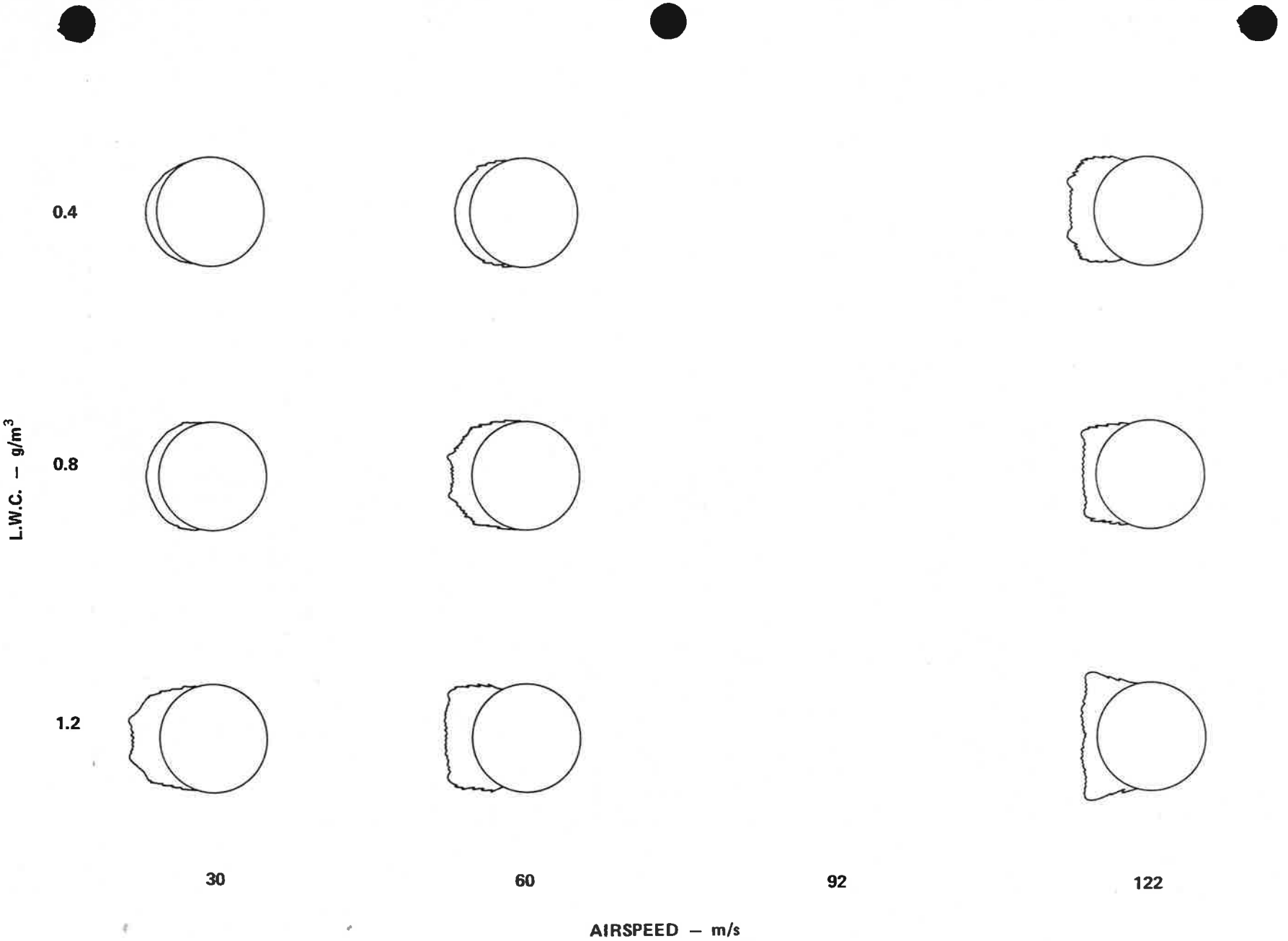

FIG. 6.1(b): CYLINDER ICING PROFILES AT -15°C WITH LIQUID WATER ONLY

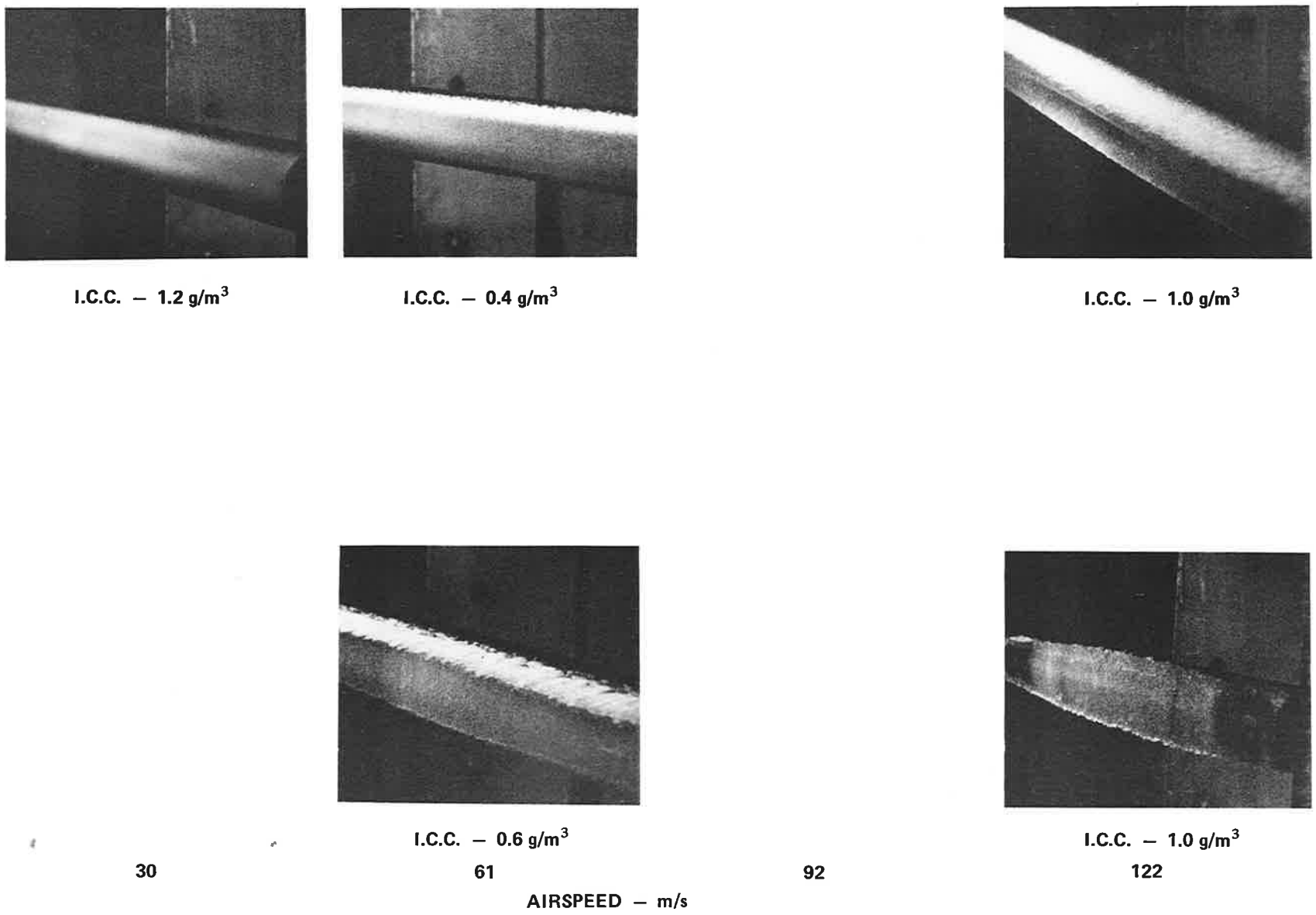

FIG. 6.2(a): CYLINDER ICING AT -15°C WITH LIQUID WATER AND ICE CRYSTALS

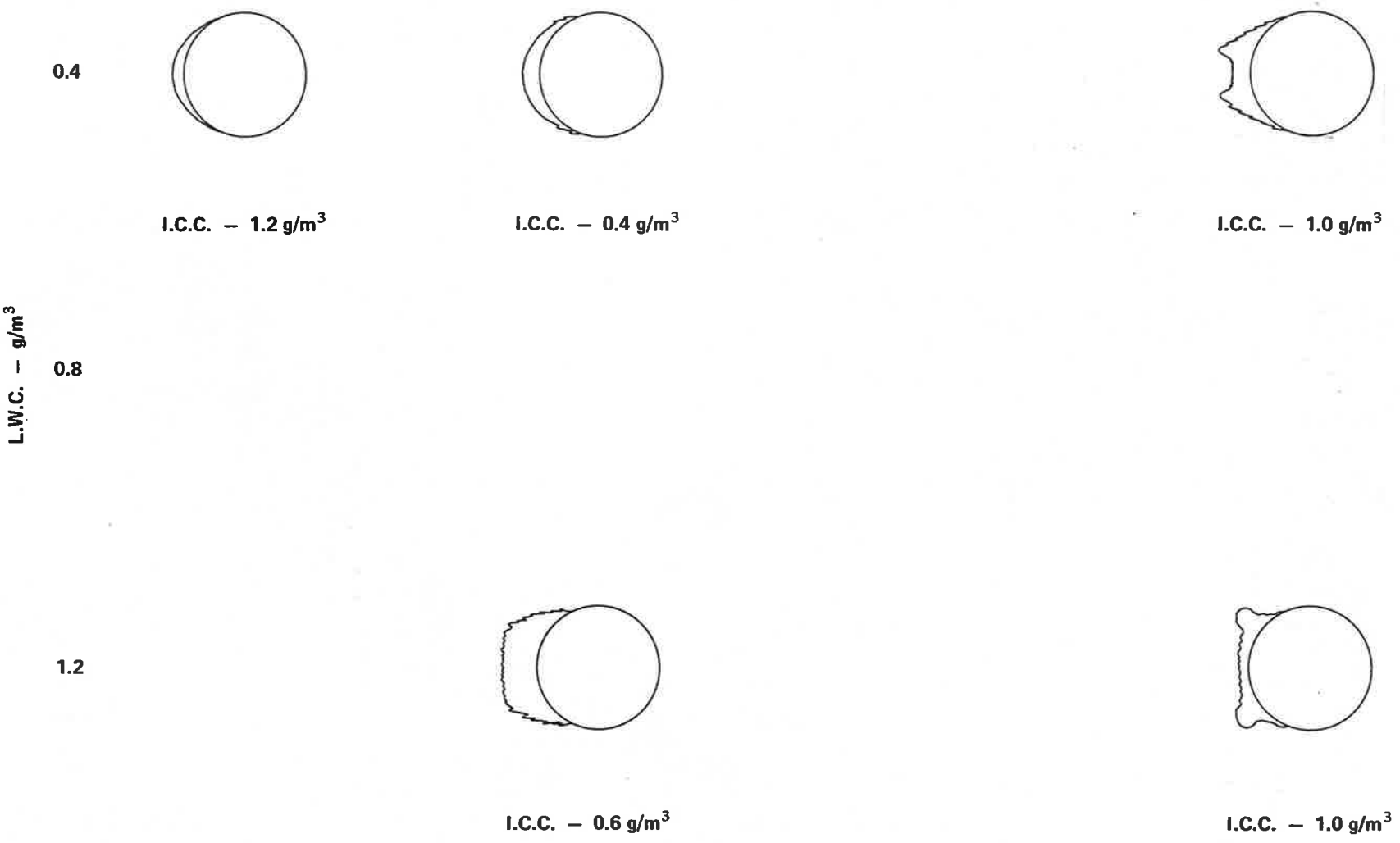

FIG. 6.2(b): CYLINDER ICING PROFILES AT – 15°C WITH LIQUID WATER AND ICE CRYSTALS

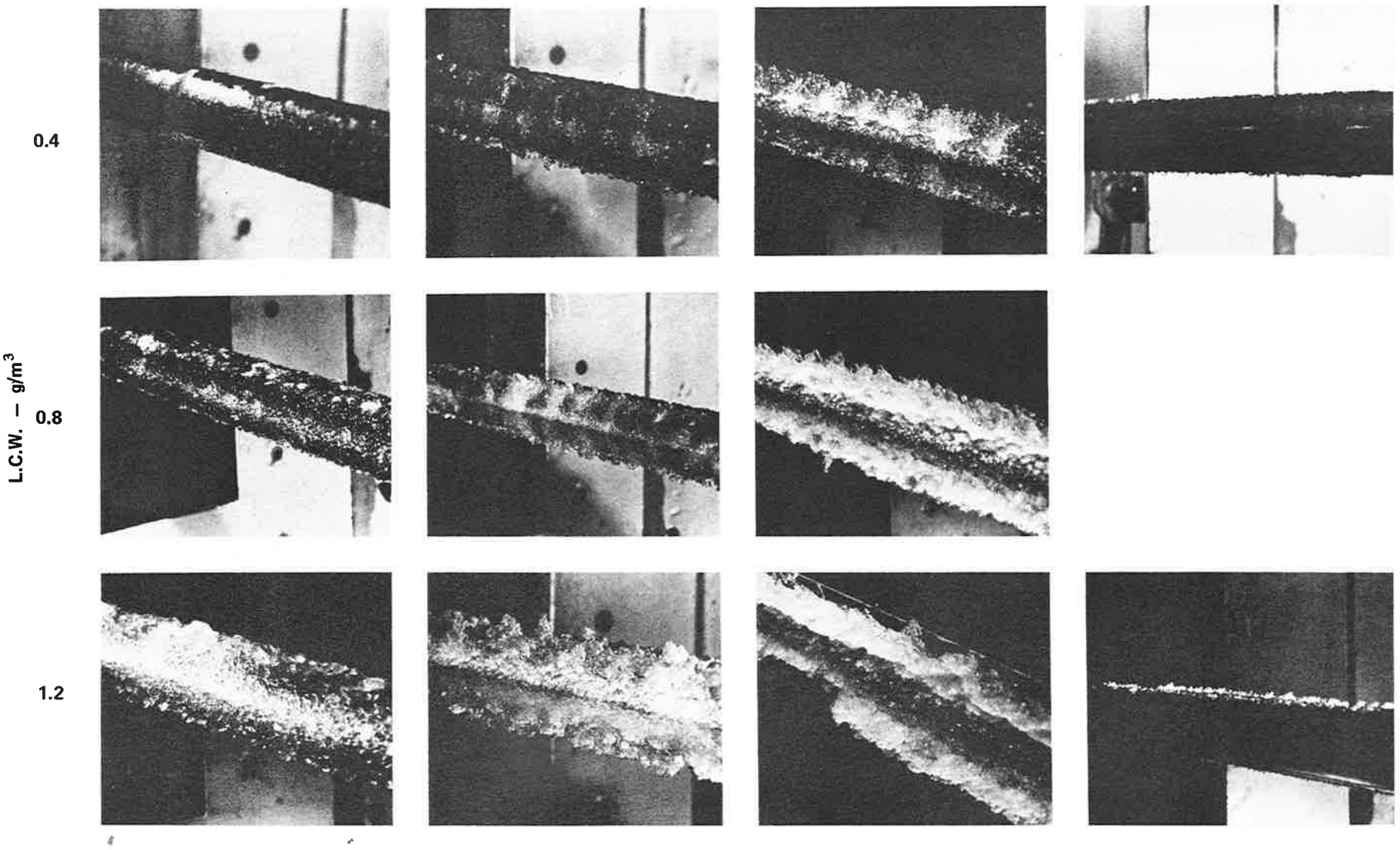

FIG. 6.3(a): CYLINDER ICING AT –5°C WITH LIQUID WATER ONLY

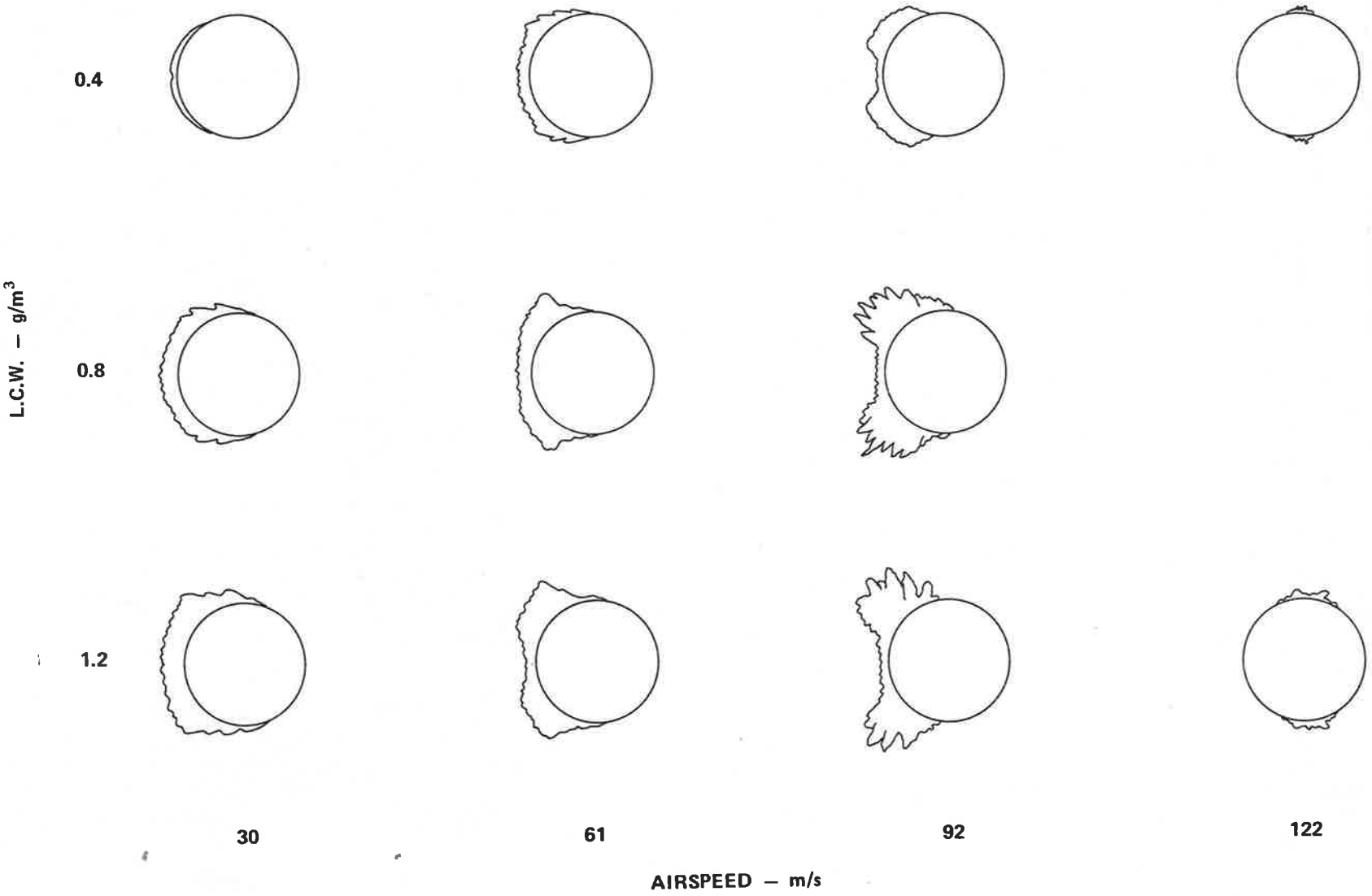

FIG. 6.3(b): CYLINDER ICING PROFILES AT -5°C WITH LIQUID WATER ONLY

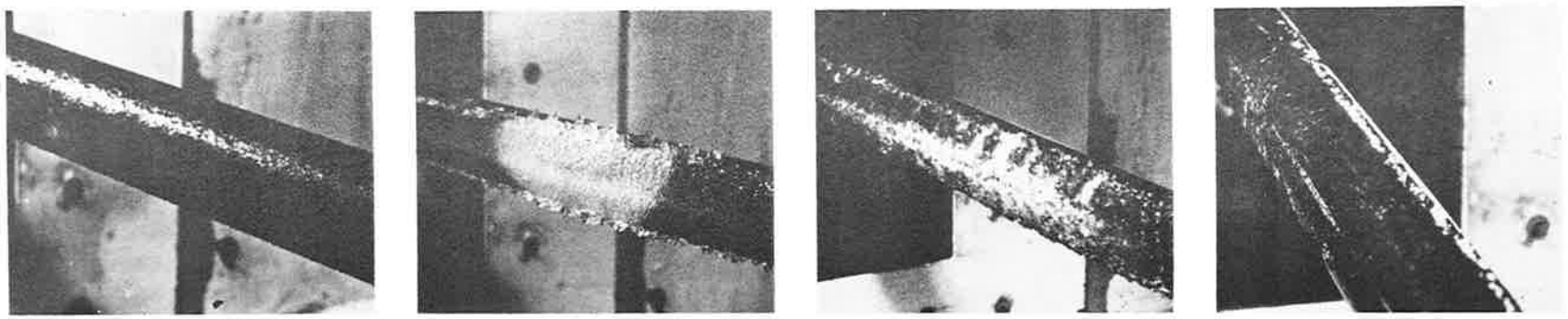

I.C.C. – 1.0 g/m^3 I.C.C. – 0.3 g/m^3 I.C.C. – 0.1 g/m^3 I.C.C. – 1.3 g/m^3

L.W.C. – g/m^3

0.4

0.8

1.2

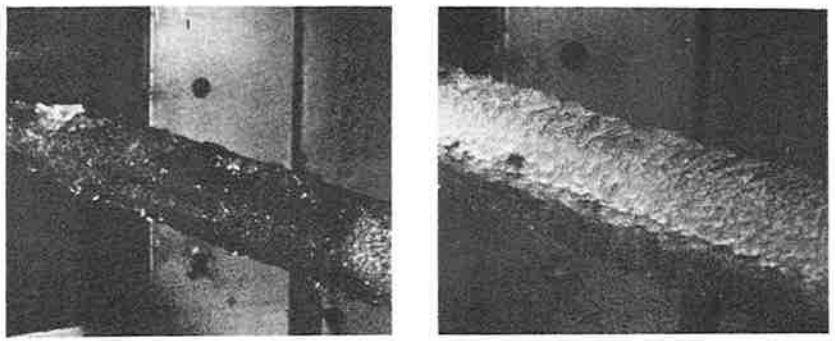

I.C.C. – 1.2 g/m^3 I.C.C. – 0.6 g/m^3

92 122

AIRSPEED – m/s

FIG. 6.4(a): CYLINDER ICING AT -5°C WITH LIQUID WATER AND ICE CRYSTALS

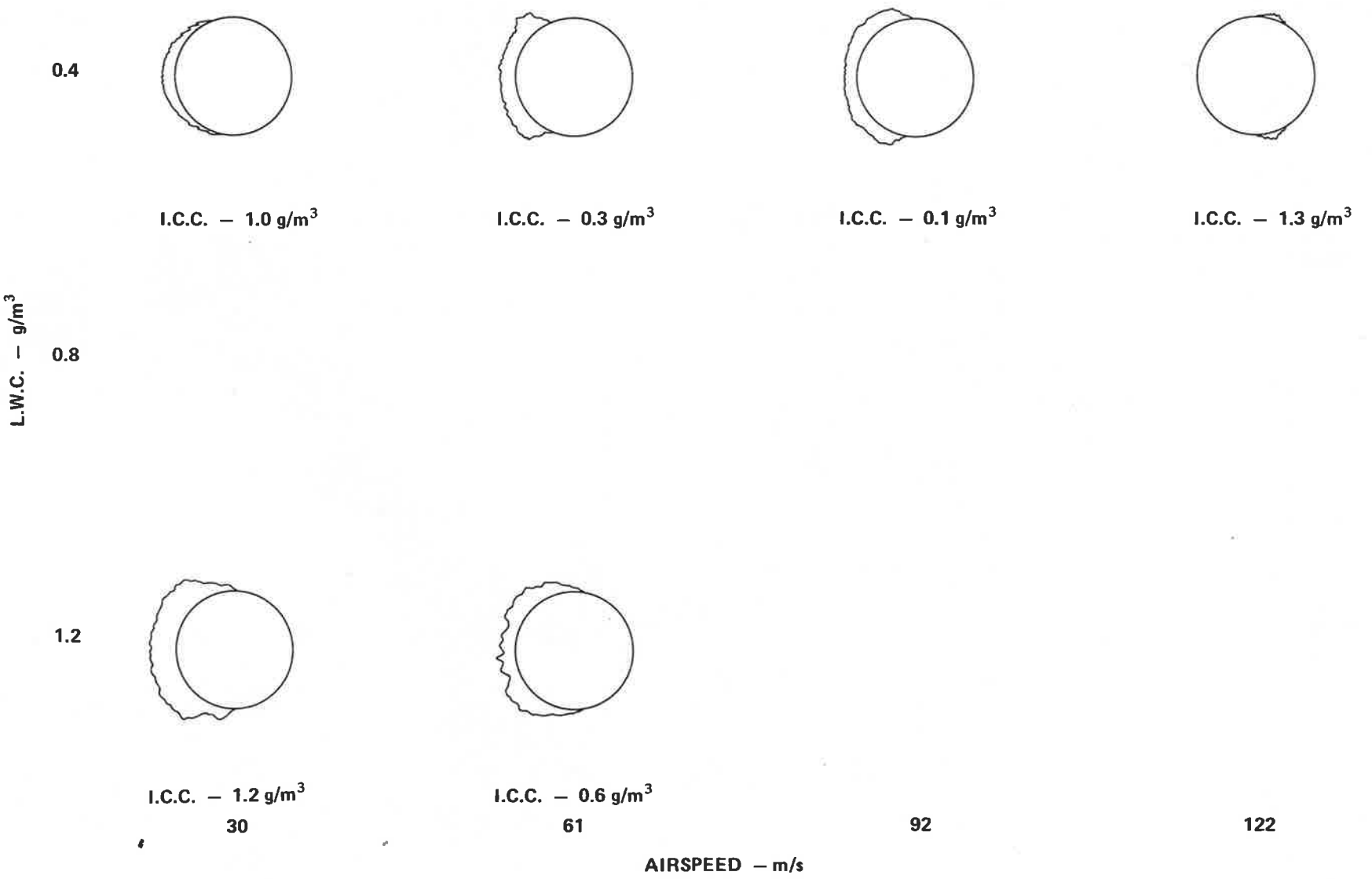

FIG. 6.4(b): CYLINDER ICING PROFILES AT -5°C WITH LIQUID WATER AND ICE CRYSTALS

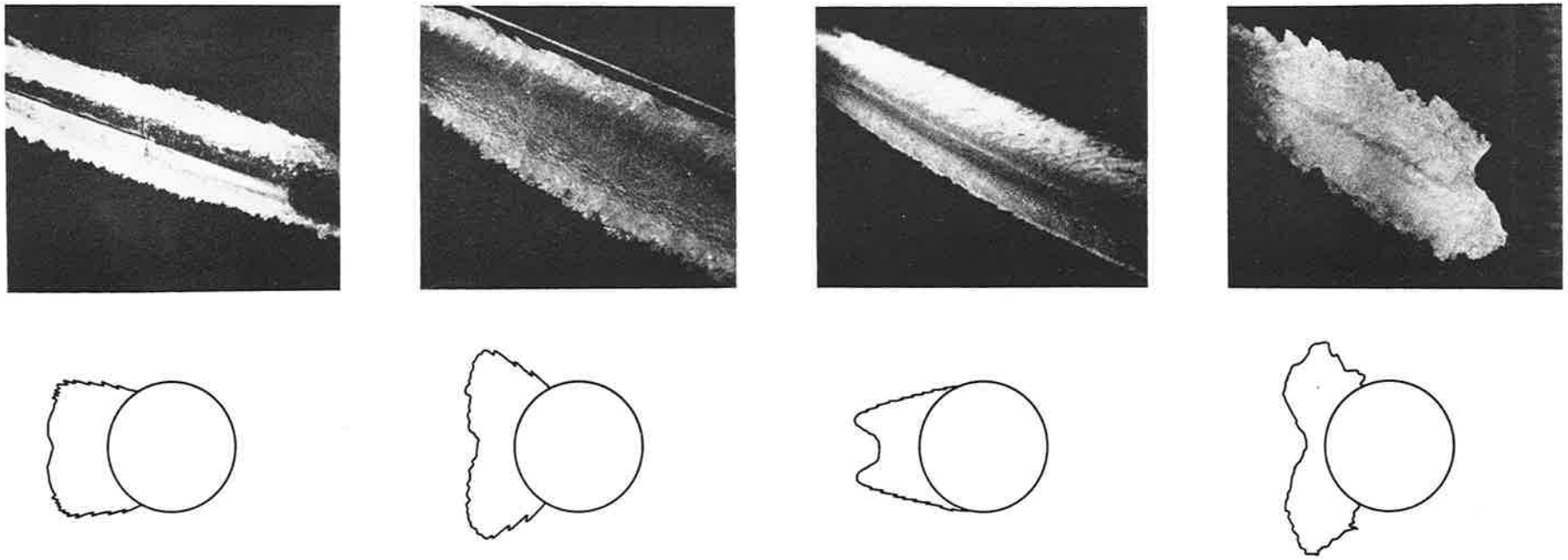

L.W.C. – 0.13 g/m^3
LIQUID WATER ONLY

L.W.C. – 0.28 g/m^3
LIQUID WATER ONLY

L.W.C. – 0.28 g/m^3
I.C.C. – 0.8 g/m^3
LIQUID WATER AND ICE CRYSTALS

L.W.C. – 0.65 g/m^3
LIQUID WATER ONLY

FIG. 6.5: CYLINDER ICING AND PROFILES AT -8°C AND 110 M/S

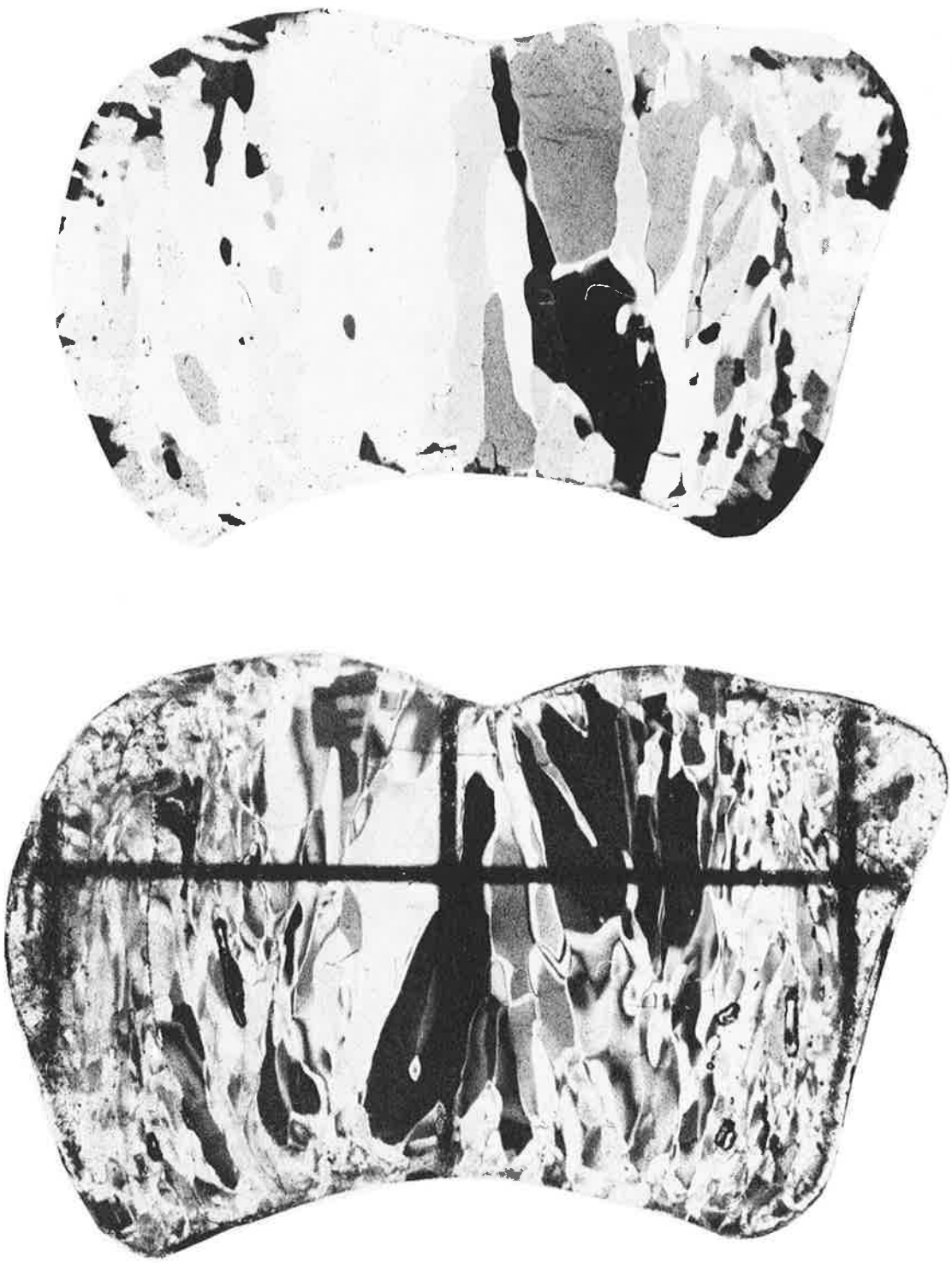

FIG. 6.6: THIN SECTIONS BETWEEN CROSSED POLAROIDS OF ACCRETION 59C
(−8°C, 110 m/s, LWC 0.13 g/m^3)
THE UPPER SECTION HAS BEEN MICROTOMED THINNER THAN THE LOWER ONE. THE GRID IN THE LOWER SECTION HAS A 1 CM. INTERVAL. A CHIP IS MISSING FROM THE UPPER LEFT-HAND CORNER.

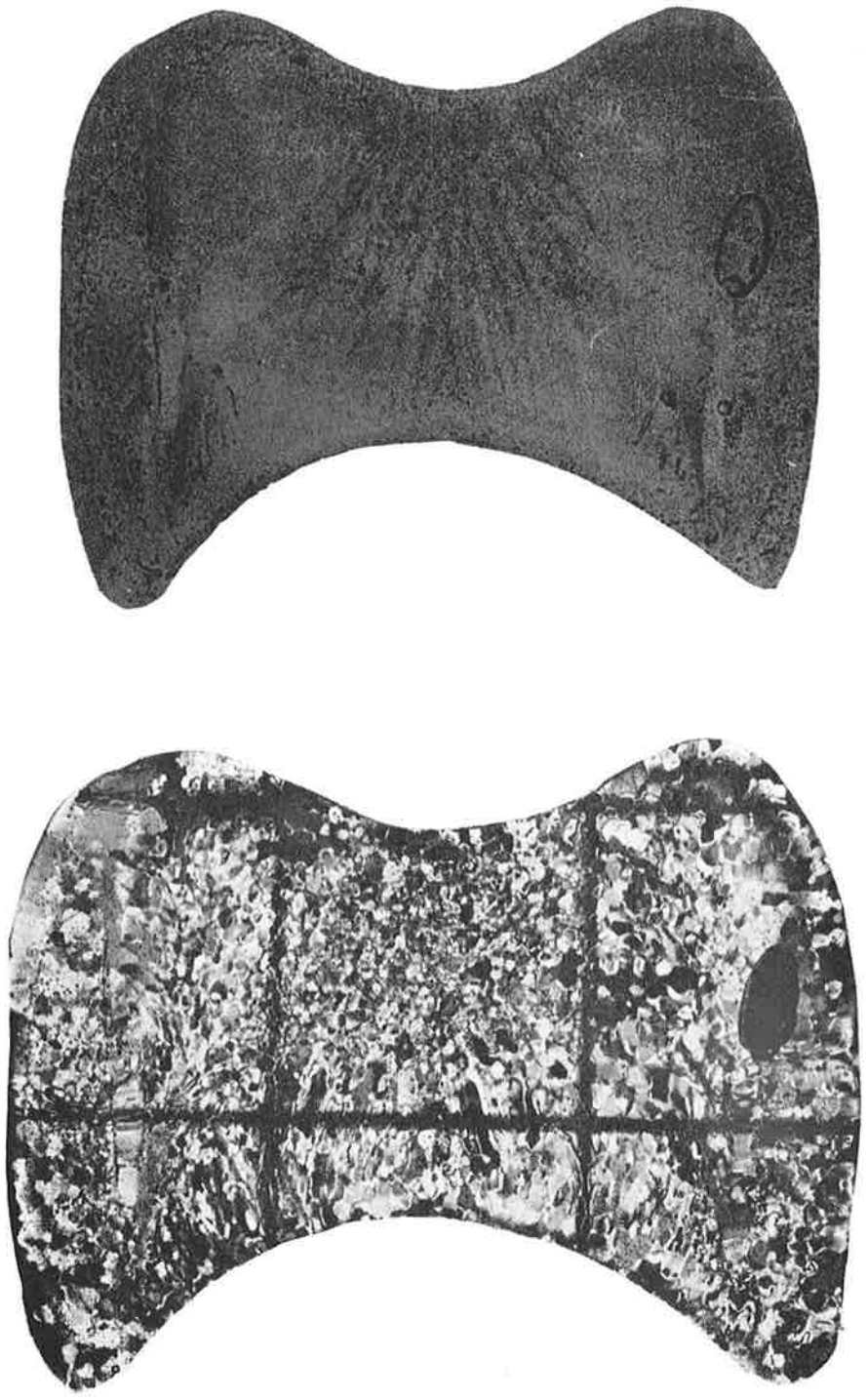

FIG. 6.7: THIN SECTIONS IN TRANSMITTED LIGHT (ABOVE) AND BETWEEN CROSSED POLAROIDS (BELOW) OF ACCRETION 72C (−15°C, 122 m/s, LWC 0.44 g/m^3).
THE GRID IN THE LOWER SECTION HAS A 1 CM. INTERVAL.

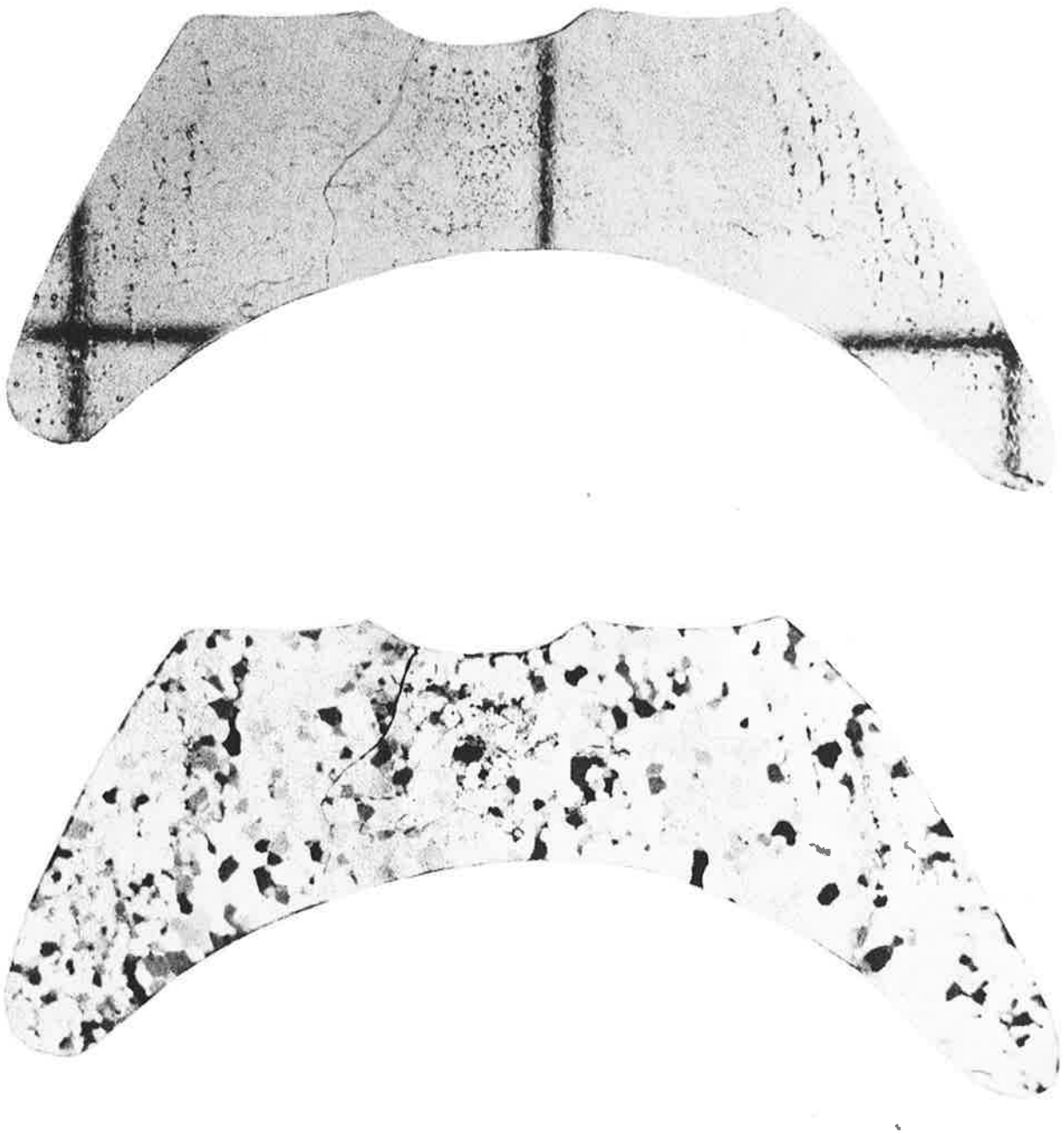

FIG. 6.8: THIN SECTIONS IN TRANSMITTED LIGHT (ABOVE) AND BETWEEN CROSSED POLAROIDS (BELOW) OF ACCRETION 70CM (−15°C, 122 m/s, LWC 0.44 g/m^3, 1CC 0.7 g/m^3). THE GRID IN THE UPPER SECTION HAS A 1 CM. INTERVAL. THE TWO HORNS WERE BROKEN OFF DURING MICROTOMING.

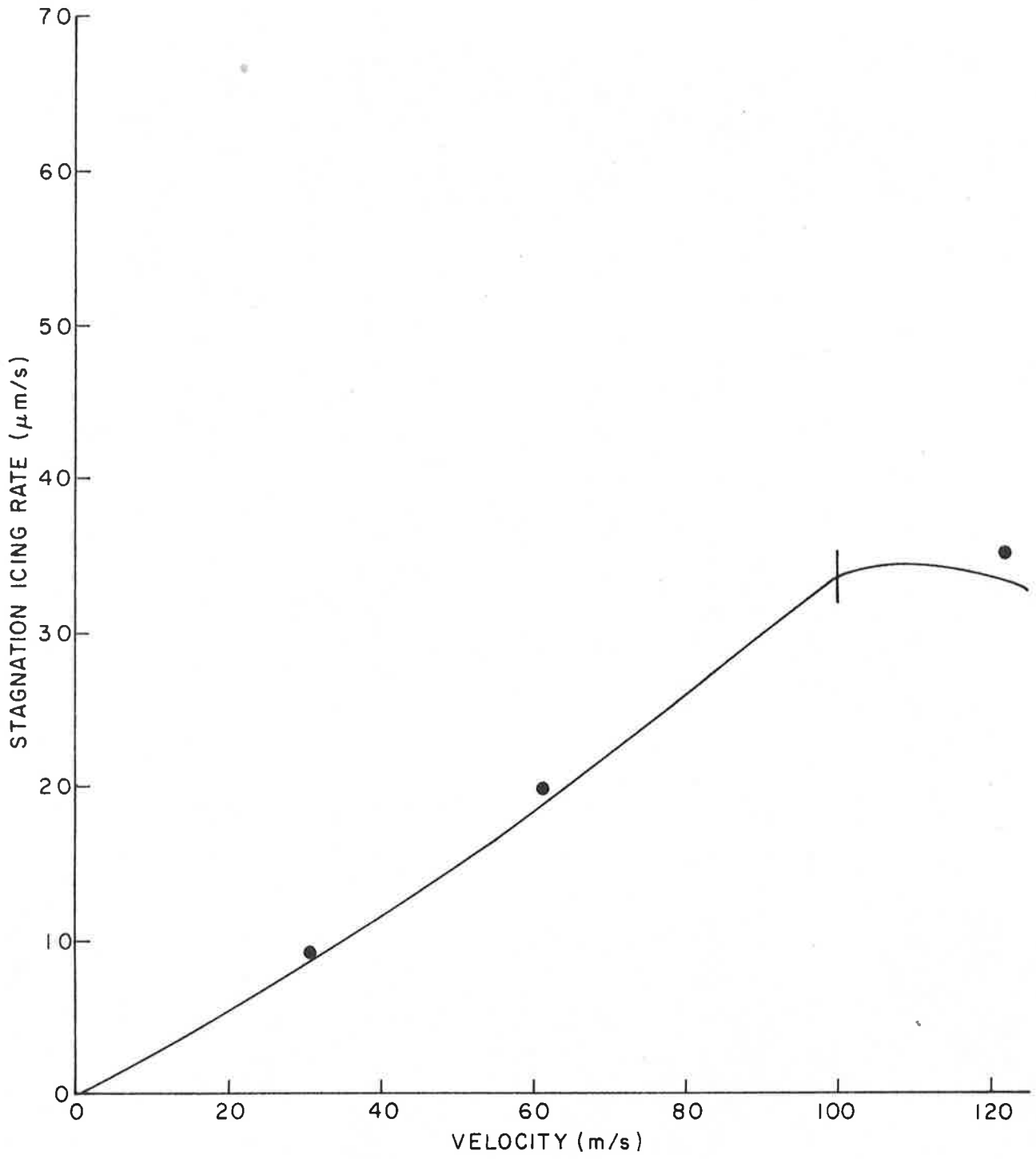

FIG. 7.1: STAGNATION LINE ICING RATE AT -15°C AND LWC OF 0.4 G/M^3.
THE POINTS ARE EXPERIMENTAL VALUES. THE LINE IS THE ICING MODEL PREDICTION. THE TICK IN THE LINE SEPARATES WET (TO RIGHT) FROM DRY (TO LEFT) GROWTH.

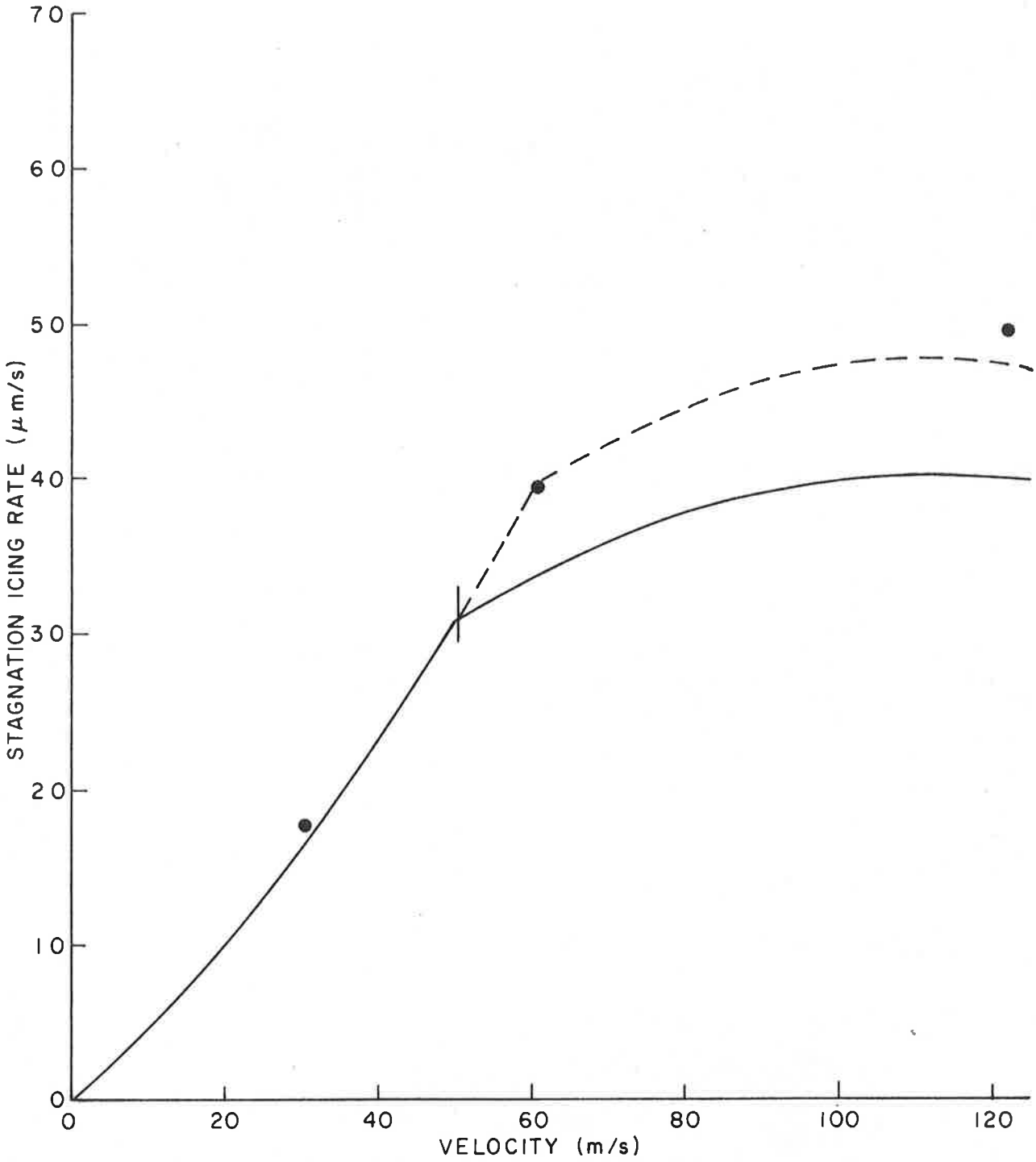

FIG. 7.2: STAGNATION LINE ICING RATE AT -15°C AND LWC OF 0.8 G/M^3
THE POINTS ARE EXPERIMENTAL VALUES. THE SOLID LINE IS THE ICING MODEL PREDICTION ASSUMING ALL UNFROZEN WATER RUNS BACK. THE TICK IN THE LINE SEPARATES WET (TO RIGHT) FROM DRY (TO LEFT) GROWTH. THE DASHED CURVE ASSUMES ADDITIONAL WATER INCORPORATED INTO THE DEPOSIT IN AMOUNTS UP TO 15% OF THE TOTAL DEPOSIT MASS.

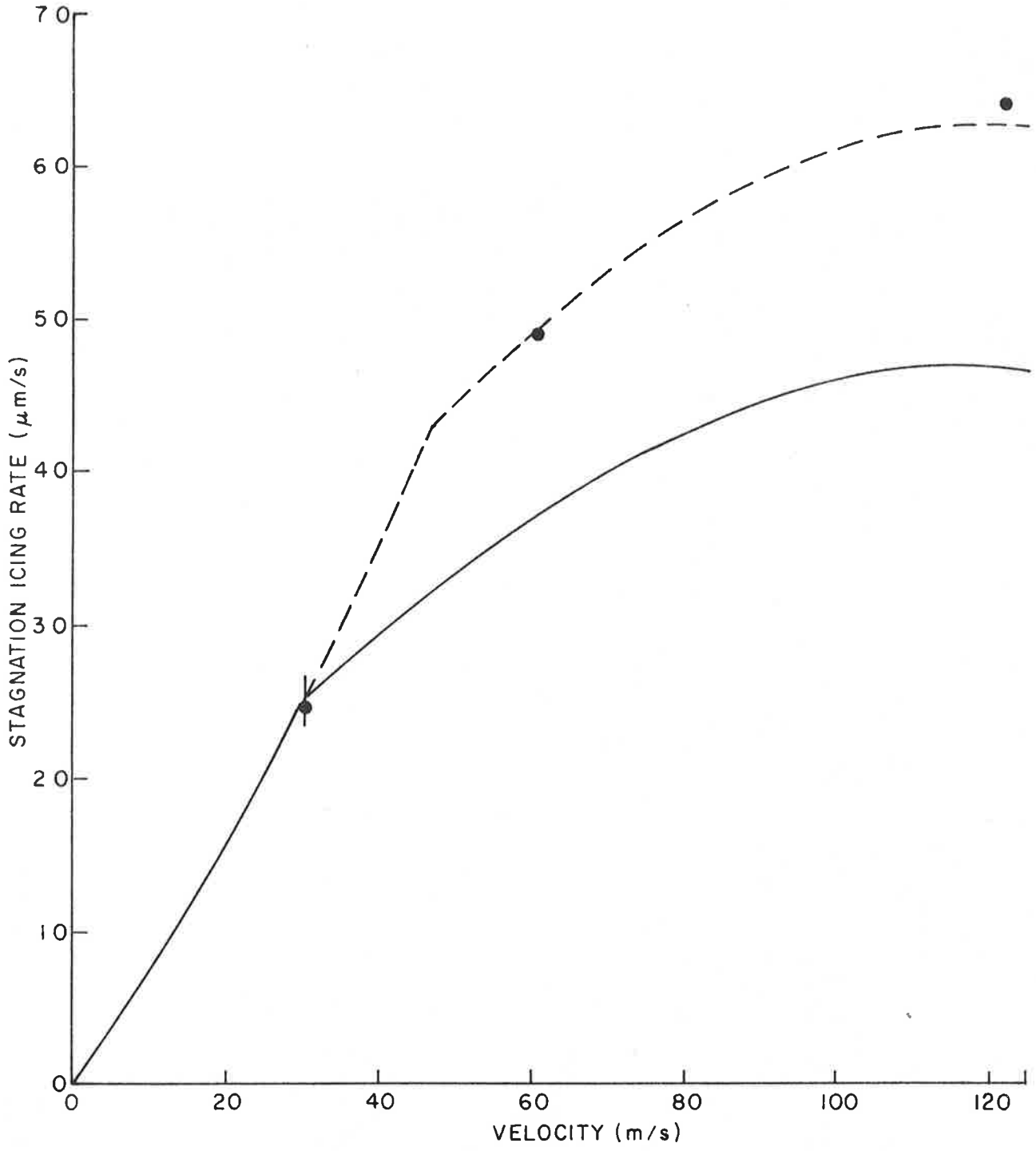

FIG 7.3: STAGNATION LINE ICING RATE AT -15°C AND LWC OF 1.2 G/M^3
THE POINTS ARE EXPERIMENTAL VALUES. THE SOLID LINE IS THE ICING MODEL PREDICTION ASSUMING ALL UNFROZEN WATER RUNS BACK. THE TICK IN THE LINE SEPARATES WET (TO RIGHT) FROM DRY (TO LEFT) GROWTH. THE DASHED CURVE ASSUMES ADDITIONAL WATER INCORPORATED INTO THE DEPOSIT IN AMOUNTS UP TO 25% OF THE TOTAL DEPOSIT MASS.

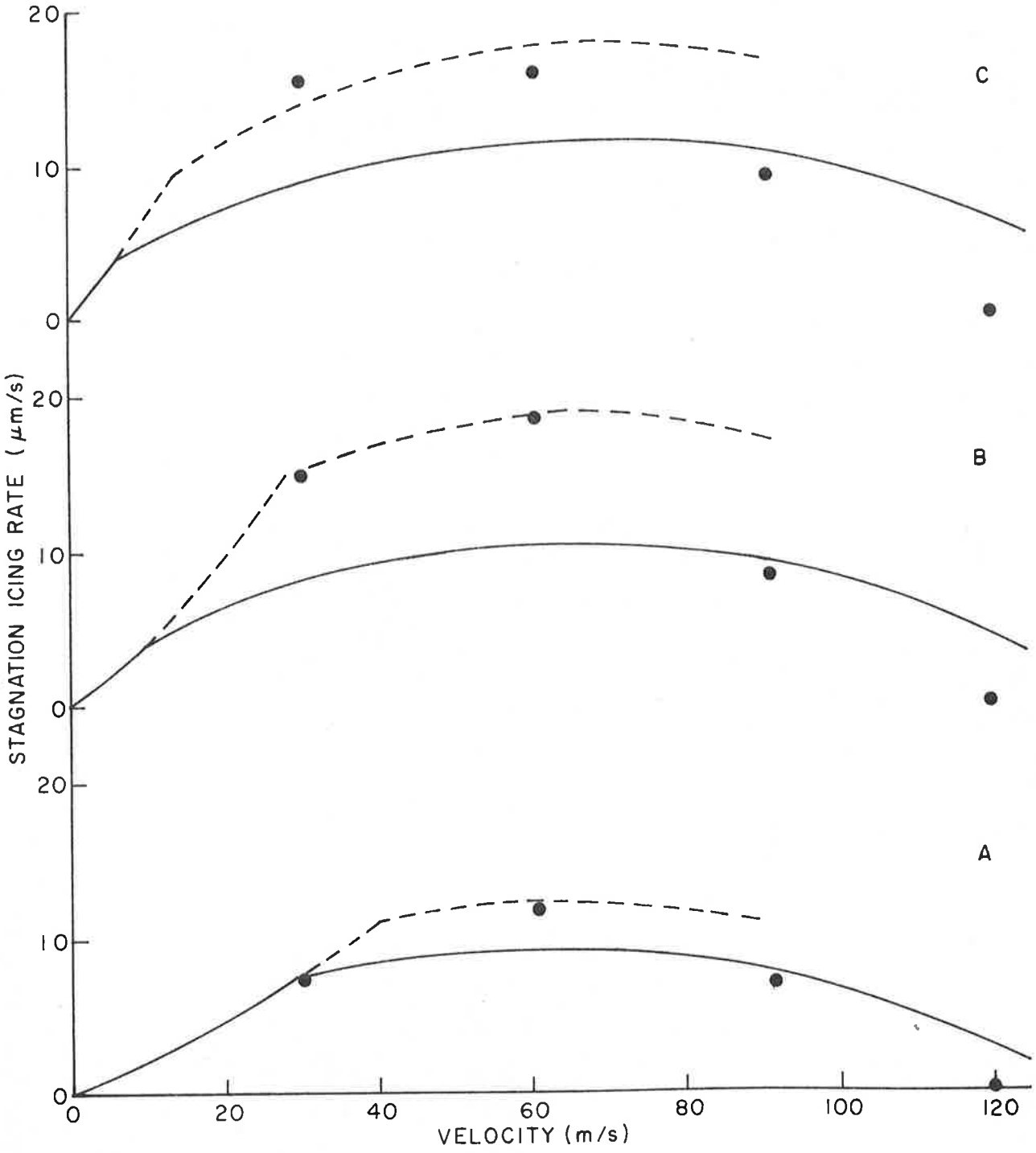

FIG. 7.4: STAGNATION LINE ICING RATE AT -5°C AND LWC OF(A) 0.4 G/M^3 (B) 0.8 G/M^3 AND (C) 1.2 G/M^3.

THE SOLID LINES ARE THE ICING MODEL PREDICTION ASSUMING ALL UNFROZEN WATER RUNS BACK. THE TICKS IN THE LINES SEPARATE WET (TO RIGHT) FROM DRY (TO LEFT) GROWTH. THE DASHED CURVES ASSUME ADDITIONAL WATER INCORPORATED INTO THE DEPOSIT IN AMOUNTS UP TO (A) 25% (B) 45% AND (C) 35% OF THE TOTAL DEPOSIT MASS.

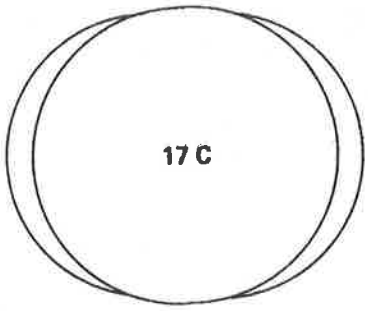

VELOCITY 30.5 m/s
L.W.C. 0.40 g/m^3

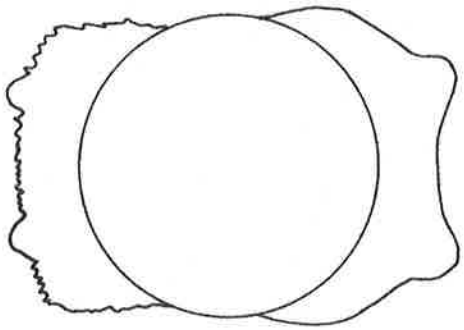

VELOCITY 122 m/s
L.W.C. 0.44 g/m^3

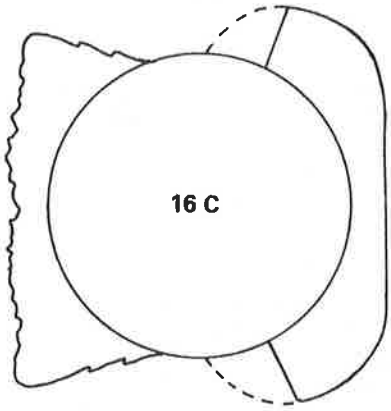

VELOCITY 122 m/s
L.W.C. 1.27 g/m^3

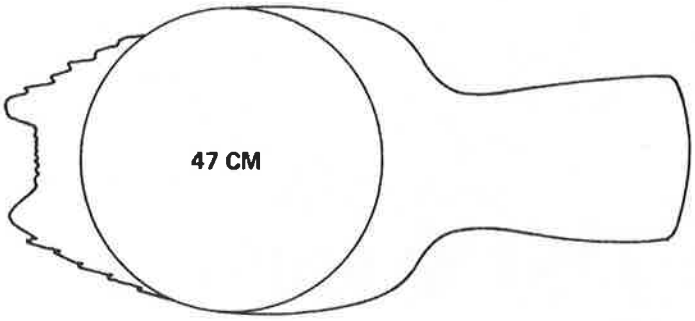

VELOCITY 122 m/s
L.W.C. 0.44 g/m^3
I.C.C. 1.0 g/m^3

FIG. 7.5: PROFILES OF SELECTED ACCRETIONS AT - 15°C.
THE EXPERIMENTAL PROFILES ARE ON THE LEFT AND THE MODEL-PREDICTED PROFILES ON THE RIGHT. THE MODEL PROFILES ARE ALL PLOTTED RADIALLY AND ARE BASED ON THE ROUGH HEAT TRANSFER COEFFICIENT. THE DASHED LINES INDICATE THE MODEL PROFILES IF RUNBACK TO 90° OCCURS BEFORE SHEDDING OF LIQUID WATER IS ALLOWED.

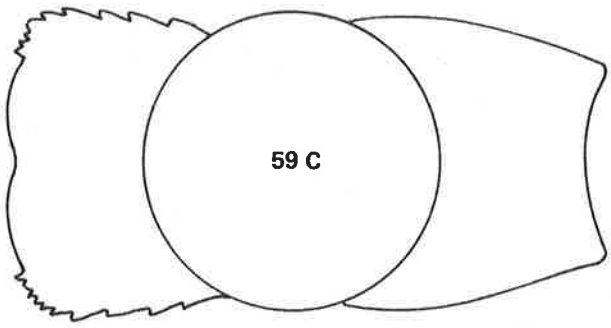

VELOCITY 110 m/s
L.W.C. 0.13 g/m^3

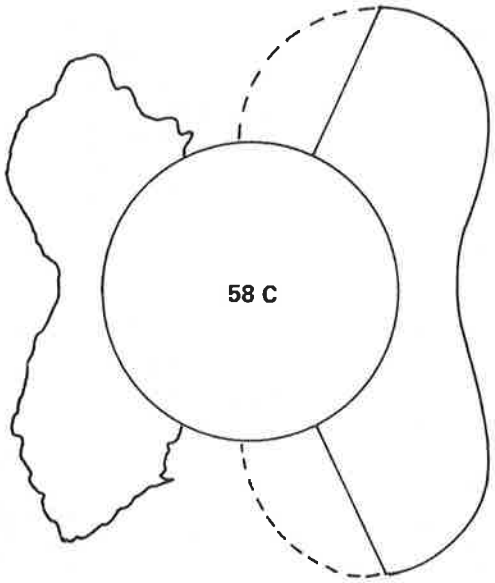

VELOCITY 110 m/s
L.W.C. 0.65 g/m^3

FIG. 7.6: PROFILES OF SELECTED ACCRETIONS AT -8°C.

THE EXPERIMENTAL PROFILES ARE ON THE LEFT AND THE MODEL-PREDICTED PROFILES ON THE RIGHT. IN CASE 59 C, THE SMOOTH HEAT TRANSFER COEFFICIENT IS ASSUMED AND THE GROWTH DIRECTION IS ASSUMED TO BE FORWARD. IN CASE 58 C, RADIAL GROWTH AND THE ROUGH HEAT TRANSFER COEFFICIENT ARE USED. THE DASHED LINES INDICATE THE MODEL PROFILE IF RUNBACK TO 90° OCCURS BEFORE SHEDDING OF LIQUID WATER IS ALLOWED.

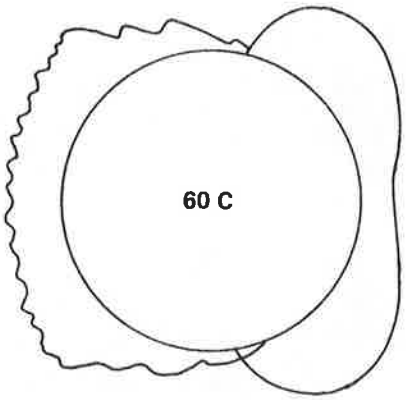

VELOCITY 30.5 m/s
L.W.C. 1.20 g/m^3

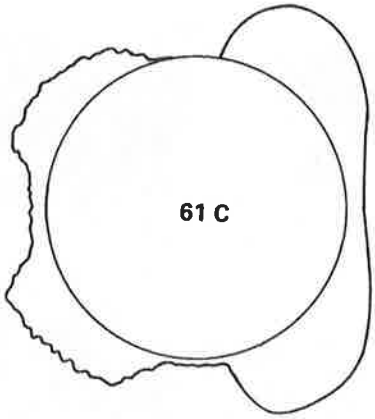

VELOCITY 91.5 m/s
L.W.C. .38 g/m^3

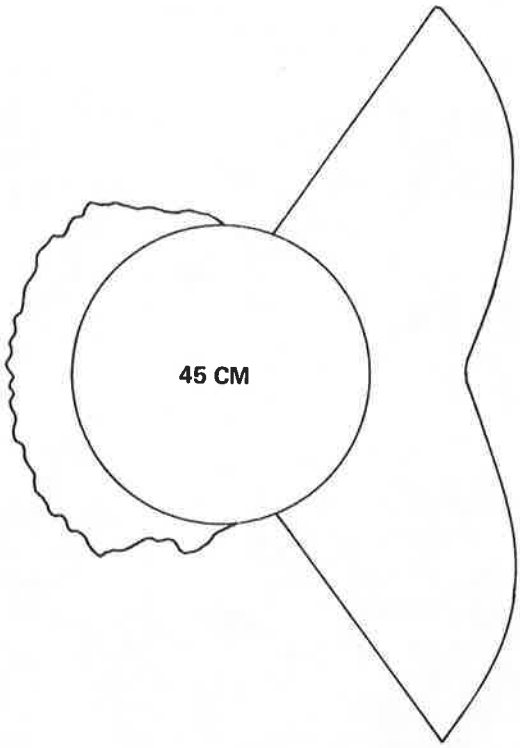

VELOCITY 30.5 m/s
L.W.C. 1.23 g/m^3
I.C.C. 1.2 g/m^3

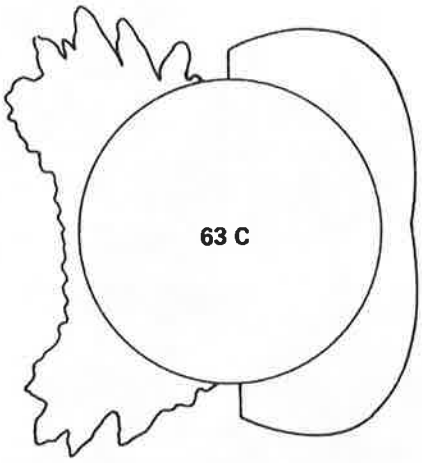

VELOCITY 91.5 m/s
L.W.C. 1.17 g/m^3

FIG. 7.7: PROFILES OF SELECTED ACCRETIONS AT -5°C.
THE EXPERIMENTAL PROFILES ARE ON THE LEFT AND THE MODEL-PREDICTED PROFILES ON THE RIGHT. THE MODEL PROFILES ARE ALL PLOTTED RADIALLY AND ARE BASED ON THE ROUGH HEAT TRANSFER COEFFICIENT.

APPENDIX A

COMPUTER PROGRAM LISTING FOR THE MODEL OF MIXED ICE ACCRETION ON A NON-ROTATING CYLINDER

```
10 PRINT
20 PRINT "       ***************************************************************"
30 PRINT "       *ICING OF A CIRCULAR CYLINDER IN MIXED CONDITIONS OF SUPER-   *"
40 PRINT "       *COOLED WATER AND ICE CRYSTALS USING ENGLISH/CANSDALE STICK-  *"
50 PRINT "       *ING ASSUMPTIONS FOR ICE AND ALLOWING FOR RUNBACK             *"
60 PRINT "       ***************************************************************"
70 PRINT
80 REM     ***********************************************************
90 REM     *  SATURATION VAPOR PRESSURE AND ITS TEMPERATURE DERIVATIVE  *
100 REM    ***********************************************************
110 REM
120 DEF FNE(X)=(((2.59E-04*X+2.7487E-02)*X+1.4472)*X+4.426E+01)*X+609.92
130 DEF FNP(X)=((1.036E-03*X+8.2461E-02)*X+2.8944)*X+44.26
140 REM
150 REM     ***********************************************************
160 REM     *               INPUT VARIABLES FROM KEYBOARD               *
170 REM     ***********************************************************
180 REM
190 DISP "SIX DIGIT DATE:DAY,MONTH,YEAR";
200 INPUT D7,D8,D9
210 WRITE (15,220)D7,D8,D9
220 FORMAT "                                    ",F3.0,"/",F3.0,"/",F3.0
230 PRINT
240 PRINT
250 DISP "AIR TEMPERATURE(DEGREES C)";
260 INPUT T2
270 PRINT "AIR TEMPERATURE =";T2;"DEG C"
280 PRINT
290 PRINT
300 DISP "LIQUID WATER CONTENT-KG/CUBIC M";
310 INPUT L
320 PRINT "LIQUID WATER CONTENT =";L;"KG/M**3"
330 PRINT
340 PRINT
350 DISP "ICE CRYSTAL CONTENT-KG/CUBIC M";
360 INPUT L9
370 PRINT "ICE CONTENT =";L9;"KG/M**3"
380 PRINT
390 PRINT
400 DISP "CYLINDER DIAMETER(METRES)";
410 INPUT D
420 PRINT "CYLINDER DIAMETER =";D;"METERS"
430 PRINT
440 PRINT
450 DISP "AIRSPEED(M/S):LOW,HIGH,INTERVAL";
460 INPUT V1,V2,V3
470 DISP "ROUGHNESS:SMOOTH=0,ROUGH=1";
480 INPUT R7
490 IF R7=1 THEN 540
500 PRINT "SMOOTH SURFACE HEAT TRANSFER ASSUMED"
510 PRINT
520 PRINT
530 GOTO 570
```

```
540 PRINT "ROUGH SURFACE HEAT TRANSFER ASSUMED"
550 PRINT
560 PRINT
570 REM
580 REM   ************************************************************
590 REM   *    DEFINE QUASI-PERMANENT VARIABLES VIA PROGRAM STATEMENTS *
600 REM   ************************************************************
610 REM
620 REM   ************************************************************
630 REM   *DROPLET DIAM SPECTRUM PERCENT VOLUME AT 5,10,....45 MICRONS *
640 REM   ************************************************************
650 REM
660 FOR J=1 TO 9
670 READ A[J]
680 NEXT J
690 DATA 6,10,19,29,18,8,3.5,1.5
700 PRINT "DROPLET SPECTRUM PARAMETERS--PERCENT VOLUME AT GIVEN DIAMETER"
710 PRINT
720 PRINT "5MU   10MU  15MU  20MU  25MU  30MU  35MU  40MU  45MU"
730 PRINT A[1];A[2];A[3];A[4];A[5];A[6];A[7];A[8];A[9]
740 PRINT
750 PRINT
760 REM
770 REM   ************************************************************
780 REM   *                  STATIC PRESSURE IN PASCALS              *
790 REM   ************************************************************
800 REM
810 P=1E+05
820 FOR V=V1 TO V2 STEP V3
830 PRINT "FREE STREAM VELOCITY =";V;"M/S"
840 PRINT
850 PRINT
860 REM
870 REM   ************************************************************
880 REM   *                        DEFINE CONSTANTS                  *
890 REM   ************************************************************
900 REM
910 P1=0.711
920 S=0.595
930 L2=2.5E+06
940 C1=1.005E+03
950 E1=0.622
960 C2=4.27E+03
970 C3=2.07E+03
980 R3=287.04
990 R4=918
1000 R9=1E+03
1010 REM
1020 REM   ************************************************************
1030 REM   *          CALCULATE FUNCTIONS OF AIR TEMPERATURE          *
1040 REM   ************************************************************
1050 REM
1060 R0=P/(R3*(T2+273.16))
1070 M=1.718E-05+5.1E-08*T2
1080 K=2.43E-02+7.3E-05*T2
1090 REM
1100 REM   ************************************************************
1110 REM   *                CALCULATE FUNCTIONS OF VELOCITY           *
```

```
1120 REM   ************************************************************
1130 REM
1140 R2=V*D*R0/M
1150 Z8=V*R0/M
1160 Z9=R9*V/(9*M*D)
1170 REM
1180 REM   ************************************************************
1190 REM   *   CALCULATE LOCAL COLLECTION EFFICIENCY,TOTAL COLLECTION   *
1200 REM   *        EFFICIENCY, MAXIMUM INPINGEMENT ANGLE               *
1210 REM   ************************************************************
1220 REM
1230 FOR J=1 TO 9
1240 D2=J*5E-06
1250 R8=Z8*D2
1260 K1=Z9*D2↑2
1270 S1=1/(1+0.0967*R8↑0.6367)
1280 K0=(K1-0.125)*S1+0.125
1290 IF K0<0.125 THEN 1410
1300 B[J]=1.4*(K0-0.125)↑0.84
1310 B[J]=B[J]/(1+B[J])
1320 E[J]=0.489*(LGT(8*K0))↑1.978
1330 T[J]=ATN(1.7*(K0-0.125)↑0.76)
1340 IF K0<0.9 THEN 1440
1350 E[J]=K0/(K0+PI/2)
1360 IF K0<7.5 THEN 1440
1370 B[J]=K0/(K0+1)
1380 IF K0<10 THEN 1440
1390 T[J]=ATNK0
1400 GOTO 1440
1410 E[J]=0
1420 B[J]=0
1430 T[J]=1E-10
1440 NEXT J
1450 REM
1460 REM   ************************************************************
1470 REM   *        CALCULATE FUNCTIONS OF ANGLE AROUND CYLINDER       *
1480 REM   ************************************************************
1490 REM
1500 FOR T4=0 TO PI/2 STEP PI/36
1510 IF R7=1 THEN 1540
1520 N=SQRR2*(1-(2*T4/PI)↑3)
1530 GOTO 1550
1540 N=SQRR2*(2.4+1.2*SIN(3.6*(T4-25*PI/180)))
1550 H=N*K/D
1560 R1=0.75+0.25*COS(2*T4)
1570 S3=0
1580 FOR J=1 TO 9
1590 IF T[J]<T4 THEN 1630
1600 G9=B[J]*COS(PI*T4/(2*T[J]))
1610 G9=G9+(PI↑3/(T[J]↑3*(PI↑2-4)))*(E[J]-2*T[J]*B[J]/PI)*T4↑2*SIN(PI*T4/T[J])
1620 S3=S3+G9*A[J]/100
1630 NEXT J
1640 PRINT "  TH   N1    TS       RI    BETA     QC       QE       QW";
1650 WRITE (15,1660)
1660 FORMAT 6X,"YF       QF       QV"
1670 REM
1680 REM  ************************************************************
1690 REM  *                    LOCAL COLLECTION EFFICIENCY             *
```

```
1700 REM  ************************************************************
1710 REM
1720 B1=S3
1730 B2=COST4
1740 REM
1750 REM  ************************************************************
1760 REM  *                  IMPINGING WATER AND ICE FLUXES          *
1770 REM  ************************************************************
1780 REM
1790 R=B1*L*V
1800 R6=B2*L9*V
1810 REM
1820 REM  ************************************************************
1830 REM  *CALCULATE LOCAL STATIC PRESSURE FOR EVAPORATIVE COOLING TERM*
1840 REM  ************************************************************
1850 REM
1860 P=P+(1.3*COS(2*T4)-0.3)*R0*V↑2/2
1870 IF T4=0 THEN 1920
1880 U1=U3
1890 U2=U4
1900 T7=T0
1910 GOTO 2040
1920 U1=0
1930 U2=0
1940 T7=0
1950 REM
1960 REM  ************************************************************
1970 REM  *       ITERATIVE SOLUTION OF THE HEAT BALANCE EQUATION    *
1980 REM  ************************************************************
1990 REM
2000 REM  ************************************************************
2010 REM  *       CALCULATE FUNCTIONS OF SURFACE TEMPERATURE         *
2020 REM  ************************************************************
2030 REM
2040 T1=0
2050 T=T2-T1
2060 L1=3.34E+05+(C2-C3)*T1
2070 REM
2080 REM  ************************************************************
2090 REM  *              CALCULATE HEAT TRANSFER TERMS               *
2100 REM  ************************************************************
2110 REM
2120 Q1=H*T
2130 Q2=(FNET2-FNET1)*H*L2*E1*(P1/S)↑0.63/(C1*P)
2140 Q3=R*C2*T
2150 Q5=H*R1*V↑2/(2*C1)
2160 Q6=R*V↑2/2
2170 Q7=R6*V↑2/2
2180 Y1=U1*C2*(T7-T1)
2190 Y2=U2*C3*(T7-T1)
2200 REM
2210 REM  ************************************************************
2220 REM  *                       TEST FOR NO SPRAY                  *
2230 REM  ************************************************************
2240 REM
2250 IF R=0 THEN 2270
2260 GOTO 2330
2270 IF U1=0 THEN 2290
```

```
2280 GOTO 2330
2290 K2=0
2300 M1=0
2310 F1=0
2320 GOTO 2770
2330 IF T1<0 THEN 2740
2340 IF T1>0 THEN 3150
2350 K2=1
2360 M1=0
2370 Q8=K2*R6*C3*T
2380 Q9=-K2*M1*R6*L1
2390 Y4=-M1*U2*L1
2400 F1=-(Q1+Q2+Q3+Q5+Q6+Q7+Q8+Q9+Y1+Y2+Y4)/(L1*(R+U1))
2410 IF F1>1 THEN 2510
2420 IF F1<0 THEN 2900
2430 REM
2440 REM  ************************************************************
2450 REM  *                        THERMODYNAMIC ZONE 3                *
2460 REM  ************************************************************
2470 REM
2480 Q4=F1*R*L1
2490 Y3=F1*U1*L1
2500 GOTO 3190
2510 IF R6=0 THEN 2740
2520 F1=1
2530 Q4=F1*R*L1
2540 Y3=F1*U1*L1
2550 K2=-(Q1+Q2+Q3+Q4+Q5+Q6+Q7+Y1+Y2+Y3+Y4)/(R6*C3*T-M1*R6*L1)
2560 IF K2<0 THEN 2740
2570 IF K2>1 THEN 2590
2580 GOTO 2660
2590 PRINT "ERROR: K EXCEEDS 1, PROGRAM STOPPED"
2600 GOTO 3430
2610 REM
2620 REM  ************************************************************
2630 REM  *                        THERMODYNAMIC ZONE 2                *
2640 REM  ************************************************************
2650 REM
2660 Q8=K2*R6*C3*T
2670 Q9=-K2*M1*R6*L1
2680 GOTO 3190
2690 REM
2700 REM  ************************************************************
2710 REM  *                        THERMODYNAMIC ZONE 1                *
2720 REM  ************************************************************
2730 REM
2740 F1=1
2750 K2=0
2760 M1=0
2770 Q4=F1*R*L1
2780 Q8=K2*R6*C3*T
2790 Q9=-K2*M1*R6*L1
2800 Y3=F1*U1*L1
2810 Y4=-M1*U2*L1
2820 P9=Q1+Q2+Q3+Q4+Q5+Q6+Q7+Q8+Q9+Y1+Y2+Y3+Y4
2830 P8=-H-H*L2*E1*(P1/S)↑0.63*FNPT1/(C1*P)-R*C2-K2*R6*C3
2840 P8=P8-K2*M1*R6*(C2-C3)+F1*R*(C2-C3)-U1*C2+F1*U1*(C2-C3)
2850 P8=P8-U2*C3-M1*U2*(C2-C3)
```

```
2860 T9=-P9/P8
2870 IF ABST9<0.01 THEN 3190
2880 T1=T1+T9
2890 GOTO 2050
2900 IF R6=0 THEN 2920
2910 GOTO 2930
2920 IF U2=0 THEN 3150
2930 F1=0
2940 Q4=F1*R*L1
2950 Y3=F1*U1*L1
2960 M1=(Q1+Q2+Q3+Q4+Q5+Q6+Q7+Q8+Y1+Y2+Y3)/((K2*R6+U2)*L1)
2970 IF M1>1 THEN 3150
2980 IF M1<0 THEN 3000
2990 GOTO 3070
3000 PRINT "ERROR: M IS NEGATIVE,PROGRAMME STOPPED"
3010 GOTO 3430
3020 REM
3030 REM  ************************************************************
3040 REM  *                    THERMODYNAMIC ZONE 4                  *
3050 REM  ************************************************************
3060 REM
3070 Q9=-M1*K2*R6*L1
3080 Y4=-M1*U2*L1
3090 GOTO 3190
3100 REM
3110 REM  ************************************************************
3120 REM  *                    THERMODYNAMIC ZONE 5                  *
3130 REM  ************************************************************
3140 REM
3150 F1=0
3160 K2=1
3170 M1=1
3180 GOTO 2770
3190 U3=(1-F1)*(R+U1)+M1*(K2*R6+U2)
3200 U4=(1-F1)*(1-M1)*(K2*R6+U2)
3210 T0=T1
3220 R5=F1*(R+U1+(1-M1)*(K2*R6+U2))
3230 W0=K2*R6+R+U1+U2
3240 IF W0=0 THEN 3270
3250 N1=R5/W0
3260 GOTO 3330
3270 N1=0
3280 REM
3290 REM  ************************************************************
3300 REM  *                  OUTPUT PARAMETERS AND RESULTS           *
3310 REM  ************************************************************
3320 REM
3330 T5=T4*180/PI
3340 WRITE (15,3350)T5,N1,T1,R5,B1,Q1,Q2,Q3,Y3,Q4,Q5
3350 FORMAT F4.0,F5.2,F5.1,E9.2,F5.2,6E8.1
3360 IF R5=0 THEN 3380
3370 GOTO 3390
3380 IF U3=0 THEN 3400
3390 NEXT T4
3400 PRINT
3410 PRINT
3420 NEXT V
3430 END
```

APPENDIX B

EQUIVALENCE BETWEEN THE SYMBOLS USED IN THE PROGRAM LISTING AND THE SYMBOLS USED IN THE TEXT

PROGRAM SYMBOL	TEXT SYMBOL	MEANING
A(J)	f_j	Fraction of total liquid water volume contained in droplets of size j
B1	β_i	Liquid water collection efficiency at angle θ_i
B2	β_{Ii}	Ice crystal collection efficiency at angle θ_i
B(J)	β_{oj}	Stagnation point collection efficiency for droplets of size j
C1	c_p	Specific heat capacity of air at constant pressure
C2	c_w	Specific heat capacity of liquid water
C3	c_I	Specific heat capacity of ice
D	D_c	Cylinder diameter
D2	D_j	Diameter of droplets of size j
E1	ϵ	Ratio of molecular weights of water vapor and dry air
E(J)	E_j	Total collection efficiency of droplets of size j
F1	f	Freezing fraction of liquid water
G9	β_{ij}	Collection efficiency for droplets of size j at angle θ_i
H	h	Local heat transfer coefficient
K	k_a	Thermal conductivity of air
K0	K_{oj}	Langmuir-Blodgett modified inertia parameter for droplets of size j
K1	K_j	Langmuir-Blodgett inertia parameter for droplets of size j
K2	k	Sticking fraction of impinging ice crystals
L	w	Liquid water content of airstream
L1	ℓ_f	Specific latent heat of freezing
L2	ℓ_v	Specific latent heat of vaporization
L9	w_I	Ice crystal content of airstream

APPENDIX B (Cont'd)

PROGRAM SYMBOL	TEXT SYMBOL	MEANING
M	μ_a	Dynamic viscosity of air
M1	m	Melting fraction of sticking ice crystals
N	Nu	Nusselt number
N1	n	Fraction of total incoming water substance which remains in a sector as ice (ice fraction of deposit)
P	p	Airstream static pressure
P1	Pr	Prandtl number
P6	$g(t_s)$	Derivative of right-hand side of heat balance equation
P9	$f(t_s)$	Right-hand side of heat balance equation
Q1	q_c	Heat transfer to airstream by conduction and convection
Q2	q_e	Latent heat transfer to airstream by evaporation or sublimation
Q3	q_w	Heat required to warm accreted liquid to deposit temperature from airstream temperature
Q4	q_f	Latent heat of freezing of a fraction f of impinging liquid
Q5	q_v	Aerodynamic heating of deposit
QC	q_{kw}	Kinetic energy flux of impinging water droplets
Q7	q_{kI}	Kinetic energy flux of impinging ice crystals
-	q_k	Sum of kinetic energy flux of impinging water droplets and ice crystals ($q_{kw} + q_{kI}$)
Q8	q_I	Heat required to warm impinging ice crystals from airstream temperature to deposit temperature
Q9	q_m	Heat required to melt a fraction m of the sticking ice crystals
R	R_w	Airstream liquid water mass flux
R0	ρ_a	Density of air
R1	r_i	Recovery factor at angle θ_i
R2	Re_c	Reynolds number for the cylinder
R3	R_d	Specific gas constant for dry air
R4	ρ_I	Density of ice
R5	R	Ice growth flux of deposit
R6	R_I	Airstream ice crystal mass flux

APPENDIX B (Cont'd)

PROGRAM SYMBOL	TEXT SYMBOL	MEANING
R7	R_o	Roughness parameter for determining heat transfer coefficient
R8	Re_j	Reynolds number for droplets of size j
R9	ρ_w	Density of liquid water
S	Sc	Schmidt number
S1	$\left(\frac{\lambda}{\lambda_s}\right)_j$	Langmuir-Blodgett parameter for droplets of size j — ratio of true droplet ballistic range to range under Stokes law approximation
S8	—	Temporary storage
T0	t_s^{*OUT}	Outgoing runback temperature from a sector (°C)
T1	t_s	Deposit temperature (°C)
T2	t_a	Airstream temperature (°C)
T4	θ	Angle around cylinder measured from forward stagnation line — θ is in degrees, T4 is in radians
T5	—	Conversion of T4 from radians to degrees
T7	t_s^{*IN}	Incoming runback temperature to a sector
T9	δt_s	Change in surface temperature during heat balance iteration
T(J)	θ_{mj}	Maximum impingement angle for droplets of size j
U1	R_w^{*IN}	Incoming liquid runback flux
U2	R_I^{*IN}	Incoming ice runback flux
U3	R_w^{*OUT}	Outgoing liquid runback flux
U4	R_I^{*OUT}	Outgoing ice runback flux
V	U	Free stream velocity
W0	—	Total incoming water substance flux ($R_w + R_w^{*IN} + k \times R_I + R_I^{*IN}$)
Y1	y_c	Heat flux liberated upon cooling of runback liquid
Y2	y_I	Heat flux liberated upon cooling of runback ice
Y3	y_f	Latent heat of freezing of runback liquid
Y4	y_m	Latent heat of melting of runback ice
Z8	Re_j/D_j	See R8 and D2
Z9	K_j/D_j^2	See k1 and D2

APPENDIX C

SUMMARY OF CONDITIONS AND RESULTS OF CYLINDER ICING TESTS

Test No.	Temp. °C	Air Speed m/s	LWC g/m^3	ICC g/m^3	Icing Duration min.	Stagnation Growth Rate μm/s	Maximum Icing Extent degrees	Movie	Notes
17C	-15	30.5	.4(0)	-	5.00	9.(1)	70	time lapse	30° to start of rime
3C	-15	30.5	.8(2)	-	5.00	18.(2)	75	no	
4C	-15	30.5	1.2(3)	-	5.00	25.(2)	68	no	
8C	-15	61	.4(6)	-	2.50	22.(9)	75	no	30° to start of rime
20C	-15	61	.7(7)	-	1.00	38.(1)	74	no	20° to end of glaze
12C	-15	61	1.2(5)	-	2.33	50.(9)	75	time lapse	
14C	-15	122	.4(4)	-	2.50	38.(6)	73	time lapse	28° to end of glaze; growth rate to horns 49.1 μm/s
18C	-15	122	.8(2)	-	1.00	50.(8)	72	time lapse	25° to peaks
16C	-15	122	1.2(7)	-	1.00	67.(7)	70	time lapse	35° to peaks
46CM	-15	30.5	.4(0)	1.2	5.00	8.(2)	--	no	
36CM	-15	61	.4(6)	.4	2.50	22.(9)	--	no	
40CM	-15	61	1.2(5)	.6	2.33	55.(4)	--	no	Growth rate to isolated peaks 60.(9) μm/s
47CM	-15	122	.4(4)	1.0	2.50	28.(8)	--	no	Growth rate to horns 44.(2) μm/s
48CM	-15	122	1.2(7)	1.0	1.00	65.(6)	--	no	IWC probably lower - snow slipping on belt
59C	-8	110	.1(3)	-	20.00	8.(9)	--	no	Forward growth rate to bulges 10.(0) μm/s; thin section
56C	-8	110	.2(8)	-	10.00	12.(8)	--	no	Forward growth rate to bulges 16.(6) μm/s
58C	-8	110	.6(5)	-	5.00	12.(1)	--	no	Forward growth rate to bulges 28.(3) μm/s
55CM	-8	110	.2(8)	.8	10.00	13.(5)	--	no	Forward growth rate to peaks 27.(5) μm/s

APPENDIX C (cont'd)

Test No.	Temp. °C	Air Speed m/s	LWC g/m^3	ICC g/m^3	Icing Duration min.	Stagnation Growth Rate μm/s	Maximum Icing Extent degrees	Movie	Notes
5C	-5	30.5	.4(0)	-	5.00	7.(5)	58	no	
65C	-5	30.5	.7(8)	-	5.00	14.(6)	68	no	Runback to 90°
60C	-5	30.5	1.2(0)	-	5.00	15.(2)	70	no	Runback to 115°; growth rate to bumps 16.(1) μm/s
9C	-5	61	.4(6)	-	4.00	13.(8)	75	time lapse	
11C	-5	61	.7(8)	-	2.92	21.(5)	83	time lapse	Runback to 105°; test 66C yields 18.(6) μm/s
13C	-5	61	1.2(5)	-	2.50	16.(3)	73	time lapse	Runback to 103°; growth to peaks 23 to 57 μm/s
61C	-5	91.5	.3(8)	-	4.00	6.(6)	--	no	Growth rate to peak 10.(9) μm/s
62C	-5	91.5	.7(6)	-	4.00	7.(9)	--	no	Growth rate to peak ~ 22 μm/s
63C	-5	91.5	1.1(7)	-	4.00	8.(9)	--	no	Growth rate to peak ~30 μm/s
15C	-5	122	.4(4)	-	2.50	0.	90	time lapse	Spike height ~ .25 cm; flow separation ~5° ahead of spike
64C	-5	122	1.1(0)	-	4.00	0.	110	no	Spike height ~ .33 cm
42CM	-5	30.5	.4(0)	1.0	5.00	9.(6)	--	no	Snow injection temp. -20°C
45CM	-5	30.5	1.2(3)	1.2	5.00	18.(8)	--	no	Growth rate to peaks 21 μm/s; snow injection temp. -12°C
38CM	-5	61	.4(6)	.6	4.00	16.(4)	--	no	
41CM	-5	61	1.2(5)	.6	2.50	23.(7)	--	no	Growth rate to lobe front 32 μm/s
68CM	-5	91.5	.3(8)	0.1	2.50	7.(5)	--	high speed	Ice content doesn't account for recirculating snow
52CM	-5	122	.4(4)	1.3	2.50	0.	>90	no	
72C	-15	122	.4(7)	-	5.00	37.(2)	--	no	Similar to 14C but grown for twice as long; thin section
70CM	-15	122	.4(4)	0.7	2.50	28.(8)	--	high speed	Growth rate at peaks 43.(8) μm/s; similar to 47CM